1-1-2008

Simulations of polymer crystallization and amyloid fibrillization.

Jianing Zhang
University of Massachusetts Amherst

SIMULATIONS OF POLYMER CRYSTALLIZATION AND AMYLOID FIBRILLIZATION

A Dissertation Presented

by

JIANING ZHANG

Submitted to the Graduate School of the
University of Massachusetts Amherst in partial fulfillment
of the requirements for the degree of

DOCTOR OF PHILOSOPHY

September 2008

Department of Polymer Science and Engineering

SIMULATIONS OF POLYMER CRYSTALLIZATION AND AMYLOID FIBRILLIZATION

A Dissertation Presented

by

JIANING ZHANG

Approved as to style and content by:

_____
M. Muthukumar, Chair

_____
Jonathan Machta, Member

_____
Scott M. Auerbach, Member

_____
Shaw Ling Hsu, Department Head
Polymer Science and Engineering

SIMULATIONS OF POLYMER CRYSTALLIZATION AND AMYLOID FIBRILLIZATION

A Dissertation Presented

by

JIANING ZHANG

Approved as to style and content by:

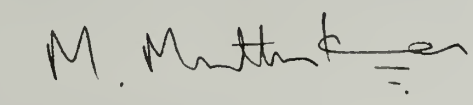

M. Muthukumar, Chair

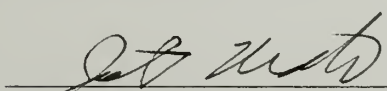

Jonathan Machta, Member

Scott M. Auerbach, Member

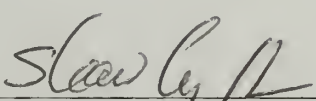

Shaw Ling Hsu, Department Head
Polymer Science and Engineering

ACKNOWLEDGMENTS

I would like to thank my advisor, Prof. Muthukumar, for his guidance and support over the years. Muthu has been a role model for me. As a first-year student, I have learned from him how to give an excellent lecture, and how to explain a complex subject to the audience. He is passionate about the research and possesses strong intellectual curiosity about various scientific questions. He has advised me not only on my research, but also on general research philosophy and communication skills. I really appreciate the cozy research environment Muthu created and tremendous respect from Muthu who treats his students like his colleagues.

I am also grateful to my committee members, Prof. Machta and Prof. Auerbach, for their time, patience, and insightful questions and comments.

I also thank my fellow research group members: Zhaoyang, Chilun, Andrew, Jiafang, Shulan, Chris, Ryan, Joanna, Jessica, Joey, Vladimir, Arindam, Ajay, Mark, Rajeev, Deniz, Xiangdong, JP, Erica, Ashok, Sonoko, Abhijit, and Joe. I am lucky to be part of this stimulating group that is full of brilliant minds.

I am indebted to my parents. It is them who always stand behind me, encourage me and show me what love and sacrifice are about. Last but not least, I would like to thank my wife for her love and support. I would like to dedicate the thesis to my daughter who is the source of immeasurable joy.

ABSTRACT

SIMULATIONS OF POLYMER CRYSTALLIZATION AND AMYLOID FIBRILLIZATION

SEPTEMBER 2008

JIANING ZHANG, B.E., TONGJI UNIVERSITY

M.S., FUDAN UNIVERSITY

Ph.D., UNIVERSITY OF MASSACHUSETTS AMHERST

Directed by: Professor M. Muthukumar

This dissertation describes computer simulations and theoretical analyses of polymer crystallization and amyloid fibrillization. Langevin Dynamics simulations of polymer chains in dilute solutions suggest that chains are prefolded before crystallization, in contradiction with the traditional view that chain folding occurs only on the growth front. The prefolded chain reveals a thickness plateau in low-temperature region (solving the puzzle of "δL catastrophe"), suggesting that lamellar thickness might be a predetermined equilibrium result. Based on the above prefolding and predetermined thickness concepts, the prefolded chains are then taken as the smallest dynamic units in Monte Carlo simulations, where an anisotropic aggregation model is proposed to study single crystals, shish-kebab crystals, and crystal melting. This model is further extended to amyloid fibrillization.

The single crystal study shows a rough-flat-rough habit transition, solving a long-standing puzzle for the existing theories. The lamellar growth rate is confirmed to vary exponentially with temperature and concentration. The shish-kebab study confirms that the distribution of kebab spacings is lognormal. In contrast to Pennings' and Hill's

models, a new model is proposed to describe the relation between the spacing and temperature: the logarithm of the spacing growth rate is proportional to the inverse of temperature. The spacing is also found to be proportional to the inverse of polymer concentration. A broad melting transition for shish-kebab crystals is observed in simulations. The melting point is confirmed to be proportional to the square root of heating rate, increase exponentially with crystallization temperature, and increase with the logarithm of crystallization time in sigmoidal fashion. It is proposed that the melting point is related to the lamellar diameter, rather than the lamellar thickness in the traditional view. The seeding phenomenon for amyloid fibrils is reproduced in simulations. It is proposed that nucleation of the amyloid fibril is due to its semi-two-dimensional nature, because a pure one-dimensional growth does not require nucleation and does not exhibit sigmoidal curves. The importance of the second layer of β-sheet is stressed. It is proposed that Ostwald ripening (bigger fibrils grow at the expense of smaller ones) is the dominating mechanism for amyloid fibril growth.

TABLE OF CONTENTS

Page

ACKNOWLEDGMENTS iv

ABSTRACT v

LIST OF TABLES x

LIST OF FIGURES xi

CHAPTER

1. INTRODUCTION 1

1.1 Organization 1
1.2 Research Philosophy and Goals 3

1.2.1 Computer Experiments 3
1.2.2 Big Picture 5

2. CHAIN PREFOLDING 8

2.1 Introduction 8
2.2 Model and Simulation Algorithm 10
2.3 Results and Discussion 13
2.4 Conclusions 14

3. SINGLE CRYSTAL 19

3.1 Introduction 19
3.2 Model and Simulation Algorithm 23
3.3 Results and Discussion 26

3.3.1 Crystal Habit 26
3.3.2 Time Evolution of Lamellar Size 29
3.3.3 Induction Time and Critical Nucleus Diagram 30
3.3.4 Lamellar Growth Rate 33
3.3.5 Mechanism of Rough-flat-rough Habits 34
3.3.6 Mechanism of Nucleation 35

3.4 Conclusions 36

4. SHISH-KEBAB CRYSTAL 47

4.1 Introduction 47
4.2 Model and Simulation Algorithm 50
4.3 Results and Discussion 51

4.3.1 Morphology 51
4.3.2 Kebab Spacing Distribution 52
4.3.3 Time Evolution of Kebab Spacings 53
4.3.4 Temperature vs. Spacings 53
4.3.5 Concentration vs. Spacings 55
4.3.6 Kebab Diameter Distribution 55
4.3.7 Time Evolution of Kebab Diameters 55

4.4 Conclusions 56

5. CRYSTAL MELTING 67

5.1 Introduction 67
5.2 Model and Simulation Algorithm 72
5.3 Results and Discussion 72

5.3.1 Morphology 72
5.3.2 Broad Melting Transition 73
5.3.3 Effects of Heating Rate 74
5.3.4 Effects of Crystallization Temperature 76
5.3.5 Effects of Crystallization Time 76

5.4 Conclusions 77

6. AMYLOID FIBRILLIZATION 84

6.1 Introduction 84
6.2 Model and Simulation Algorithm 86
6.3 Results and Discussion 91

6.3.1 Single Fibril 91

6.3.1.1 Energy Ratio vs. Length Ratio 91
6.3.1.2 Nucleation and Growth 92
6.3.1.3 Fibril Size and Lag Time 93

6.3.2 Multiple Fibrils 94

6.3.2.1 Time Evolution 94
6.3.2.2 Effects of Concentrations 96
6.3.2.3 Effects of Temperature 96
6.3.2.4 Seeding 97

6.3.2.5 Disassembly upon Dilution 98

6.3.3 Mechanism of Nucleation and Growth 98

6.4 Conclusions 102

7. CONCLUSIONS AND FUTURE WORK 117

7.1 Polymer Crystallization 117

7.1.1 Conclusions 117
7.1.2 Future Work 120

7.2 Amyloid Fibrillization 121

7.2.1 Conclusions 121
7.2.2 Future Work 122

BIBLIOGRAPHY 124

LIST OF TABLES

Table		Page
7.1.	Comparisons between the two existing models and our prefolding model	123

LIST OF FIGURES

Figure — Page

2.1. (a) Chain folding occurs during the crystallization process and is facilitated by the growth front template, i.e., secondary nucleation. (b) Chain folding occurs before the aggregation (crystallization) process and is not facilitated by other chains or the growth front, i.e., self prefolding. 16

2.2. Five chains of 500 beads prefold by themselves into bundles. These bundles aggregate by attractive van der Waals interactions (no stem nucleation barrier). 17

2.3. (a) Time-averaged radius of gyration of single chain of 500 beads at different temperatures. Each data point is averaged over five different runs. (b) Lamellar thickness as determined by low-angle x-ray diffraction as a function of crystallization temperature for isotactic polystyrene from dimethyl phthalate. Theoretical relation in Equation (2.1) can not fit with experimental results even for different parameter values. 18

3.1. polymer solutions for single crystal growth are mapped onto a 3D array of lattice sites. Each lattice site takes one of five possible states. S_4 serves as the nucleus for subsequent crystal growth. $S_{1\sim3}$ and S_4 are interconvertible by adsorption and desorption. Interactions between $S_{1\sim3}$ are disabled in order to form a "single" crystal. For clarity, the solvent site S_0 is invisible herein except one example shown in the bottom-right corner. 39

3.2. Five typical habits for solution-grown polymer crystals. The upper part (1-4) shows experimental observations: (1) 0.01% polyethylene in xylene solution.[50] (2) 0.1% polyethylene in o-xylene solution.[48] (3) 0.1% isotactic polystyrene in dimethyl phthalate solution.[53] (4) 0.05% polyethylene solution.[40] The middle part (5-9) presents our typical simulation results at various temperatures and concentrations. Note that a rough-flat-rough transition of habits occurs by merely adjusting temperature at $C = 0.00002$. The lower part (10-14) gives sketches of habits. 40

3.3. Roughness parameter (RP) as functions of temperature and concentration. 41

3.4. Time evolution of the lamellar size at various temperatures with a fixed $C = 0.0002$. The initial nucleus size is $R_0 = 5$. The simulation box size is $L_{box} = 200$. The four micrographs illustrate how the nucleus grows and redissolves with time until a fluctuation in size is large enough to overcome the nucleation barrier, where the number of crystalline chains in the crystal is equal to 25, 75, 25, 90 for $t = 207, 448, 571, 784$ ($\times 10^4$MCS), respectively. 42

3.5. (a) Induction time τ as a function of temperature kT for various seed sizes R_0. $C = 0.0002$. The inset presents the critical nucleus size R_c as a function of temperature, which is obtained by intersects of a horizontal line $\tau = 100 \times 10^4$MCS with four curves at positions $kT = 0.146, 0.179, 0.189, 0.196$ for $R_0 = 1, 3, 5, 7$, respectively. (b) R_c is plotted as functions of both kT and C, resulting in a phase diagram with three regions..... 43

3.6. (a) Temperature dependence of the lamellar growth rate G at various concentrations. (b) Logarithmic of crystal growth rate against crystallization temperature for solution crystallization of Poly(ethylene oxide) of different molecular weights.[67] (c) Concentration dependence of the lamellar growth rate G at various temperatures. (d) Logarithmic growth rate (μm/hr) versus concentration of crystals for polyethylene sample grown from octane at different temperatures.[62] 44

3.7. The total number of *i*-neighbor desorption events occurred during the late stage of crystallization at various temperatures. 1-, 2-, 3-neighbor crystallites become unstable at $kT = 0.10, 0.12, 0.16$ respectively, resulting in different crystal habits. $C = 0.0002$..... 45

3.8. Mechanism of nucleation and stability of edge crystallites. (a) 3×3 nucleus; (b) 5×5 nucleus. The number in each square designates how many neighboring crystallites it has..... 46

4.1. Polymer solution for shish-kebab crystallization is mapped onto a three-dimensional array of lattice sites with length $100 \times 100 \times 100$. Each lattice takes one of five possible states: x-, y-, z-oriented free chains, z-oriented crystalline chain (shish or kebab crystallite), and empty lattice site (invisible here). 58

4.2. Time evolution of kebab formation. (a) kT=0.12, C=0.001; (b) kT=0.15 (higher temperature results in larger spacings and bigger kebabs), C=0.001; (c) kT=0.15, C=0.005 (higher concentration results in narrower spacings and bigger kebabs). 59

4.3. (a) Time evolution of skewed distribution of kebab spacings. All the curves are under conditions kT=0.14 and C=0.001. (b) Lognormal distribution of kebab spacings by Pennings et al.[68,69] 60

4.4. (a) Time evolution of the kebab spacing at different temperatures in our simulations. (b) Time evolution of the kebab spacing at different washing temperatures in experiments.[71] 61

4.5. Time evolution of temperature dependence of the kebab spacing. (a) Simulation results at C=0.001. (b) Experimental results extracted from Table 2 in Ref. [71]. 62

4.6. (a) Pennings' model: $\ln S \sim 1/T\Delta T$. (b) Hill's model: $\ln S \sim 1/T\Delta T^2$. (c) Our model: $\ln G_S \sim 1/T$, where $G_S = (S - S_0)/time$ is the spacing growth rate, S_0 is the initial spacing in Figure 4.4a, or the constant minimum spacing in the low-T region in Figure 4.5a. 63

4.7. (a) Time evolution of the average kebab spacing at different concentrations. kT=0.15. (b) The spacing growth rate, the slope in (a), is proportional to the inverse of polymer concentration, i.e., $G_S \sim 1/C$ 64

4.8. (a) Time evolution of symmetric distribution of kebab diameters. kT=0.14 and C=0.001. (b) The diameter distribution in (a) normalized by the average diameter in X axis and the total number of measurements in Y axis becomes invariant with time. 65

4.9. (a) Time evolution of the average kebab diameter at different temperatures. (b) The curves in (a) are horizontally shifted into a master curve. 66

5.1. T_c is isothermal crystallization temperature, t_c is crystallization time, and β is heating rate. The melting point T_m is obtained as the temperature at which the last trace of crystals disappears. 79

5.2. Melting transition upon heating: time evolution of crystallinity in (a) and endotherm in (b). 80

5.3. Melting temperature is proportional to the square root of heating rate. (a) Simulations. (b) Experiments.[104] 81

5.4. The dependence of melting temperature on crystallization temperature (Hoffman-Weeks Plot). (a) Simulations. (b) Experiments.[93] 82

5.5. T_m increases with $\log t_c$ in sigmoidal fashion. The one-to-one correlation between T_m and $\log R$ is evident. T_m values are represented by the symbols and $\log R$ values by the lines, sharing the same abscissa $\log t_c$ in the same range. $\log R$ data are extracted from Figure 4.9a in the previous chapter. 83

6.1. Peptide solutions for amyloid fibril formation are mapped onto a 3D array of lattice sites. Each peptide (a bead-rod chain) occupies one lattice and is represented by a cuboidal brick which randomly walks, randomly changes its orientation (state $S_1 \sim S_6$), and aggregates with other peptides when having the same orientation. The solvent (state S_0) is represented by the empty lattice which is invisible here for clarity. For the single-fibril case, an additional state S_7 (same orientation as S_6) is introduced to serve as the seed nucleus. The fibril thus formed has length L_x, width L_y, intra-sheet H-bonding interaction E_x, and inter-sheet interaction E_y. 105

6.2. The length ratio (L_x / L_y) as a function of the energy ratio (E_y / E_x). The size of the initial seed nucleus is 1 (almost invisible); the size of the simulation box $B_x = 250$ and $B_y = B_z = 100$; temperature $kT = 1.0$; the initial peptide concentration $C = 0.0005$; the total simulation time $t_{\max} = 10^7$ MCS. (a) Initial and final morphologies for various energy ratios. (b) L_x / L_y vs. E_y / E_x. L_x / L_y is averaged over t =(800–1000)×10^4 MCS. 106

6.3. Nucleation and growth of single fibril. The seed size is 1; kT =1.17; C =0.001. All subsequent simulations on single fibrils are under the conditions $B_x = 500$, $B_{y,z} = 50$, and $t_{\max} = 10^7$ MCS. In the rest of the chapter, the default energy settings are $E_x = -10$, $E_y = -1$, and $E_{z,n} = +10$. 107

6.4. Time evolution of the fibril size (R) and the corresponding lag time (τ) as a function of the initial seed size ($n_x \times n_y$). C =0.001 and kT =1.2. 108

6.5. Time evolution of the fibril size (R) and the corresponding lag time (τ) as a function of the initial peptide concentration (C). kT =1.2 and the seed size is 1. 109

6.6. Time evolution of morphologies and fibril size distributions for multi-fibril assembly. C =0.001; kT =0.8; all subsequent simulations on multiple fibrils are performed in the simulation box with length $B_{x,y,z} = 100$. (a) Morphological evolution in simulations. (b) Morphological evolution in experiments.[143] (c) Time evolution of fibril size distributions in simulations. The integrated "Area" represents the total number of protofibrils. (d) Time evolution of fibril size distributions in experiments.[143] 110

6.7. Morphologies as a function of peptide concentrations for (a) simulation results at $t = 10^7$ MCS and (b) experimental results.[143] Concentration dependence of the fibril growth rate for (c) simulation results and (d) experimental results.[143] 111

6.8. Morphologies as a function of temperature for (a) simulation results at $t = 10^7$ MCS and (b) experimental results.[143] Temperature dependence of the initial fibril growth rate for (c) simulation results and (d) experimental results.[143] 112

6.9. Effects of seeding and seed concentrations on fibril growth. Time evolution of the total fibril mass (based on all fibrils whose size ≥ 10) is monitored for the unseeded, 1-seed, and 4-seed cases, respectively. The corresponding morphologies for the unseeded and 4-seed cases are given at t =0, 50, 300, 430, 800 ($\times 10^5$MCS). The size of each seed is 20×2. C =0.0005, kT =0.9. The mass contribution due to added seeds was subtracted.[129,133] Due to the stochastic nature, only one typical run is given for the time-mass curve. The average lag time of 50 simulation runs, however, indeed decreases with increasing the seed concentration: τ =171, 74, 3 ($\times 10^5$ MCS) for the unseeded, 1-seed, and 4-seed cases, respectively. 113

6.10. (a) Disassembly upon dilution. The already-formed fibrils (under the conditions C =0.002, kT =0.9, simulation box length 100) are put in a bigger simulation box with length 300 to simulate effects of dilution. (b) Experimental results where the sample was diluted 20-fold.[143] 114

6.11. Mechanisms of nucleation and Ostwald ripening. 1-, 2-, and 3-layer fibrils are all in dynamic exchange with monomers. 115

6.12. Pure 1D growth. The energy settings are $E_{\tau} = -10$ and $E_{y,z,n} = +10$. $B_x = 500$, $B_{y,z} = 30$, C =0.001. (a) Morphological evolution at kT =1.0. (b) Fibril growth at various temperatures. No sigmoidal curve is observed at any kT. 116

CHAPTER 1

INTRODUCTION

1.1 Organization

Due to the interdisciplinary nature of this dissertation, the literature review commonly found in the Introduction is to be given in later chapters together with relevant data and discussions. Instead, Chapter 1 covers the organization and common themes of all the research work. The research goals and the philosophy guiding my research are also presented here.

Chapter 2 utilizes Langevin Dynamics simulations to test the most basic assumption in Lauritzen-Hoffman theory[1,2] of polymer crystallization – chains fold only on the growth front, i.e., "template folding", where the growth front is the edge of the polymer crystal preformed by other chains that might be longer or stochastically lucky. In contrary, our simulation results clearly demonstrate that, in a dilute solution where chains are far away from one another, chains undergo "self folding" without the facility of the growth front, and then these prefolded chains aggregate into a polymer crystal. This "prefolding" concept is contradictory to the Lauritzen-Hoffman theory,[1,2] where chain folding and polymer crystallization occur simultaneously on the growth front. To test this "prefolding"/"self-folding" concept, we then perform systematic Monte Carlo simulations for various aspects of polymer crystallization in Chapter 3, 4, and 5.

Chapter 3 focuses on polymer single crystals. The prefolded chain serves as the smallest dynamic unit in the Monte Carlo simulations. The simulation results resolve the long-standing dilemma regarding crystal habit (shape). Lauritzen-Hoffman theory

can explain the low-temperature (low-T) roughening of the crystal outline, but can not explain the high-temperature (high-T) roughening well. On the contrary, Sadler-Gilmer model[3-7] can explain the high-T roughening, but can not explain the low-T roughening. Our simulation results naturally reveal both high-T and low-T roughenings, which can be explained by the different local binding energies. Besides crystal habits, crystal sizes, induction time, and growth rates are evaluated as functions of both temperature and polymer concentrations in solution. All simulation results are compatible with experimental results. In addition, because the nucleus size can be explicitly specified in simulations, we are able to deduce, for the first time, a phase diagram of critical nucleus sizes from the data of induction time.

Chapter 4 focuses on shish-kebab polymer crystals. The shish is pre-set to serve as the nucleation sites. Following the same methods in Chapter 3, the prefolded chains diffuse and aggregated on the shish to form kebabs. The kebab spacing (distance between neighboring kebabs) and diameters are investigated as functions of time, temperature, and concentrations. The experimental fact that the kebab spacing enlarges as time elapses is confirmed by our simulations and explained by Ostwald ripening mechanism (i.e., evaporation-condensation mechanism). A new temperature-spacing relation is proposed and compared with the existing two theories. We also predict that the kebab spacing is inversely proportional to the polymer concentration in solution.

Chapter 5 focuses on melting of multiple crystals (shish-kebab crystals as a model system). The melting point is defined as the temperature at which the last trace of polymer crystals disappears. The dependences of melting points on crystallization time,

crystallization temperature, and heating rates are investigated. The results are consistent with experimental results and reveal some new features.

Chapter 6 utilizes a similar Monte Carlo model to simulate amyloid fibril formation which is relevant to Alzheimer's and Huntington's diseases. Although polymer crystallization and amyloid fibrillization belong to entirely different fields, they are both certain types of aggregation (either aggregation of prefolded chains, or aggregation of folded/extended peptides). Surprisingly, nucleation and Ostwald ripening mechanisms also play important roles in the amyloid fibrillization process. For the first time, we are able to reproduce the "seeding" phenomenon[8,9] (the lag time of fibril growth is reduced by adding preformed fibrils) which has been widely seen in many amyloid experiments but not fully understood. In addition, we are able to reproduce many experimental observations including time evolution of fibril size distributions and disassembly upon dilution. The temperature and concentration dependences of fibril elongation rates agree well with experiments.

1.2 Research Philosophy and Goals

1.2.1 Computer Experiments

Computer simulation is a bridge between theory and experiment. Simulation is similar to theory in that it is usually based on certain equations. For example, Langevin Dynamics is based on the Newtonian equation of motion with a random noise term included to simulate collision of solvent molecules. Metropolis algorithm in Monte Carlo simulations is based on the equation of acceptance probability which depends exponentially on the energy change. Simulation is also similar to experiment, in the

sense that once you input parameters you have to allow the simulation to run (evolve like an experiment) to a final unpredictable result (because of the uncertainty introduced by the noise term or the probability term). Simulation is better than theory in one aspect – simulation makes far lesser assumptions than theory does. The world is simple. The lesser assumptions (usually arbitrary or subjective) you make, the closer you are to the truth. Simulation is better than experiment in one aspect too – simulation is a totally apparent process but experiment is usually performed in a black box. In simulations, you keep the track of each individual particle so that you can calculate whatever quantity you want. In experiments, on the contrary, you normally get only one or two ways of characterization outputs. However, simulation is worse than theory in one aspect – simulation is more difficult to be tested against experiment than theory is. It is much easier and less time-consuming to use an equation than to run a simulation. Simulation is secondary to experiment, because experiment is the king of science. If simulation wants to predict and guide experiment, it has to prove itself first by reproducing certain amounts of experiments. If simulation and experiment give contradictory results under the same conditions, experiment is always right.

Based on the above beliefs, we intend to make as less assumptions as possible in our simulations. In polymer crystallization research, only anisotropic interaction and Metropolis algorithm are assumed. Unlike other simulations,[10,11] we make no assumption on how the crystal front grows, and did not artificially disable certain types of desorption or rearrangement events. In fact, the program can not distinguish all four events (adsorption, desorption, diffusion, and rearrangement) based on their physical meanings. All four events are treated by the program as a single type of Metropolis-

weighted random walk. When we first set up and run the simulations, we have no idea what the results would be, such as the temperature-dependent roughness or the dependence of melting points on crystallization temperature. We just tried to explore the parameter space as widely as possible (over wide temperature and concentration ranges) and honestly recorded the simulation results, and then compare with experimental results – to find out what is consistent and what is inconsistent and figure out why. So it is more like a computer experiment. No attempt has been made to add an additional energy term, like some theorists do, to modify the simulation results, in order to fit the experiments. Because simulation is apparent and the trajectories of each particle are recorded, we are able to count the rates of 1-, 2-, 3-, 4-neighbor desorption events separately. This is very helpful for us to figure out why both low-T and high-T roughenings exist. The transparency of simulation is also helpful for proposing a theoretical equation for growth rates (we can count the adsorption and desorption rates separately and see how each depends on environmental parameters).

1.2.2 Big Picture

Unlike an experimentalist, a good simulationist has to be aware of the progresses in all three areas: simulations, theories, and most importantly experiments. The simulationist has to read tons of references and figure out what experimental findings are commonly observed and reliable, and what experimental findings are ad-hoc and unreliable. Only reliable experimental data are compared with the simulation results. Because of the easiness in running simulation experiments (in comparison with running real experiments), simulations are usually performed over a wider range of

parameter space, revealing a bigger picture than most experiments can do. For example, a Ph.D. thesis of an experimentalist focuses on only one subject, the nonlinear Hoffman-Weeks plot, where the plot of melting points versus crystallization temperature is used to extrapolate the equilibrium melting point. In our simulations which cover a wider temperature range (130°C) than theirs (20°C), we have found that the line deviates and reaches a plateau at low temperatures (which was seen in experiments for certain polymers too). And we found out that the slope of the plot strongly depends on the heating rate. Both our findings seriously challenge the validity of doing such a nonlinear extrapolation based on the data over a narrow temperature range and at a fixed finite heating rate. In our simulations, we have studied not only the effects of crystallization temperature, but also the effects of crystallization time, heating rate, polymer concentration, and crystal sizes. Standing at a higher altitude (exploring a wider parameter space), it becomes easier to see a bigger picture, thus leading to a "more likely" correct conclusion. The other way to see the big picture is to do interdisciplinary research. I would like to thank my advisor, Prof. Muthukumar, who first pointed out the similarity between the growth curves of amyloid fibrillization and polymer crystallization and introduced me into this new field. As I delved into the amyloid field deeper, I gradually realized that two facially different fields actually share the same underlying principles, such as the existence of induction time (or lag time), the seeding (or nucleation) phenomenon, and the Ostwald ripening growth mechanism. Both fields are concerned with an attractive-interaction-driven aggregation process into a more ordered structure (either two-dimensional lamella or semi-one-dimensional fibril). Performing interdisciplinary research is very beneficial and exciting, because

certain known ideas or facts in one field could be entirely new or unknown to another field. For example, the bell-shaped dependence of growth rates on temperature is a known fact for the polymer crystallization field, but remains unnoticed in the field of amyloid fibrillization. The corresponding inverse-bell-shaped dependence of lag time on temperature in the polymer crystallization field leads us to propose that there are two types of lag times for the amyloid fibrillization field. Another example is the Ostwald ripening mechanism which has been widely recognized in the fields of grain growth and polymer phase separation. However, Ostwald ripening remains unnoticed by the amyloid community. In the present dissertation, it is a key mechanism we would propose to explain some puzzles encountered by the amyloid community.

CHAPTER 2

CHAIN PREFOLDING

2.1 Introduction

Among the numerous theoretical attempts to understand the various experimental results on polymer crystallization, two popular models have been extensively attempted to interpret experimental data. These are the Lauritzen-Hoffman (LH) surface nucleation model[1,2] and the Sadler-Gilmer (SG) rough surface model.[3-7] Both theories assumed that chains have to *fold on* the growth front (the edge of the preformed polymer crystal), in contrast to the view in the present dissertation that chains *fold before* approaching one another. Figure 2.1a illustrates the secondary nucleation concept behind the LH theory.[1] In dilute solutions where polymer chains are isolated from one another, the primary nucleus is formed first from a single polymer chain. Once the primary nucleus has been formed, its flat side surface can serve as the growth front so that other polymer chains can grow on it via a secondary nucleation mechanism. The secondary nucleation concept is essentially a one-dimensional (1D) stem nucleation, where the length of the first stem of the chain attached on the growth front fluctuates with time until it is longer than the critical length, $L > L^*$. After the first stem is formed with certain surface energy penalty, additional stems can quickly attach next to the first stem one by one without paying surface energy penalty. This critical length L^* is analogous to the critical nucleus size R^* employed in the traditional three-dimensional (3D) nucleation theory. Sadler[4] criticized this secondary (stem) nucleation concept based on the fact that there should be no nucleation barrier

for 1D growth. Anyway, the LH secondary nucleation theory was successful in explaining two key results to a certain degree: temperature dependences of lamellar thicknesses and lateral growth rates, as described in the following two equations,

$$L = L^* + \delta L = \frac{A}{\Delta T} + \delta L \tag{2.1}$$

and

$$G \propto \exp\left(\frac{-K}{T\Delta T}\right) \tag{2.2}$$

where A is a constant, δL is a small value in comparison with L^*. The supercooling ΔT is defined by $T_m^{\,0} - T$, where $T_m^{\,0}$ is the extrapolated equilibrium melting temperature for an infinitely large crystal, T is the crystallization temperature, G is the radial growth rate of lamellae, and K is the nucleation constant. The exponential dependence of G on T suggests the existence of nucleation, which was actually one of the motivations for Lauritzen and Hoffman to propose the secondary nucleation concept.

Unfortunately, based on current experimental techniques, it is not able to see directly how polymer chains in solutions diffuse, change their conformations, and aggregate into a two-dimensional (2D) crystal lamella. Simulation becomes a handy tool to study the chain folding process at microscopic scale. Single chain self folding has been observed in many simulations.[12-16] If the polymer solution is dilute enough, it is reasonable to assume that chains prefold before they meet and interact with one another, as illustrated in Figure 2.1b. In addition, polymer chains were observed in simulations to adsorb onto the growth front spontaneously without invoking any energy barrier,[13,17] in direct contradiction with the stem-nucleation-based LH theory. When two bundles of chains come closer, they simply attract each other and merge into a bigger

bundle (lamella).[12] In experiments, there is increasing evidence of the presence of nodular (bead-like) structures in polymer crystals grown from either melt[18] or solution[19], which is a further support to our prefolding concept. Moreover, Equation (2.1) is actually not valid over a wide temperature range, as observed in experiments.[20] It was found that the lamellar thickness L reaches a constant plateau at low temperatures.[20] Simulations by two independent groups[13,21] have confirmed that the finite thickness is actually at the global minimum of free energy, rather than kinetically trapped in a local minimum (arguments in the LH theory). This suggests that a finite thickness is an equilibrium result. The concept of the "predetermined thickness" is further supported by "isochronous decoration" experiments,[22,23] where L and G was found to be independent of the previous substrate upon alternative heating and cooling.

2.2 Model and Simulation Algorithm

There are two major groups of force field (potential energy) parameters for studying chain folding. The major difference lies in the setting for the torsion energy. In Welch's model,[13] the torsion potential parameters are so set that the difference of the energy levels between gauche and trans conformations is large. A typical fold can be formed by four gauche conformations at the folding point and fifty trans-conformations along the extended stem. If the gauche energy level is too high, the chain becomes fully extended (all trans conformations). If the gauche energy level is too low, the chain collapses into a globule (many gauche and trans conformations coexist). In the models by Paul,[24] Chester,[12] and Waheed,[25] the energy level difference between gauche and trans conformations is small. In order to form chain folding, bead 1 and 4 (next next

nearest neighbors, separated by three bonds) have to interact with both torsion and van der Waals forces. Existence of a repulsive van der Waals interaction between bead 1 and 4 actually favors the trans conformation and essentially enlarges the energy gap between gauche and trans conformations, thus leading to a similar result as Welch's model. Although there is no consensus on the force fields for chain folding, we are more interested in kinetics of chain folding and aggregation. The choice of the exact force fields should not affect our general results regarding the kinetics. In the present dissertation, the force field parameters are modeled after the paper by Chester and Muthukumar.[12]

The united atom model for polyethylene is chosen for a polymer chain, where each methylene unit is modeled as a bead in a bead-spring model. The typical chain length in our simulations is 500 united atoms. The simulation is performed under periodic boundary conditions. The total potential energy consists of the potential energies arising from bond stretching U_l, bond angle bending U_θ, bond torsion U_ϕ, and nonbonded Lennard-Jones interaction U_{LJ}. The potential energy associated with bond stretching is taken to be

$$U_l = K_l \left(l - l_0\right)^2 \tag{2.3}$$

where l is the bond length and l_0 is the equilibrium bond length. The spring constant K_l is taken to be 350 kcal/mol/Å^2 and $l_0 = 1.53$ Å. The potential energies associated with bond angle θ and torsion angle ϕ are assumed to be of the form

$$U_\theta = K_\theta \left(\theta - \theta_0\right)^2 \tag{2.4}$$

and

$$U_{\phi} = K_1(1-\cos\phi) + K_2(1-\cos 2\phi) + K_3(1-\cos 3\phi) \tag{2.5}$$

where $\theta_0 = 109^\circ$, $K_\theta = 60$ kcal/mol, $K_1 = 0.8$ kcal/mol, $K_2 = -0.43$ kcal/mol, and $K_3 = 1.62$ kcal/mol. The Lennard-Jones potential U_{LJ} is

$$U_{LJ} = \varepsilon\left[\left(\frac{\sigma}{r}\right)^{12} - 2\left(\frac{\sigma}{r}\right)^{6}\right] \tag{2.6}$$

where the interaction strength $\varepsilon = 0.112$ kcal/mol, and the equilibrium distance is 4.5Å. The Lennard-Jones interaction contains a coefficient of 2 for the attractive part so that the minimum of this potential occurs at $r = \sigma \approx 3l_0$. Therefore bead 1 and 4 are repulsive so that trans conformation is preferred (as a tradition, the Lennard-Jones interactions between the nearest or the next-nearest neighbors are disabled, because those interactions are already included in bond stretching and bond angle potentials). For the actual computation, reduced units are used throughout and all data presented are expressed in terms of the reduced units. The units have been renormalized to a united-atom mass m of 1, an equilibrium bond length l_0 of 1, and a Lennard-Jones ε of 1. It follows that the reduced temperature, T^*, is equal to $k_B T / \varepsilon$, the reduced energy is E / ε, and the reduced time is $t\sqrt{\varepsilon / m\sigma^2}$.

The equations of motion are integrated according to Langevin Dynamics.[26] The motion of the particles is described by the Langevin equation which consists of inertial terms, force field, friction drag, and noise, respectively.

$$\ddot{r}_i = -\nabla U_i - \Gamma \dot{r}_i - W_i(t) \tag{2.7}$$

The effects of solvent molecules are implicitly included in the friction term and the noise term. The friction coefficient Γ is related to the autocorrelation function of W through the fluctuation-dissipation theorem,

$$\langle W_i(t) \bullet W_i(t') \rangle = \delta_{ij} \delta(t-t') 6 k_B T \Gamma \tag{2.8}$$

where Γ is set to 1, between the over-damped regime and the purely deterministic regime. Velocity verlet finite-differencing scheme is used for integration.[26] The average time step used in the data presented is about 0.01. One time unit in the simulation is estimated to be about 10^{-10} second. The precise relationship between the simulation time unit and the actual time is not yet established.

2.3 Results and Discussion

Since the melting temperature was estimated as 11.0±0.2,[12] we have chosen T^*=8 and performed simulations in the simulation box of different sizes. For the box length of 200, it is shown in Figure 2.2a that five chains of 500 beads quickly fold by themselves into ordered bundles. Because it takes too long time to observe aggregation of these bundles, smaller box lengths have been tried, as shown in Figure 2.2bc. In Figure 2.2b, it is observed that a prefolded bundle approaches and slide in another bundle. In Figure 2.2c, the last prefolded chain attach laterally on the growth front formed by the previous four chains. Both slide-in and lateral attachments are not hindered by any barrier, but instead are driven by van der Waals attractive interactions. These observations support early simulation results[12,13] and the prefolding concept, in direct contradiction with the secondary nucleation concept in the LH theory.[1]

In addition, we calculated the radius of gyration (which should be proportional to the lamellar thickness) of single chain of 500 beads at different reduced temperatures, as depicted in Figure 2.3a. Clearly, there is a plateau in the low-T range. This plateau was actually confirmed in experiments and led to a so-called "δL catastrophe". According to Equation (2.1), the δL term should increase quickly in the low-T range, which has never been seen in experiments. Instead, the lamellar thickness shows a wide plateau in the low-T range. These low-T experimental data can not be fit by Equation (2.1) no matter what parameter value is input, as illustrated by the upswing curves in Figure 2.3b. So δL catastrophe has seriously undermined the foundation of the LH theory. In contrast, we propose that the lamellar thickness obtained is an equilibrium result based on the competitions between torsion energy, van der Waals interactions, and kT (i.e., the heat bath). Unlike the view in the LH theory that the critical thickness L^* is strongly correlated with the growth rate G, our simulation results suggest that the lamellar thickness is predetermined before aggregation, and thus L and G are uncorrelated.

2.4 Conclusions

Langevin Dynamics simulations of polymer chains in dilute solutions suggest that chains are prefolded before aggregation, consistent with single-chain simulation studies. The aggregation of prefolded chains occurs by either slide-in or lateral attachment mechanism. Either way, the aggregation is driven by van der Waals attractions and not hindered by secondary nucleation barrier, in agreement with other simulations[13] but in contradiction with the LH theory. The LH theory is further

criticized by δL catastrophe – a plateau of lamellar thickness in the low-T range which can not be fitted by the existing theory. Our simulation results are consistent with experimental results by showing a thickness plateau in the low-T range, suggesting that the lamellar thickness might be a predetermined equilibrium result and uncorrelated with crystal lateral growth. The prefolding concept is also supported by observations of nodular structures in polymer crystals.[19] In the next three chapters, these prefolded chains are to be taken as the smallest dynamic units in our Monte Carlo simulations, where the prefolding concept is further tested by comparing simulation results with experimental ones in terms of macroscopic properties such as morphology, growth rates, and melting points.

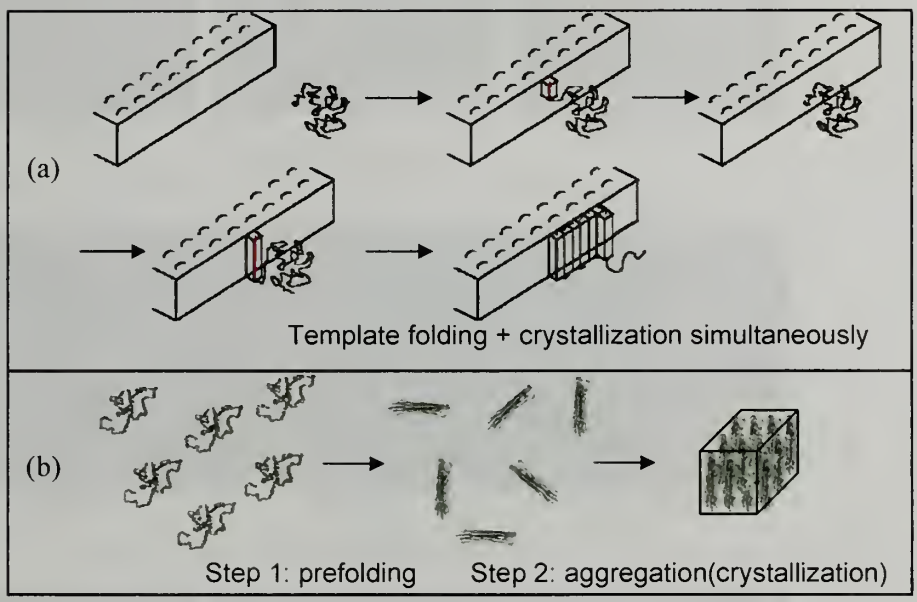

Figure 2.1: (a) Chain folding occurs during the crystallization process and is facilitated by the growth front template, i.e., secondary nucleation. (b) Chain folding occurs before the aggregation (crystallization) process and is not facilitated by other chains or the growth front, i.e., self prefolding.

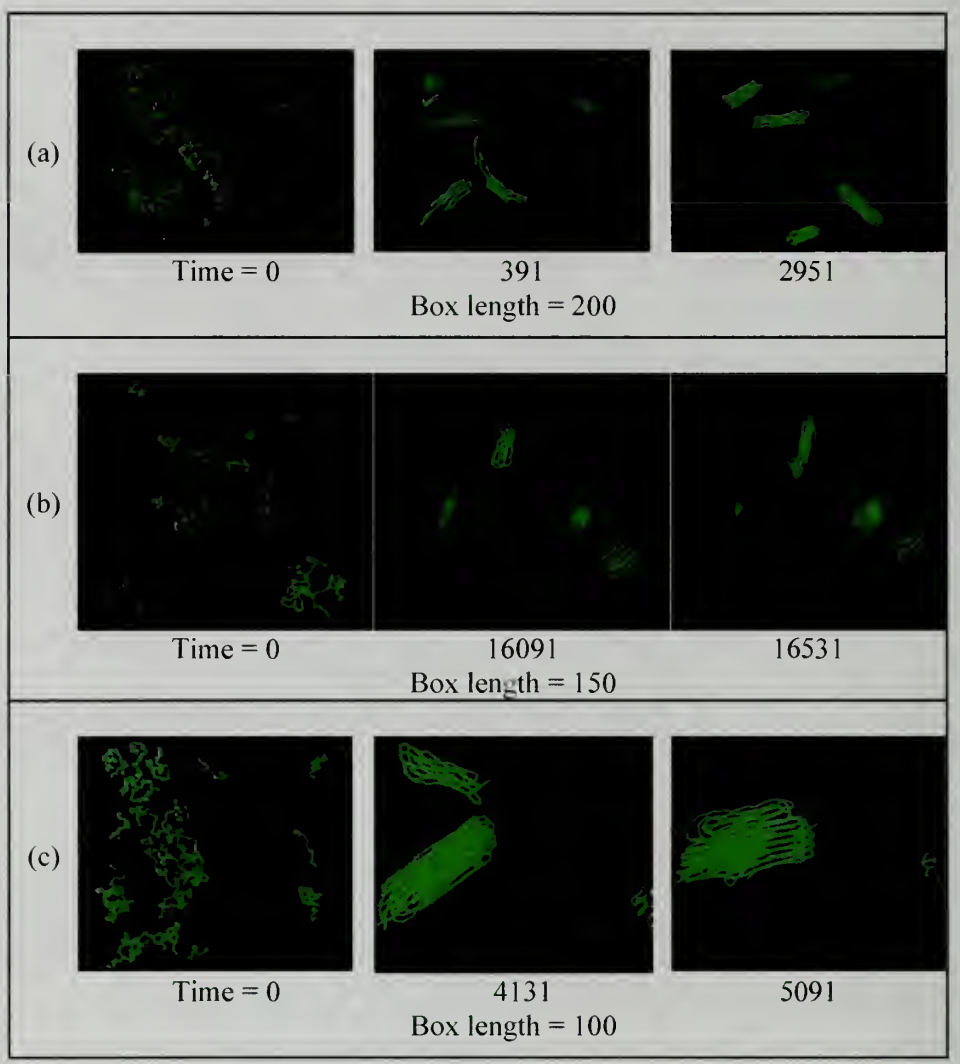

Figure 2.2: Five chains of 500 beads prefold by themselves into bundles. These bundles aggregate by attractive van der Waals interactions (no stem nucleation barrier).

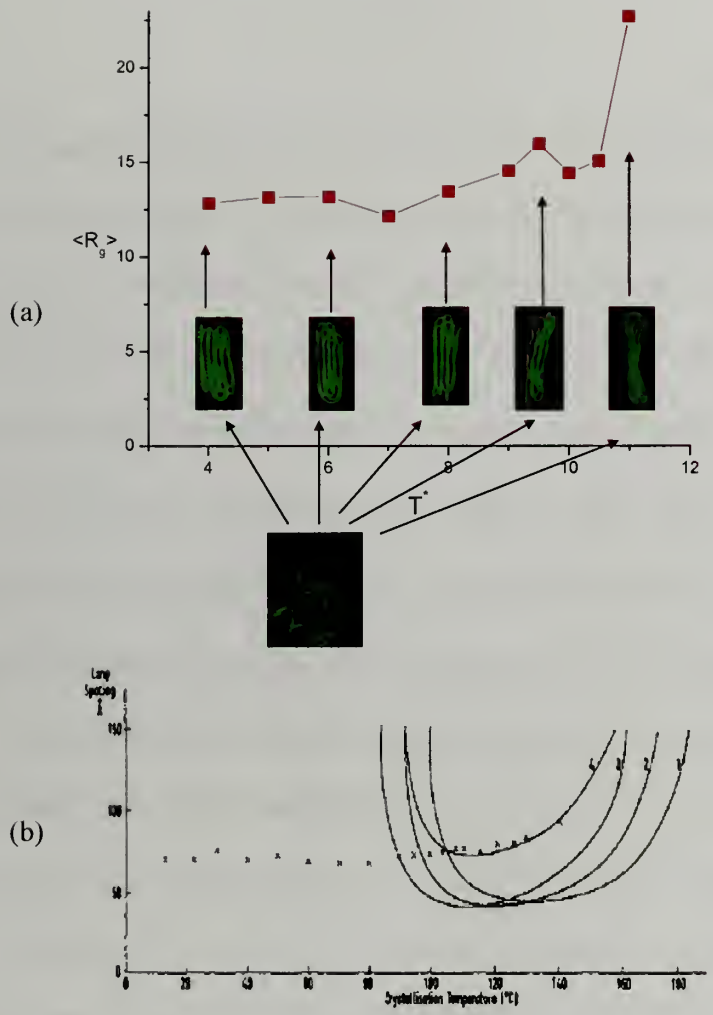

Figure 2.3: (a) Time-averaged radius of gyration of single chain of 500 beads at different temperatures. Each data point is averaged over five different runs. (b) Lamellar thickness as determined by low-angle x-ray diffraction as a function of crystallization temperature for isotactic polystyrene from dimethyl phthalate. Theoretical relation in Equation (2.1) can not fit with experimental results even for different parameter values.

CHAPTER 3

SINGLE CRYSTAL

3.1 Introduction

As described in the previous chapter, the exponential dependences of lamellar thickness L (Equation (2.1)) and lateral growth rate G (Equation (2.2)) on temperature are two key results and motivations for the LH theory. Equation (2.1) has encountered the δL catastrophe. Equation (2.2) is not perfect either. First, the key term ΔT in Equation (2.2) requires the knowledge of the equilibrium melting point T_m^0 of an infinite large crystal. T_m^0 is an ideal value extrapolated from the plot of T_m versus $1/L$. However, T_m^0 has not been determined accurately and uniquely for most polymers (except polyethylene),[27,28] presumably due to the problem of continuous lamellar thickening during the measurements. The second problem with Equation (2.2) is that the plot of $\log G$ vs. $1/T\Delta T$ is not necessarily linear but showing slope changes or curvature.[29] The concept of I-II [30] and II-III [31] regime transitions were introduced, where the slope K in Equation (2.2) decreases or increases with lowering T, respectively. The LH theory interpreted three regimes as a result of competition between the surface nucleation rate i of the first stem and the substrate completion rate g of subsequent stems:[32] Regime I at high temperatures corresponds to a mononucleation region where $i \ll g$. The surface nucleation i is the rate-determining step and the substrate completion g is so rapid that the growth face tends to be flat; Regime II at intermediate temperatures corresponds to a multiple-nucleation region

where $i \approx g$ and the growth front starts to show some roughness; Regime III at low temperatures corresponds to an excessive-nucleation region where $i \gg g$ such that the niche separation is of the order of the stem width. Apparently the above analysis leads to a conclusion that the crystal outline becomes rougher at lower temperatures, a phenomenon known as "kinetic roughening". In experiments, most of the regime transitions were found to be I-II and II-III types,[32,33] with a few exceptions where III-II-I [34,35] and III-II-I-II [36,37] type transitions were also observed.

The concept of regime transitions was criticized by Point and Janimak[38] in terms of unrealistic values of the substrate length and kinetic length. Another problem with the LH regime transition theory is that the slope change in the plot of $\log G$ vs. $1 / T\Delta T$ is not concomitant with the morphological change at the same regime transition temperature.[34,39] More importantly, the LH theory can only account for "kinetic roughening" phenomenon (roughness at lower temperatures), but encounter difficulties in explaining "thermal roughening" phenomenon (roughness at higher temperatures).[3] In experiments, the axial ratio and the curvature of polyethylene crystal outlines were observed to increase with temperature,[39,40] raising serious doubts on the validity of the LH theory at higher temperatures.

In order to account for thermal roughening at higher temperatures, Sadler and Gilmer applied the "rough surface growth" model developed for crystal growth of small molecules to the case of polymers and proposed an alternative model for polymer crystallization.[3-7] In this model, the surface roughness requires that the binding energy between units in the crystal, ε, is comparable with kT, where k is the Boltzmann constant and T is the absolute temperature. Hence the smallest dynamic unit was

estimated to be a segment of a polymer chain (ca. 6 $-CH_2-$) in the SG model rather than a complete stem (ca. 80 $-CH_2-$) in the LH theory. Sadler argued that nucleation may be a more important barrier at low temperatures but not at high temperatures. However, the original rough surface growth model for small molecules predicted that the growth rate G is linear with supercooling,[3]

$$G \propto \Delta T \tag{3.1}$$

which apparently contradicts with the experimental fact that the growth rate of polymer crystals varies nonlinearly with temperature conforming to Equation (2.2). In order to account for this discrepancy, Sadler and Gilmer[5] introduced another new concept, a pinning entropic barrier, to replace the surface nucleation barrier in the LH theory. The pinning barrier represents a trap created by crystallization of a stem shorter than L^* in Equation (2.1). Further crystallization next to this short stem with $L > L^*$ has a disadvantage due to the expense for the creation of new side surfaces. Therefore crystallization is interrupted by the short stem, and this pinning stem has to be removed by fluctuations in order to resume the crystallization.[6] The thicker the lamella is, the less likely the pinning stem is removed by fluctuations. In this sense, the pinning effect was considered as an entropic barrier whose magnitude increases linearly with lamellar thickness. Hence the growth rate limited by this pinning effect has the same exponential dependence on the supercooling as that limited by nucleation. By introducing pinning effects into the rough surface growth, the SG model can qualitatively reproduce the temperature dependences of both L in Equation (2.1) and G in Equation (2.2) without invoking secondary nucleation concepts, as demonstrated by Monte Carlo simulations[4,5] and rate equation approach.[6,7]

However, the pinning concept becomes questionable because pinning should result in a tapered edge,[4] which contradicts with direct AFM observations.[41,42] More importantly, the SG model only takes thermal roughening into account and leaves kinetic roughening unexplained, in the direct opposite direction with the LH theory. Our Monte Carlo simulations described below demonstrate that both kinetic and thermal roughenings can be realized by merely varying temperature, without invoking either surface nucleation or entropic pinning concepts. Our simulation results also reproduced the exponential dependence of G on T in Equation (2.2). We argue that Equation (2.2) is merely a good fitting function as long as an appropriate T_m^0 is chosen.

The salient assumptions of our Monte Carlo simulations for polymer crystallization from dilute solutions with polymer concentrations below the overlap concentration may be summarized as follows:

1. The smallest dynamic unit is a complete chain (a prefolded bundle), rather than a stem in the LH theory or a segment in the SG model.
2. The crystal thickness is mainly predetermined in Step 1 and is assumed to be decoupled with the crystallization kinetics in Step 2, distinct from the underlying assumptions in the LH/SG models that L and G are strongly correlated.
3. The crystallization (adsorption) and melting (desorption) are fully reversible, in line with the SG model[3-5] but in contradiction with the LH theory. Hence the adsorption process is not hindered by a barrier but favored by van der Waals attractions.
4. An anisotropic interaction is introduced, distinct from the isotropic binding energy in the SG model. This leads to a roughness on the lateral surface alone for our

model, instead of the roughness on both lateral and fold surfaces for the SG model.[4,5]

3.2 Model and Simulation Algorithm

We model the crystallization of polymers in dilute solutions as an anisotropic aggregation process, belonging to the same category as the q-state Potts model with conserved order parameter. Our model shares some features with other models used in simulations of grain growth in liquid phase sintered materials,[43-45] crystal growth in a transdermal drug delivery system,[46] and diffusion-limited polymer crystallization in the thin film.[10]

Simulations are performed in a cubic simulation box with length L_{box}, under periodic boundary conditions. The box is further discretized into ${L_{box}}^3$ cubic lattices, each with length 1. L_{box} varies from 100 to 500 in this work. Each cubic lattice is assigned a state from five possible states, as shown in Figure 3.1: state S_0, solvent cubic lattice; state $S_1 \sim S_3$, x-, y-, and z-oriented free chain (diffusing prefolded bundle in solutions); state S_4, z-oriented crystalline chain which serves as the nucleus for subsequent crystal growth.

The simulation procedure is as follows:

1. Put a small z-oriented seed nucleus (S_4) with length R_0 at the origin of the simulation box. The initial seed nucleus is fixed and not movable throughout the simulation.

2. Put a specific number (${L_{box}}^3 \times C$, where C is the initial polymer concentration) of free chains with random orientations ($S_{1\sim3}$) at random locations in the simulation box. The rest of lattices are assigned to solvent (S_0).
3. Randomly pick one chain ($S_{1\sim4}$, where S_4 appears after the crystallization in Step 6). Let it undergo random walk and randomly change its orientation ($S_{1\sim3}$). Note that a crystalline chain (S_4) has to be converted to a free chain ($S_{1\sim3}$) in this step.
4. If the random walking direction is blocked by another chain, quit the walk and go back to Step 3.
5. Calculate its energy state before (E_0) and after (E_1) such a random walk. Decide whether to accept such a random walk based on the acceptance probability in the classical Metropolis algorithm:[47]

$$P = \begin{cases} 1 & \text{when} \quad \Delta E \leq 0 \\ \exp\left(\dfrac{-\Delta E}{kT}\right) & \text{when} \quad \Delta E > 0 \end{cases} \tag{3.2}$$

   where the energy change $\Delta E = E_1 - E_0$.
6. If the chain after the random walk is z-oriented (S_3) and has at least one crystalline chain (S_4) in its 4 nearest neighbors along x and y directions, this chain (S_3) will be further converted to a crystalline chain (S_4).

Repeat Step 3~6 for several billion times. The number of iterations is given in units of Monte Carlo step (MCS). At 1 MCS, the number of attempted random walks is equal to the total number of chains ($S_{1\sim4}$) in the simulation box. As is conventional for Monte Carlo simulations, all temperatures are given as kT . The initial random configuration of free chains is to mimic the athermal state of polymer solutions above

the melting temperature. Then kT parameter is set to a constant value so that the whole process of simulation is to mimic an isothermal crystallization process at kT after quenching from a temperature above the melting temperature. It is to be noted that a chain may crystallize ($S_{1\sim3} \overset{Step\ 3}{\rightarrow} S_3 \overset{Step\ 6}{\rightarrow} S_4$), melt ($S_4 \overset{Step\ 3}{\rightarrow} S_{1\sim3}$), rearrange along the growth front ($S_4 \overset{Step\ 3}{\rightarrow} S_3 \overset{Step\ 6}{\rightarrow} S_4$), or diffuse ($S_{1\sim3} \overset{Step\ 3}{\rightarrow} S_{1\sim3}$) depending on whether the criteria in Step 6 are satisfied.

The energy state of the chain before/after random walk is calculated by counting how many crystalline chains (S_4) are in its 6 nearest neighbors and what interaction these neighbors give:

$$E = \varepsilon_{x1}\left(S_i, S_4\right) + \varepsilon_{x2}\left(S_i, S_4\right) + \varepsilon_{y1}\left(S_i, S_4\right) + \varepsilon_{y2}\left(S_i, S_4\right) + \varepsilon_{z1}\left(S_i, S_4\right) + \varepsilon_{z2}\left(S_i, S_4\right) \quad (3.3)$$

where $x1, x2, y1, y2, z1, z2$ correspond to 6 nearest neighbors, and the subscript i denotes the current state of the chosen chain. Here the local anisotropic interaction is simply defined as attraction ($\varepsilon_p < 0$) between two neighboring parallel chains and repulsion ($\varepsilon_n > 0$) between two neighboring non-parallel (end-to-end or perpendicular) chains. Since only the dimensionless ratio $\Delta E / kT$ is employed in calculating the acceptance probability, we reduced ε_p to unity and determined kT values by trial and error. It turned out that meaningful results were obtained only in the range of $kT = 0.13 \sim 0.20$, below or above which the crystal grows too fast or melts. After setting $\varepsilon_p = -1$, for simplicity, we further set $\varepsilon_n = +1$. Different magnitudes of $\varepsilon_n = +1 \sim +5$ have been tried and the results showed no difference as long as a certain repulsion exists to avoid non-parallel aggregation of chains. The following equation gives more detailed energy setting:

$$\begin{cases} \text{parallel:} & \varepsilon_{xy}(S_3,S_4) = \varepsilon_{xy}(S_4,S_4) = -1 \\ \text{end-to-end:} & \varepsilon_{z}(S_3,S_4) = \varepsilon_{z}(S_4,S_4) = +1 \\ \text{perpendicular:} & \varepsilon_{xyz}(S_1,S_4) = \varepsilon_{xyz}(S_2,S_4) = +1 \end{cases} \tag{3.4}$$

where the subscript x, y, z correspond to 6 nearest neighbors along x, y, z directions. Only the interaction with crystalline chains (S_4) was considered, i.e. omitting interactions between free chains ($S_{1\sim3}$) to avoid forming multiple crystals. So the present study focuses on single crystal growth starting only from a preset seed and to mimic heterogeneous nucleation in nature. In contrast, homogeneous nucleation and competitive growth of multiple crystals will be the focus of future work.

For simplicity, we assume that ε_p is a constant. In both experimental[20] and simulation[12] results, the lamellar thickness increases slightly at higher temperatures, suggesting that ε_p should also increase slightly in the high-T region. However, as the thickness increases, the width of the prefolded bundle decreases, and the chain conformation becomes less ordered. The latter two effects might compensate for the contribution of larger thickness to the van der Waals attraction, leading roughly to a constant ε_p over the whole temperature range.

3.3 Results and Discussion

3.3.1 Crystal Habit

In spite of the fact that the microscopic details at length scales less than a chain are completely ignored, it turns out that the present simulations are able to capture the general trends in the crystal habits at different temperatures and concentrations. First,

we give a summary of key experimental results extracted from the literature. Next, we give the simulation results, followed by a discussion.

The study of Wunderlich *et al.*[48] showed that polyethylene grows from dilute o-xylene in the form of faceted lozenge-like crystals at 84°C [Figure 3.2(2)]. Below 80°C the angle of the crystal apex becomes increasingly sharpened with decreasing temperature, leading to a sharpened-apex lozenge at 75°C. At even lower temperature[48] or higher concentrations,[49] the crystal becomes more dendritic, resulting in a hedgehog dendrite. Similarly, Holland and Lindenmeyer[50] observed a transition from faceted lozenges at 80°C to dendritic structures at 40°C [Figure 3.2(1)]. This trend was further confirmed by Kloos *et al.*'s observations[51] that truncated, faceted, and sharpened-apex lozenges were formed at 82°C, 75°C, and 45°C, respectively. The transition from faceted habits to sharpened-apex lozenges and then to dendrites indicates a transition of underlying mechanism from nucleation-controlled to diffusion-limited growth.[52] Free chains with random diffusion path prefer landing on the outer region of the lozenge (the apices sticking out) to the inner part (screened by the apices), which results in sharpened apices or even dendritic structures. Regarding the kinetic roughening (i.e. low-T roughening), Tanzawa[53] observed that the outline of the lamella grown from isotactic polystyrene solution transformed from a hexagon at 130°C to a more rounded circle at 110°C [Figure 3.2(3)]. Yamashita *et al.*[54] also observed that the morphology of isotactic poly(butene-1) in the melt film transformed from a square faceting shape at 100°C to a rounded and wavy habit at 85°C. Hitherto, the kinetic roughening has been explained as a result of $i \gg g$ in the LH theory. For the thermal roughening (i.e., high-T roughening), Organ and Keller[39,40] found that at higher temperatures, the crystal habit

becomes more rounded and elongated [Figure 3.2(4)], in direct contrast to the prediction of the LH theory. Several mechanisms have been advanced[3,55-57] to understand the thermal roughening. Sadler[3] argued that the crystal outline become thermally roughened at molecular scale when the binding energy between segments becomes comparable with kT.

The middle part of Figure 3.2 presents our typical simulation results. With increasing temperature and lowering concentrations, the crystal habit exhibits five different types: dendritic structure → sharpened-apex lozenge → kinetic roughening → faceting → thermal roughening. At high $C = 0.004$ and low $kT = 0.10$, the crystal outline is dendritic, as seen in Figure 3.2(5). At intermediate $C = 0.0005$ and low $kT = 0.09$, a sharpened-apex lozenge is formed [Figure 3.2(6)]. At low $C = 0.00002$, a well-defined faceting is formed at intermediate $kT = 0.135$ [Figure 3.2(8)]. At the same concentration, the rounding habit caused by kinetic roughening [Figure 3.2(7)] or thermal roughening [Figure 3.2(9)] appears at lower or higher temperatures, respectively. The lower part of Figure 3.2 gives schematic drawings of the corresponding habits. By comparing the upper, middle and lower parts in Figure 3.2, the one-to-one correspondence between simulation results and experimental pictures is clearly seen. The reason why the faceting of Figure 3.2(8) deviates from a lozenge shape is because the building block in simulations is in a square shape, while in reality chain stems in the orthorhombic unit cell are stacked in a lozenge shape. Therefore a coordination transformation will eliminate the difference. One might consider dendrites and sharpened-apex lozenges as the extreme cases of kinetic roughening. This

classification, however, is deemed inappropriate because the former two are diffusion-limited in nature while kinetic roughening should be interface-controlled.[58]

In order to quantify the above observations, a roughness parameter (RP) is defined as the average number of crystal-solvent interfaces along the x, y directions per edge crystallite:[3]

$$RP = \frac{n_1 \times 3 + n_2 \times 2 + n_3 \times 1}{n_1 + n_2 + n_3} \tag{3.5}$$

where n_i is the total number of *i*-neighbor crystallites, where "*i*-neighbor" denotes how many crystal-crystal interfaces it has (see Figure 3.8 for the definition). The asymptotic values of RP are 1 and 2, respectively, for fully facetted and fully serrated habits. The temperature dependence of RP at different concentrations is given in Figure 3.3. The RP depends on temperature non-monotonically. As the temperature is increased, RP decreases from a higher value, reaches a minimum, and then increases again. This result is a representation of the rough-flat-rough transition observed experimentally. This trend is noted for all concentrations in Figure 3.3, although it is more pronounced at lower concentrations. Figure 3.3 also offers a plausible explanation of why a perfect faceting is obtainable only in dilute solutions[33] and within a narrow temperature range.[48]

3.3.2 Time Evolution of Lamellar Size

Figure 3.4 presents time evolution of the lamellar size R as a function of temperature. The lamellar size is defined as the square root of the number n_c of chains in the lamella, i.e. $R = \sqrt{n_c}$. It is observed that R initially increases linearly with time

and then attains a plateau value as the polymer chains become exhausted, in agreement with experimental results.[50,59] At high temperatures, there emerges an additional stage right before the crystal growth, i.e. a nucleation stage, where the crystal is observed to grow and redissolve back until its size exceeds a critical nucleus size R_c. It is noteworthy that the shape of the nucleus is not necessarily in a faceted shape, and can be rough and irregular from time to time. For $R > R_c$, the crystal has a greater tendency to grow than to shrink. For the conditions in Figure 3.4, the critical nucleus size is in the range, $\sqrt{75} < R_c < \sqrt{90}$. In general, the behavior of R vs. t can be divided into three stages: (1) nucleation stage; (2) linear growth stage; and (3) equilibrium stage. Our results are in full agreement with the recent scattering data of Wang.[60] Both our simulation results and Wang's experimental data exhibit the following features: As temperature is raised, the length of the nucleation stage becomes longer, the slope of the linear growth stage becomes shallower, and the height of the final equilibrium stage becomes lower.

3.3.3 Induction Time and Critical Nucleus Diagram

The duration of the nucleation stage, called the "induction time", τ, is measured in experiments as the time at which the crystallinity becomes detectable. Here we make the choice of the detector limit as $R = 10$ for reporting τ. This arbitrary choice is made for the convenience of correctly discounting wild fluctuations in crystal size, e.g., the size fluctuation of sub-critical nucleus ($R < R_c$) can be as high as $\sqrt{75} = 8.7$, as shown in Figure 3.4. After performing 50 independent runs with different random number seeds, it is found that τ has a lognormal distribution and such a distribution

becomes broader at higher temperature (data not shown). The average values of τ are given in Figure 3.5a as functions of temperature and the nucleus size. As seen in Figure 3.5a, τ increases exponentially with an increase in kT, in good agreement with experimental results.[61] Surprisingly, the $\tau - T$ curve also depends significantly on the seed size R_0. For larger R_0, the $\tau - T$ curve shifts to higher kT, as expected for the seeding phenomenon (i.e., only larger seeds can grow crystals at higher temperatures). And the shifting distance is increasingly narrower as R_0 increases evenly. According to the classical nucleation theory, the induction time must correspond to the time required for the formation of the crystal with the critical size R_c. If the seed size R_0 is much smaller than R_c, τ tends to infinity. On the other hand, if R_0 is much larger than R_c, τ is zero. For R_0 comparable to R_c, τ is a finite value close to zero. Therefore, the transition point of τ from very large values to the constant plateau is taken as $R_0 \approx R_c$. Here we choose the transition points as intersects of the horizontal line $\tau = 100 \times 10^4$ MCS with the four $\tau - T$ curves in Figure 3.5a. For different $R_0 = 1$~7, the transition point $R_c \approx R_0$ occurs at different temperature $kT = 0.146$, 0.179, 0.189, and 0.195, respectively. This information is utilized to construct temperature dependence of the critical nucleus size R_c in the inset of Figure 3.5a, where R_c is observed to increases exponentially with temperature. Such nonlinear dependence of R_c on kT is expected to be unaffected by the choice of the intersecting horizontal line, as long as the $\tau - T$ curve shifts to higher kT with increasingly narrower distance for larger R_0.

Using the same method as that in the inset of Figure 3.5a ($C = 0.00020$), the temperature dependences of R_c for four other concentrations ($C = 0.00005$, 0.00035, 0.00050, and 0.00065) are collected. Therefore R_c as functions of both kT and C can be constructed in the $T - C$ plane, as illustrated in Figure 3.5b. It is evident that R_c increases sharply as kT is increased or C is decreased, tending to diverge at some asymptotic points. Here we identify the asymptotic points as the melting points (the dashed curve), where even a very large crystal nucleus ($R_0 \to \infty$) would melt gradually rather than induce crystallization. Thus the two curves of $R_c = 1$ and $R_c \to \infty$ divide the plane into three regions for the growth of crystals from seeds: no growth region where $R_0 \ll R_c$ (infinite barrier), metastable region where nucleation might occur if $R_0 < R_c$ (finite nonzero barrier), and spontaneous growth region where $R_0 \gg R_c$ (zero barrier). The width of the metastable region is wider at lower concentrations. If we take R_c as an additional coordinate orthogonal to the $T - C$ plane, the four curves of $R_c = 1 \to 7$ constitute a surface, as shown in the inset of Figure 3.5b. Any state point (R_0, T, C) below this surface corresponds to $R_0 < R_c$ and $\tau > 0$; any state point above this surface corresponds to $R_0 > R_c$ and $\tau = 0$. Therefore, in order to reduce τ, any state point below the surface can penetrate through the surface by any of three directions: (1) increasing R_0; (2) decreasing kT; (3) increasing C. To our best knowledge, Figure 3.5b is of great importance because it is the first time to construct a phase diagram of critical nucleus sizes on the $T - C$ plane.

3.3.4 Lamellar Growth Rate

The lamellar growth rate G is calculated as the initial slope of R versus time in Figure 3.4. The temperature dependence of G is presented in Figure 3.6a for five different concentrations. It is found that G decreases exponentially with kT, consistent with the experimental results shown in Figure 3.6b.

As regards the concentration dependence of G, it is generally expressed by[62]

$$G \propto C^{\alpha} \tag{3.6}$$

where α is a constant normally ranging from 1/3 to 1,[29,59,62,63] with some exceptions where α is as high as 2.[62] Figure 3.6c presents our simulation results on the concentration dependence of G, which are very similar in shape to the experimental curves shown in Figure 3.6d. It is found that $\alpha = 1$ at low temperatures and at high concentrations, indicating that G is proportional to C when the crystal growth is diffusion-limited. With increasing temperature or decreasing concentration, α shows a transition from 1 to 2 or even higher values. As Keller and Pedemonte[62] suggested, $\alpha = 2$ indicates that a successful attachment requires the simultaneous arrival of two chains onto the growth front. There is much higher tendency for a single chain to leave the flat growth front, unless another chain arrives soon enough to stabilize both chains. The results presented in Figure 3.6c reveal several important trends which are fully consistent with experiments: (1) α increases with increasing temperature.[29,59,62] (2) α increases with decreasing concentration.[52,62,63] (3) All curves at various temperatures converge at higher concentrations.[62] (4) At lower temperatures, the crystal growth can take place at even lower concentrations.[52,63] In fact, closer inspection reveals that α is not constant but varies smoothly with lowering C. So, in a strict sense, Equation (3.6)

is not valid due to the nonconstant α. Although Toda et al.[52,63] claimed that the plot of $\log G$ vs. $\log C$ with their data exhibited two intersecting straight lines, closer inspection on their raw data reveals no apparent kinks but smooth curves. In literature, the cilia nucleation concept[64-66] has been introduced into the nucleation theory to explain the increase of α with an increase in temperature or a decrease in concentration. The present model, however, can capture these two trends without invoking the cilia nucleation concept.

3.3.5 Mechanism of Rough-flat-rough Habits

Figure 3.7 gives the total number of *i*-neighbor desorption events (*i*=1~3) in the late stage when the crystal outline has reached equilibrium. Because the desorption probability $P = \exp\left(\frac{-i}{kT}\right)$, the 1-, 2-, 3-neighbor crystallites have different thermal stability and tend to desorb at different temperatures, thus leading to different habits. At very low $kT < 0.10$, even 1-neighbor crystallites are stable so that once-adsorbed chains will never desorb. Now the crystal growth is dominated by diffusion of the free chains but not by the interface, thus leading to dendritic structures. For $kT > 0.10$, 1-neighbor crystallites start to become unstable so that 2-neighbor crystallites dominate to form a sharpened-apex lozenge. The sharpened apices are the remnants of the diffusion-controlled dendrites. For $kT > 0.12$, diffusion becomes unimportant and kinetic roughening shows up, where 1-neighbor crystallites are totally unstable and 2-neighbor crystallites are still partially stable. At $kT = 0.16$, both 1 and 2-neighbor crystallites are unstable so that 3-neighbor crystallites dominate to form a faceted habit. For $kT > 0.19$, 2-neighbor crystallites are totally unstable and 3-neighbor crystallites start

to become unstable, where desorption/adsorption occurs so frequently that the crystal outline become fluid and thermally roughened. Therefore, the rough-flat-rough transition is due to different thermal stabilities of *i*-neighbor crystallites, and the diffusion dominates when the desorption rate becomes zero. Finally, it should be noted that concentration also influences habits by adjusting adsorption rates. At very high concentrations, the incoming free chains are so numerous that the edge crystallites will have less chance to desorb or rearrange themselves into a more faceted habit before being buried by other incoming chains. This burying effect at high concentrations explains why the dendritic structure is often observed at high concentrations, and why the roughness of crystal outline increases with concentration.

3.3.6 Mechanism of Nucleation

Two nuclei with different sizes $R=3$, 5 are compared to illustrate the mechanism of nucleation, as shown in Figure 3.8. Here the 4-neighbor crystallites are almost impossible to desorb so that we will focus only on desorption of edge crystallites. The average binding energy $\langle E \rangle$ for the edge crystallites of size R is

$$\langle E \rangle = \frac{(4R-8)\times 3 + 4\times 2}{(4R-8)+4} = 3 - \frac{1}{R-1} \tag{3.7}$$

where $(4R-8)$ is the number of 3-neighbor edge crystallites, and 4 is the number of 2-neighbor corner crystallites. So the average binding energies for $R=3$ and 5 are $\langle E \rangle = 2.5$ and 2.75, respectively. This means that the edge crystallites of $R=5$ have stronger binding energy than those of $R=3$ so that the former is much stabler than the latter. As the nucleus size increases, it is deduced from Equation (3.7) that $\langle E \rangle$ will

become saturated and approach the limiting value 3. In other words, increasing the nucleus size from $R_0 = 1$ to 3 will make more difference than increasing the nucleus size from 3 to 5, as supported by the simulation results in Figure 3.5a. For each adsorption/desorption site, the probability of adsorption should be independent of R but dependent on the solute concentration, while the probability of desorption strongly depends on R through the dependence of E on R in Equation (3.7) (As R is smaller, the binding energy E becomes weaker, and therefore the desorption probability $P = \exp\left(\frac{-\Delta E}{kT}\right)$ increases significantly). In our view, the competition between the R-independent adsorption probability and the R-dependent desorption probability constitutes the mechanism of nucleation.

3.4 Conclusions

We have introduced a simple anisotropic aggregation model for polymer crystallization from solutions at concentrations below the overlap concentration. Starting from a seed of square shape of linear dimension R_0, we follow the aggregation of prefolded chains to form lamella by using a 5-state Potts model.

The present model is distinct from the previous LH and SG models in several aspects. First, the smallest dynamic unit is a whole chain in our model, instead of a stem in the LH theory or a segment in the SG model. Second, the nonlinear dependence of G on T is not caused by the exponential increase of L with T, but by the exponential dependence of desorption rates on T. In contrast, the LH theory and SG model assume that G is strongly correlated with L, with assumptions of an enthalpy barrier when

$L > L^*$ (the LH theory) or an entropic barrier from pinning effects when $L < L^*$ (the SG model). Third, reversible crystallization and melting is allowed in the present model, which is similar to the SG model but different from the LH theory. Fourth, our model puts polymer crystallization from dilute solutions into the same general framework of classical crystallization of small molecules. The only distinction between crystallization of polymers and small molecules is the anisotropic interactions introduced here, which confines polymers crystallization into a 2D lamella and slows down both crystallization and melting rates.

The crystallization behavior exhibited by our model is remarkably analogous to the experimental facts. Such a correlation is surprising, given the simplicity of the model. We now list the major correlations between the results of the anisotropic aggregation model and phenomenology of polymer crystallization from dilute solutions. In terms of crystal habits, both kinetic roughening in the LH theory and thermal roughening in the SG model can be reconciled by our model with producing the rough-flat-rough transition by merely varying temperature. Two more typical habits, the sharpened-apex lozenge and the dendritic structure, are also observed in our simulations. And it is further confirmed that the roughness increases with polymer concentrations. The mechanism of the rough-flat-rough habit transition is explained by different thermal stabilities of *i*-neighbor crystallites (which have different local binding energies). Consistent with experiments, time evolution of the lamellar size shows three or two distinct regions: nucleation, linear growth, and equilibrium regions. In terms of the temperature dependence of the growth rate, our simulations reproduce the exponential dependence of G on T. In terms of the concentration dependence of G,

our simulations successfully agree with the experimental fact that the growth exponent α increases with increasing T or decreasing C. In fact, closer inspection shows that α is not a constant. The mechanism of 2D nucleation (in contrast to the 1D stem nucleation in the LH theory) is explained by the competition between R-independent adsorption rates and R-dependent desorption rates. The effects of R_0, T and C on induction time τ and critical nucleus sizes are all consistent with experiments. Based on induction time, for the first time, a phase diagram of critical nucleus sizes on the $T-C$ plane is constructed depicting the various regions of different nucleation barriers.

It must be noted, however, that our model assumes a predetermined equilibrium thickness, instead of a kinetically trapped L as in the LH and the SG models. While this assumption is gathering acceptance due to data from isochronous experiments[22,23] and free energy calculations by single-chain simulations[13,21], it is desired to verify it by multiple-chain simulations and figure out the underlying mechanism for the finite thickness.

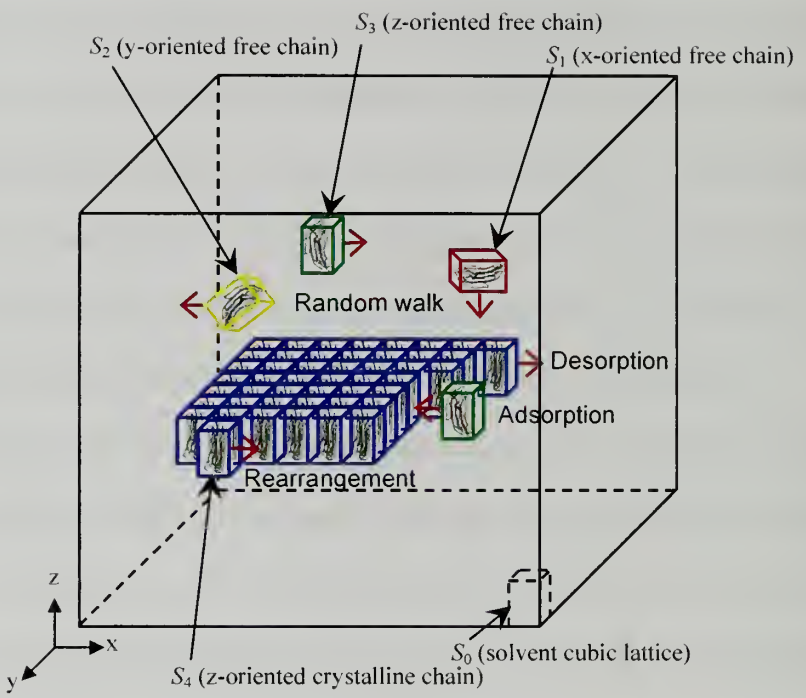

Figure 3.1: polymer solutions for single crystal growth are mapped onto a 3D array of lattice sites. Each lattice site takes one of five possible states. S_4 serves as the nucleus for subsequent crystal growth. $S_{1\sim3}$ and S_4 are interconvertible by adsorption and desorption. Interactions between $S_{1\sim3}$ are disabled in order to form a "single" crystal. For clarity, the solvent site S_0 is invisible herein except one example shown in the bottom-right corner.

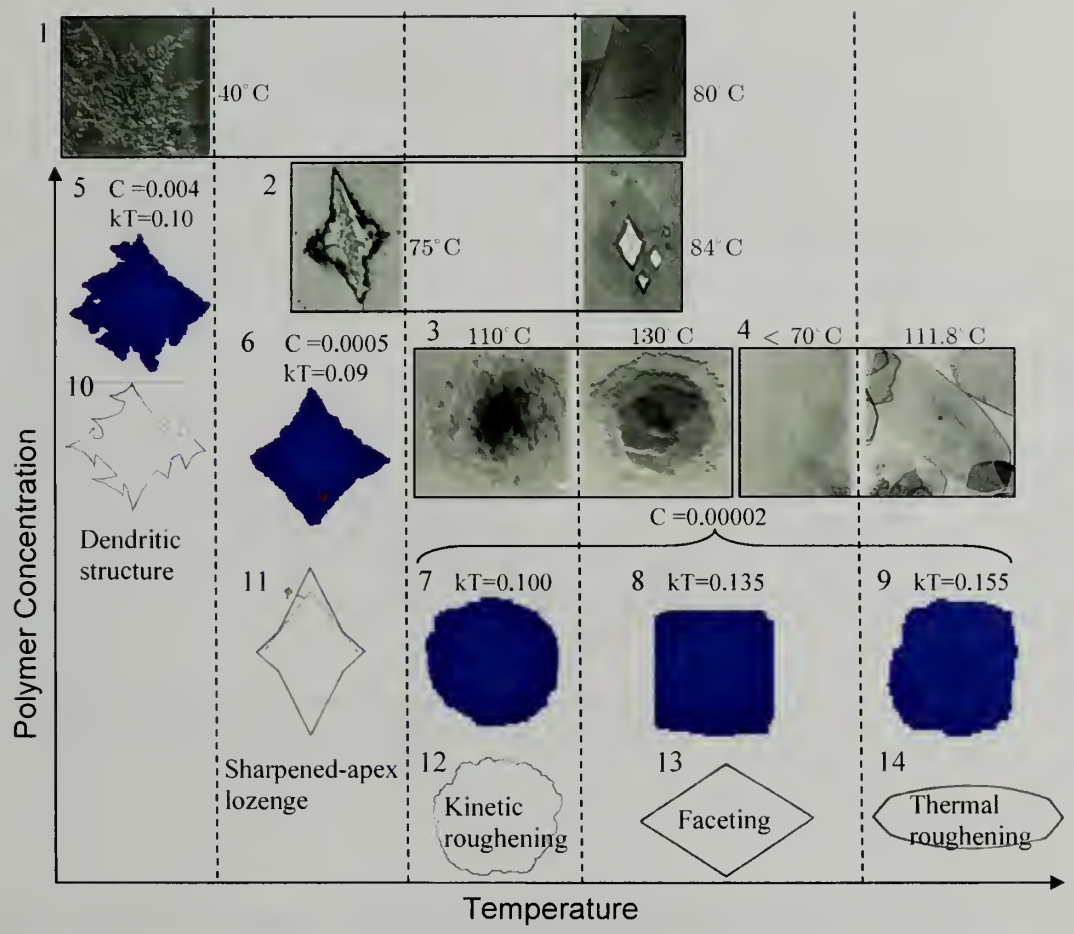

Figure 3.2: Five typical habits for solution-grown polymer crystals. The upper part (1-4) shows experimental observations: (1) 0.01% polyethylene in xylene solution.[50] (2) 0.1% polyethylene in o-xylene solution.[48] (3) 0.1% isotactic polystyrene in dimethyl phthalate solution.[53] (4) 0.05% polyethylene solution.[40] The middle part (5-9) presents our typical simulation results at various temperatures and concentrations. Note that a rough-flat-rough transition of habits occurs by merely adjusting temperature at $C = 0.00002$. The lower part (10-14) gives sketches of habits.

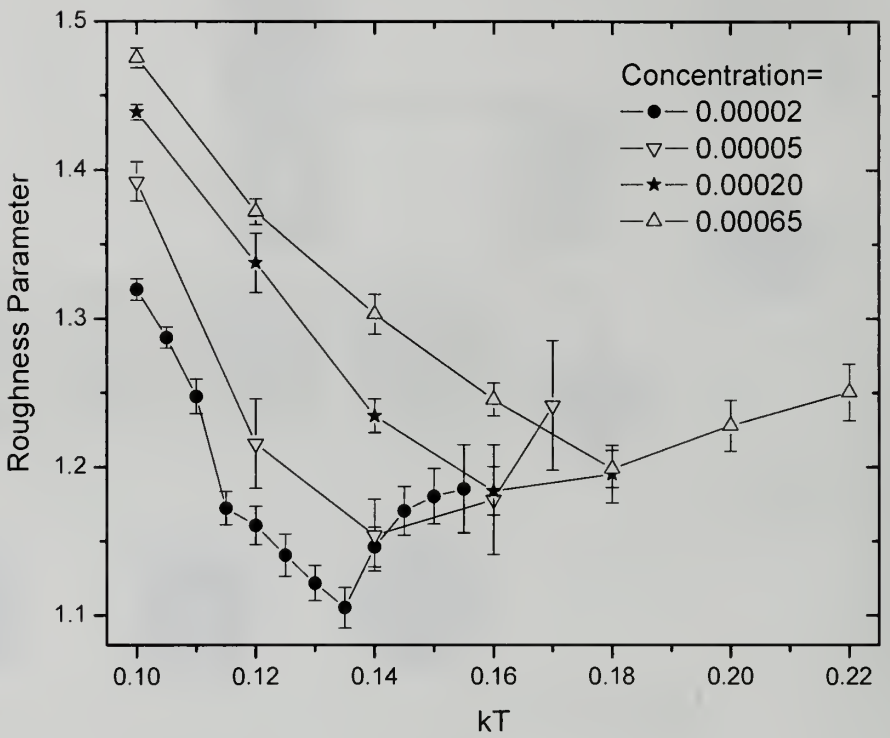

Figure 3.3: Roughness parameter (RP) as functions of temperature and concentration.

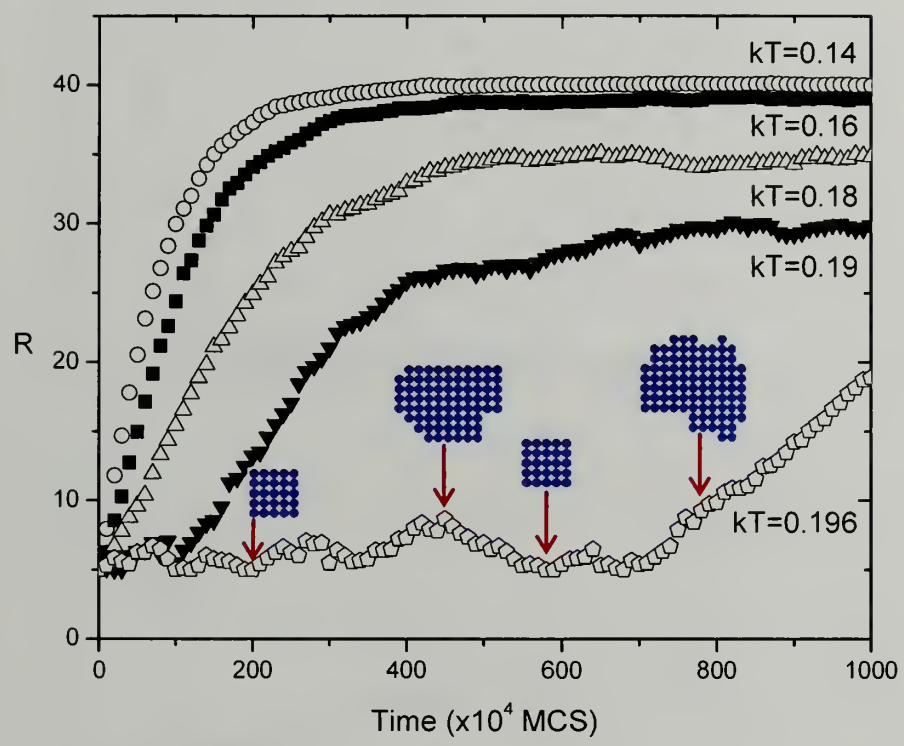

Figure 3.4: Time evolution of the lamellar size at various temperatures with a fixed $C = 0.0002$. The initial nucleus size is $R_0 = 5$. The simulation box size is $L_{box} = 200$. The four micrographs illustrate how the nucleus grows and redissolves with time until a fluctuation in size is large enough to overcome the nucleation barrier, where the number of crystalline chains in the crystal is equal to 25, 75, 25, 90 for t =207, 448, 571, 784 ($\times 10^4$MCS), respectively.

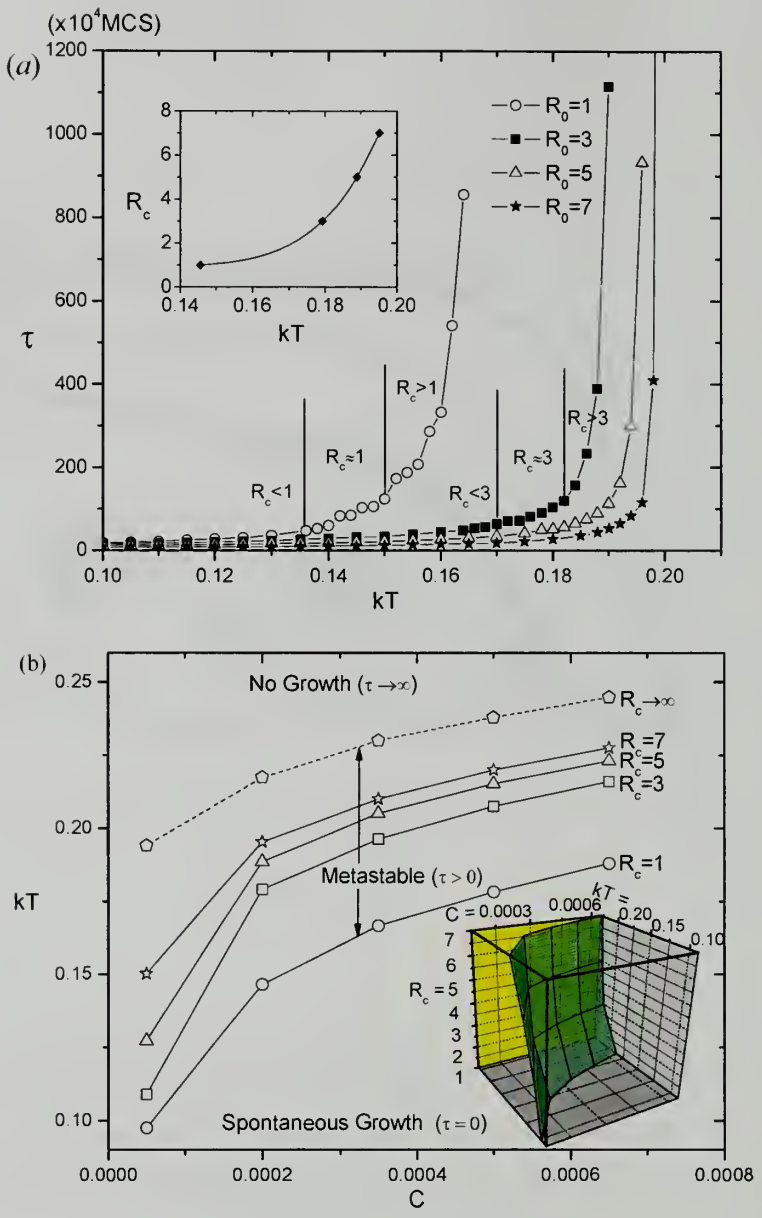

Figure 3.5: (a) Induction time τ as a function of temperature kT for various seed sizes R_0. $C = 0.0002$. The inset presents the critical nucleus size R_c as a function of temperature, which is obtained by intersects of a horizontal line $\tau = 100 \times 10^4$MCS with four curves at positions $kT = 0.146, 0.179, 0.189, 0.196$ for $R_0 = 1, 3, 5, 7$, respectively. (b) R_c is plotted as functions of both kT and C, resulting in a phase diagram with three regions.

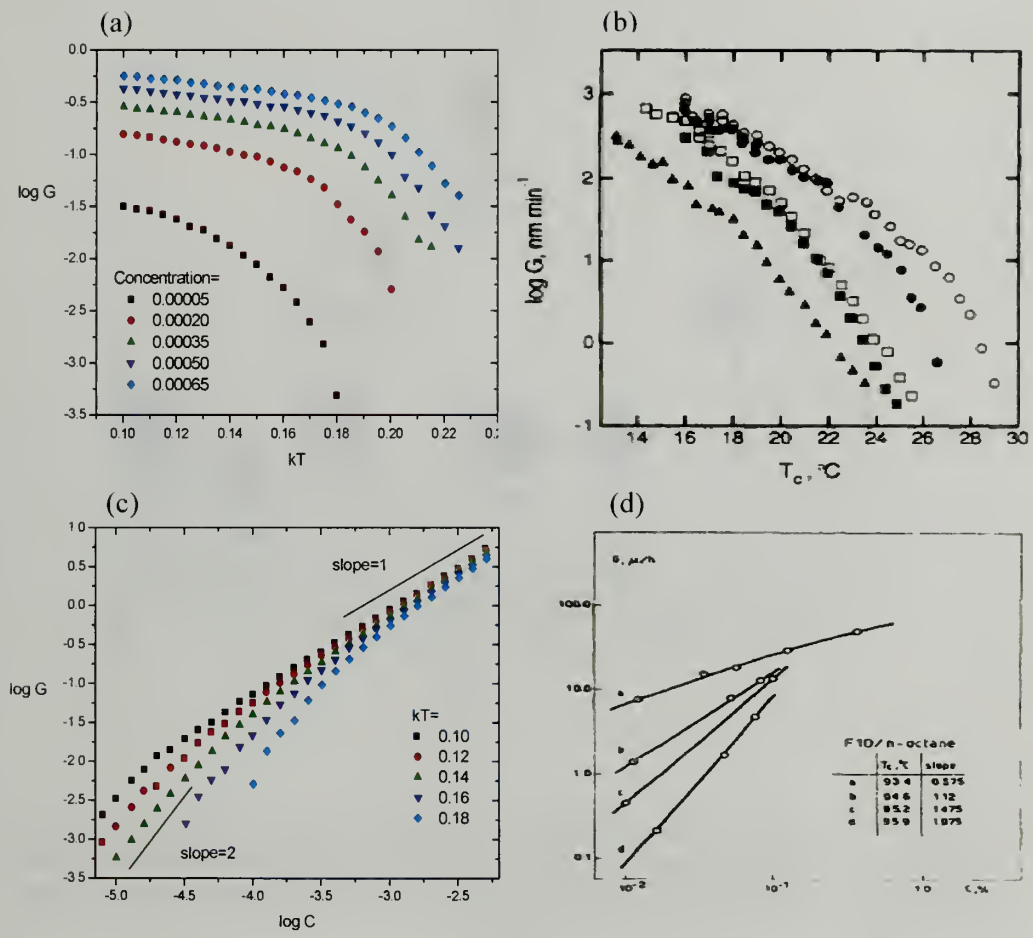

Figure 3.6: (a) Temperature dependence of the lamellar growth rate G at various concentrations. (b) Logarithmic of crystal growth rate against crystallization temperature for solution crystallization of Poly(ethylene oxide) of different molecular weights.[67] (c) Concentration dependence of the lamellar growth rate G at various temperatures. (d) Logarithmic growth rate (μm/hr) versus concentration of crystals for polyethylene sample grown from octane at different temperatures.[62]

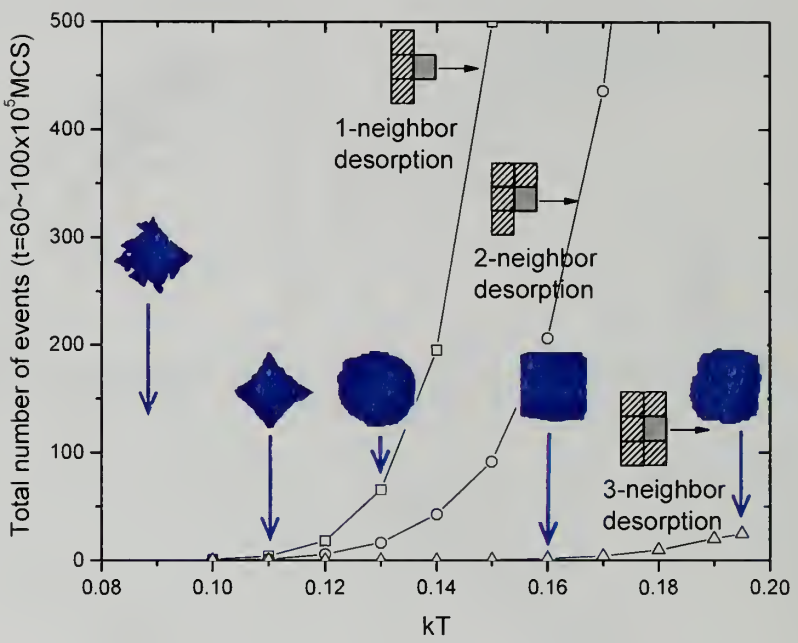

Figure 3.7: The total number of i-neighbor desorption events occurred during the late stage of crystallization at various temperatures. 1-, 2-, 3-neighbor crystallites become unstable at $kT = 0.10, 0.12, 0.16$ respectively, resulting in different crystal habits. $C = 0.0002$.

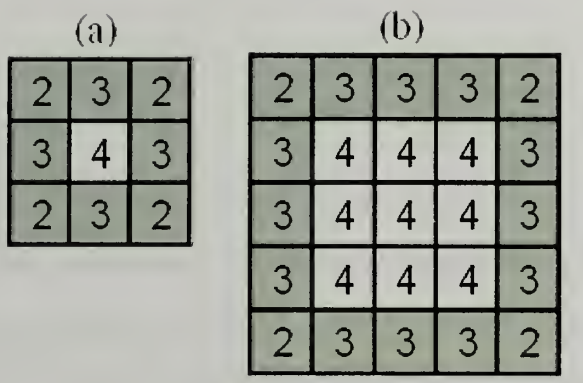

Figure 3.8: Mechanism of nucleation and stability of edge crystallites. (a) 3×3 nucleus; (b) 5×5 nucleus. The number in each square designates how many neighboring crystallites it has.

CHAPTER 4

SHISH-KEBAB CRYSTAL

4.1 Introduction

Flow-induced polymer crystallization is of considerable technical importance because it occurs practically in all industrial molding and extruding processes. The typical morphology found in polymer solution or melt subjected to flow is so-called "shish-kebab"[68-71] or "row" structures.[72-74] It is widely believed that the "shish", an extended-chain type of backbone which serves as the nucleus for subsequent growth, formed first under flow from the relatively longer chains[75,76] (because the coil-stretch transition depends critically on the chain length). The "kebabs", a folded-chain type of lamellae, formed next from the relatively shorter chains by secondary nucleation and epitaxial growth onto the shish.[77,78]

Although shish-kebab crystals have been studied for forty years, the mechanism of kebab formation is still a matter of controversy. Pennings et al.[68,69] proposed that the kebabs are formed by "hairdressing" the cilia which are partially incorporated in shish threads by velocity gradient. The cilia model was further modified by the distinction between macro- and micro-"shish kebabs" introduced by Barham and Keller.[79] The macro-kebabs are removable, while micro-kebabs are permanent, indicating intimate molecular connectedness with an essentially extended chain core. The TEM micrographs by Liu et al.[80,81] also suggested that micro- and macro-kebabs are reversible via melting and recrystallization, due to the differences in their thermal

stability. Nagasawa and Shimomura[82] proposed that the kebabs grow by a screw dislocation mechanism, and then are deformed by the shear stress to form the shish-kebab structure. It is also proposed that there exists periodic density modulation of shish defects, which pre-determines the kebab spacing.[33,83,84] TEM Dark Field micrograph showed many structure defects distributed randomly along both the shish cores and the overgrown kebabs.[80,81] It is possible that the dense regions along the precursor shish give rise to the periodic kebab lamellae.[75] Another model is related to the early observations of nodular structures by Geil et al.,[85,86] where strain-induced crystallization occurs by rotation, alignment and perfection of internal order of paracrystalline ball-like structures (7.5-10 nm in diameter) originally present in the amorphous material. In light of the above different models, one of the motivations in the present work is to test whether Geil's model (diffusion and alignment of prefolded bundles on the shish) is consistent with other experimental results such as kebab spacings and diameters. If so, this would be a strong support to Geil's nodular structure as well as our prefolding concept introduced in the forgoing chapters.

Another motivation is to figure out the real temperature dependence of kebab spacings. The isothermal crystallization by Pennings et al.[68] and Hill et al.[70,71,73] showed three interconvertible morphologies. At lower temperatures, "closely spaced shish kebabs" (type II) are formed over a wide temperature range. The kebab diameters and spacings keep constant with increasing temperature until some point they experience drastic augmentation over a narrow temperature range, which corresponds to "widely spaced shish kebabs" (type III). Beyond these two regions, at very low temperature or very high temperature, only "smooth shish threads" (type I) are formed. These three

types of morphologies are interconvertible by dissolving the kebabs at higher temperature and recrystallization under different conditions. The type of morphology obtained solely depends on the final storage temperature, showing history-free characteristics. Pennings et al. were interested in the narrow temperature range where large spacings (type III) occurred and proposed a model based on the nucleation theory:[68]

$$\ln S \sim \frac{1}{T\Delta T} \tag{4.1}$$

where S is the average kebab spacing, T is isothermal crystallization temperature, and the supercooling $\Delta T = T_m^{\,0} - T$. Later on, Hill et al. repeated Pennings' experiments and proposed a new model after further considering depletion of materials:[70,71]

$$\ln S \sim \frac{1}{T\Delta T^2} \tag{4.2}$$

Nevertheless, by plotting the same data according to the two different models, Hill et al. can not tell which model is more correct as the temperature range studied is too narrow. The data plotted against Equation (4.1) and Equation (4.2) both show good linearity. The present study aims to find out which model is better.

Another important feature which should be taken into account is that the kebab spacing is not fixed but evolves with time. Preliminary work by Hill et al.[70] showed that closely-spaced kebabs transformed into widely-spaced kebabs when the storage time prolonged from 2 to 48 hours. When transferring the sample from hot xylene to cool xylene for quenching purpose, if the transfer lasted longer, fibers which they expected to be smooth started to show overgrowths. Subsequent studies by Hill et al.[71] revealed that the average spacing increase linearly with washing time at the first stage and then

reach an equilibrium value. Moreover, the initial slope of spacing versus time (i.e., the spacing growth rate G_S) increased with increasing the washing temperature. For nonisothermal experiments, TEM observations by Petermann and Gleiter[74] in the film of polystyrene melts indicated that the kebab diameters decreased with increasing quenching rate (less crystallization time). At the highest quenching rate, long rod-shaped crystals (shish) were observed. The three types of morphologies aforementioned are reversible depending on the quenching rate too. The present simulation aims to monitor how the kebab spacing and diameter evolve with time.

In line with the prefolding concept, we propose a new model for shish-kebab crystallization. Under shear stress, due to the coil-stretch transition, longer chains are extended to form shishs while shorter chains remain coiled and gradually prefold into bundles. The shish provides nucleation sites onto which the prefolded bundles adsorb to form kebabs. The kebab spacing varies with time because these prefolded bundles can desorb from the shish or the growth front reversibly.

4.2 Model and Simulation Algorithm

The model is very similar to the model employed in the single crystal study in the previous chapter. The only distinction is to extend a 1×1 seed in the single crystal study along z direction to form a $1\times1\times100$ shish. The effect of the shish diameter is not investigated for the time being. All simulations are performed in a cubic box with length $100\times100\times100$ under periodic boundary conditions, which is discretized into 10^6 cubic lattices with length $1\times1\times1$. Each cubic lattice is assigned to a state from five possible states, as shown in Figure 4.1: empty/solvent cubic lattice (invisible here), x-,

y-, z-oriented free chain (prefolded bundle), and z-oriented crystalline chain (shish or kebab crystallite). The only difference between shish and kebab chains is that the shish chain is fixed immobile while the kebab chain are indexed dynamic units, interconvertible with free chains. Similar to the single crystal study, there are four types of random walks: diffusion, adsorption, desorption, and rearrangement along the growth front. The other details such as energy settings and procedures can be consulted with the previous chapter.

4.3 Results and Discussion

4.3.1 Morphology

As mentioned in the Introduction, the kebab diameter and spacing increase with time.[70,71] Such time dependences are indeed observed in our simulations. As seen in Figure 4.2, in all cases, nucleation and growth of kebabs take place very quickly ($< 10^5$ MCS) at the beginning. The initial kebab diameters and spacings are relatively small. Then, kebab diameters and spacings increase gradually over a long period of time by the Oswald ripening mechanism (or Evaporation-condensation mechanism). Detailed analysis on morphological evolution reveals that bigger kebabs grow at the expense of smaller ones and only the biggest kebab survives if enough time is allowed, which is a typical characteristic of the Ostwald ripening process. In experiments,[71] the time required to crystallize the overgrowth is about one minute, while the time required to achieve larger spacings is about two days. AFM in-situ study of polyethylene shish-kebabs[87,88] revealed that the growth rate of individual lamella varies from time to time

and differs from lamella to lamella, consistent with our simulations and the Ostwald ripening mechanism.

By comparing Figure 4.2a and b, it is clearly seen that the kebab spacing and diameter increase with increasing temperature.[71] By comparing Figure 4.2b and c, it is evident that the kebab spacing decreases whereas the kebab diameter increases with increasing polymer concentrations. Row structures grown in the melt is a somewhat inappropriate example for concentration effects. The primary difference between solution-grown shish kebabs and melt-grown row structures is that row structures usually have considerably wide kebabs and narrow spacings[87]. So the row structure can be regarded as the extreme case of the shish-kebab structure where polymer concentration is very high.

Another important characteristic of morphologies is that the spacings and diameters of kebabs are not uniform but show irregular distributions. The existence of distribution is consistent with many experiments and reflects the random nucleation nature of kebeb formation. The model ideally allows for random nucleation and growth anywhere on the shish backbone or on the existing kebab growth front. Close inspection on kebabs reveals that the shish is not necessarily located at the center of kebabs. Some kebabs appear to stick out with a preferred growth direction, as also noted in the TEM studies.[80,81]

4.3.2 Kebab Spacing Distribution

Direct observation of shish kebabs by AFM[88] and TEM[80,81] showed that the lamellae are not equally but irregularly spaced along the shish backbone. The more

quantitative studies by Pennings et al.[68,69] revealed that the spacing distribution is actually a lognormal distribution or a positive skewed distribution, which is indicative of a random nucleation process. It is noteworthy that frequency distribution of long periods for the row structure in the melt also showed a skewed distribution[89]. The spacing distribution counted in our simulations is displayed in Figure 4.3a, in good agreement with the experimental data shown in Figure 4.3b.[69] As time elapses, the skewed spacing distribution becomes broader and broader.

4.3.3 Time Evolution of Kebab Spacings

As mentioned in the Introduction, the kebab spacing is strongly dependent on time or quenching rate. In Hill's experiments (Figure 4.4b),[71] the spacing increases linearly with washing time and then reaches an equilibrium value. Moreover, higher washing temperature results in a higher spacing growth rate at the beginning. This is in good agreement with our simulation results shown in Figure 4.4a, where each curve can be roughly divided into two stages. The initial linear stage corresponds to the Ostwald ripening process. The final equilibrium stage of value 100 corresponds to the case where only one biggest kebab survives in the simulation box. Similar to Hill's experiments, the initial slope (the spacing growth rate G_S) increases with increasing temperature.

4.3.4 Temperature vs. Spacings

Temperature dependence of the average kebab spacing at different times is presented in Figure 4.5a. At the early stage $t = 1\times10^5$ MCS, the spacing is essentially

constant over a wide temperature range. At late stage $t = 1000 \times 10^5$ MCS, however, the spacing is constant in a narrow low-T region and increases significantly with T in a high-T region. Surprisingly, similar time dependence of temperature effects on spacings was observed in isothermal crystallization of shish-kebabs in polyethylene solution, as shown in Figure 4.5b.[71] It is evident that the spacing for the sample held for only one minute is constant (210±12nm) over $T = 91.5 \sim 96\,^{\circ}\mathrm{C}$, whereas the spacing for the sample held for two days increases significantly from 200nm to 691nm. The invarant spacing in the low-T region can be explained by the slow Ostwald ripening process at low temperatures. The desorption probability of crystallites, $P = \exp(-\Delta E / kT)$, is almost zero for low kT so that the kebabs appear frozen without any change in spacings (see Figure 4.2a).

Using the same data in Figure 4.5a, three different models regarding the temperature dependence of kebab spacings are given in Figure 4.6a (Pennings' model), b (Hill's model), and c (our model), respectively. Apparently, Pennings' and Hill's models did not take time effects into account. As time elapses, the slopes of two models increase continuously. Even for a fixed time, both models do not exhibit good linearity over the entire temperature range. The lines become curved at both ends. Different $T_m^{\,0}$ values have been tried. But the problems of time-dependent slopes and nonlinearity still remain. On the other hand, if we plot the logarithm of the spacing growth rate $G_S = \dfrac{S - S_0}{time}$ (i.e., the initial slopes in Figure 4.4a) as a function of $1/T$, a good linearity and time invariant are both observed, as illustrated in Figure 4.6c and the following equation:

$$\ln G_S \sim 1/T \tag{4.3}$$

4.3.5 Concentration vs. Spacings

As shown in Figure 4.7a, the average spacing grows linearly with time. The spacing growth rate (which are obtained from the slopes in Figure 4.7a) is found to be proportional to the inverse of polymer concentration (Figure 4.7b):

$$G_S \sim 1/C \tag{4.4}$$

leading naturally to the relation $S \sim 1/C$, which is to be tested by experiments.

4.3.6 Kebab Diameter Distribution

In contrast to the spacing distribution, the kebab diameter distribution is symmetric, as shown in Figure 4.8a. As time elapses, the diameter distribution becomes broader and broader. Interestingly, if the diameter distributions in Figure 4.8a are normalized by the average diameter in X axis and the total number of counts in Y axis, all the curves will overlap onto one another (Figure 4.8b), indicating self similarity inherent in the kebab growth.

4.3.7 Time Evolution of Kebab Diameters

Figure 4.9a displays time evolution of the average kebab diameter at different temperatures. The log-log plot reveals the scaling law $R \sim t^{0.38}$ in the late stage. It has been established that Ostwald ripening follows the scaling law $R \sim t^{1/3}$ in the late stage.[44,45] The exponent 0.38 obtained here is close to 1/3 scaling law, in good agreement with the Ostwald ripening mechanism. If shifting each curve in Figure 4.9a

horizontally by a proper distance $\log a_T$, all curves can overlap and form a master curve. This is actually a well known phenomenon called "time-temperature superposition" in the polymer field, which means that increasing temperature has similar effects as prolonging time.

4.4 Conclusions

A new model based on the prefolding concept is proposed to study the shish-kebab polymer crystallization. It is surprising that such a simple model can reproduce so many experimental findings.

Both spacings and diameters become larger with time. The growth rate of individual kebab varies with time and from lamella to lamella. The shish is not necessarily located at the center of kebabs. The distribution of kebab spacings is found to be lognormal, consistent with experiments. The kebab spacing increases linearly with time and then reaches equilibrium later. For a short period of time, the spacing remains constant over a wide temperature range. For a long period of time, the spacing is constant in the low-T region but increases exponentially in the high-T region. Both behaviors are confirmed by experiments. In contrast to Pennings' and Hill's models, we propose a new model to describe the relation between spacings and temperature, $\ln G_S \sim 1/T$, where $G_S = \frac{S - S_0}{time}$ is the spacing growth rate and S_0 is the initial spacing or the low-T spacing. We also propose that the relation between spacings and concentration follows $G_S \sim 1/C$ and $S \sim 1/C$, which is to be tested by future experiments.

On the other hand, the distribution of kebab diameters is found to be symmetric, which needs to be tested in experiments. If the diameter distributions are normalized, they will overlap on one another, indicating self-similarity in kebab growth. The kebab diameter follows the scaling law $R \sim t^{0.38}$, which is close to the 1/3 law commonly observed in the Ostwald ripening process. We propose that Ostwald ripening is the dominating mechanism for polymer shish-kebab crystallization.

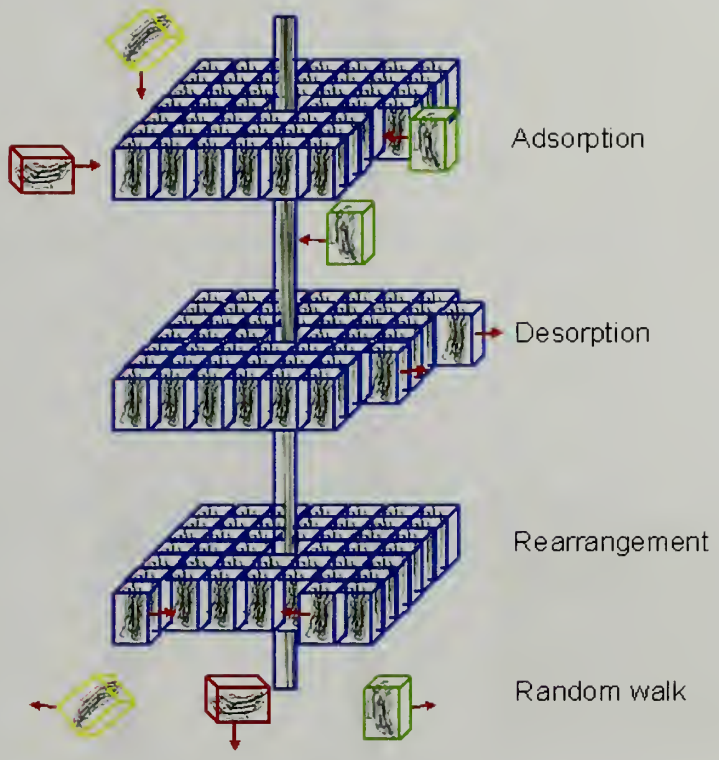

Figure 4.1: Polymer solution for shish-kebab crystallization is mapped onto a three-dimensional array of lattice sites with length $100 \times 100 \times 100$. Each lattice takes one of five possible states: x-, y-, z-oriented free chains, z-oriented crystalline chain (shish or kebab crystallite), and empty lattice site (invisible here).

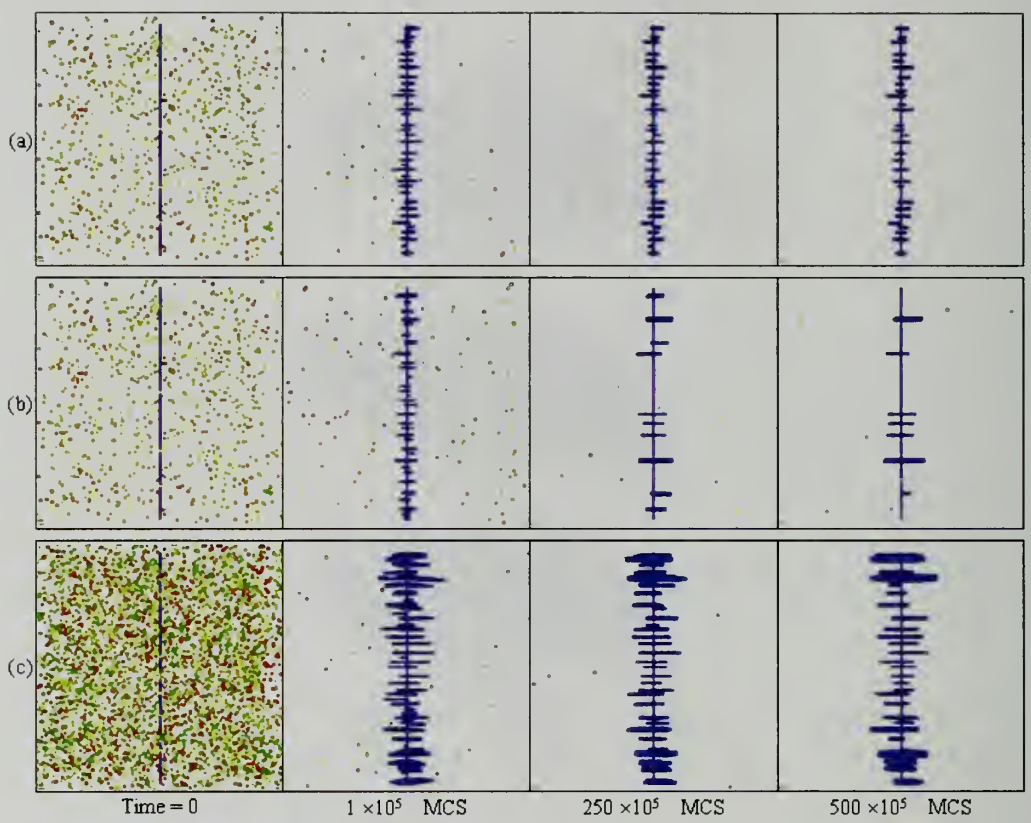

Figure 4.2: Time evolution of kebab formation. (a) kT=0.12, C=0.001; (b) kT=0.15 (higher temperature results in larger spacings and bigger kebabs), C=0.001; (c) kT=0.15, C=0.005 (higher concentration results in narrower spacings and bigger kebabs).

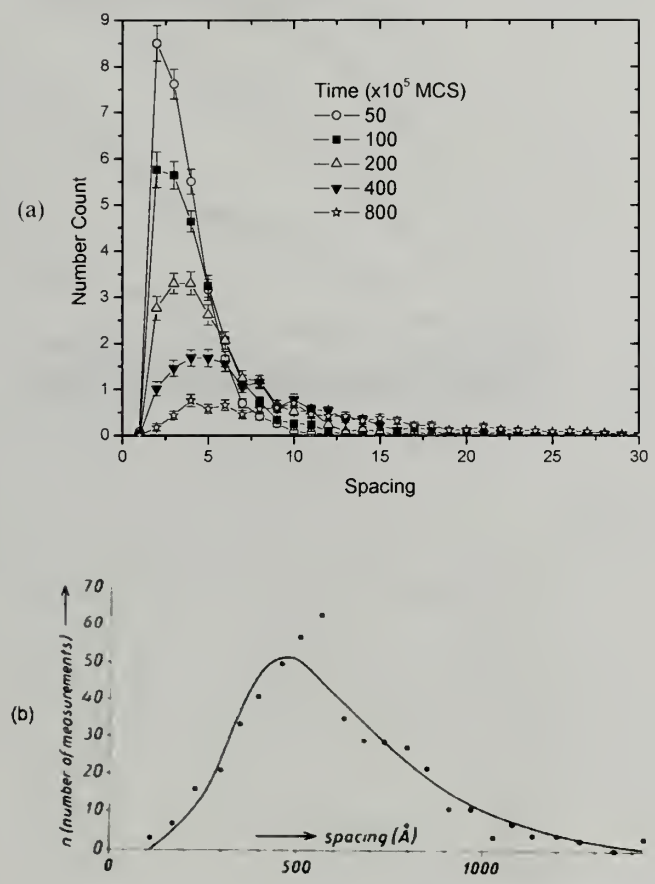

Figure 4.3: (a) Time evolution of skewed distribution of kebab spacings. All the curves are under conditions kT=0.14 and C=0.001. (b) Lognormal distribution of kebab spacings by Pennings et al.[68,69]

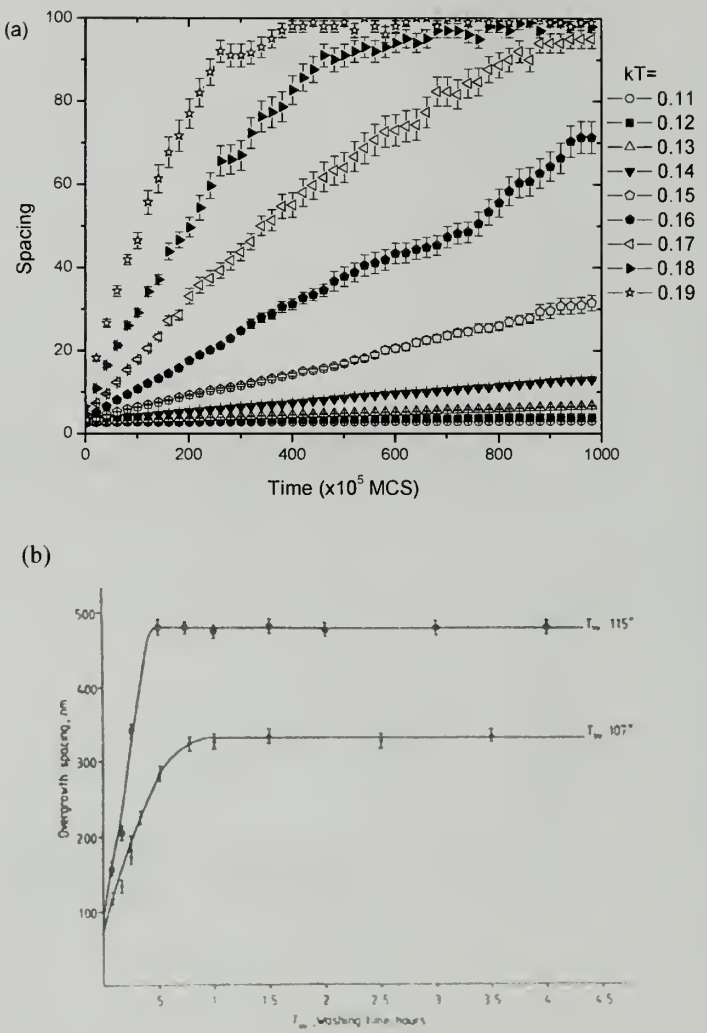

Figure 4.4: (a) Time evolution of the kebab spacing at different temperatures in our simulations. (b) Time evolution of the kebab spacing at different washing temperatures in experiments.[71]

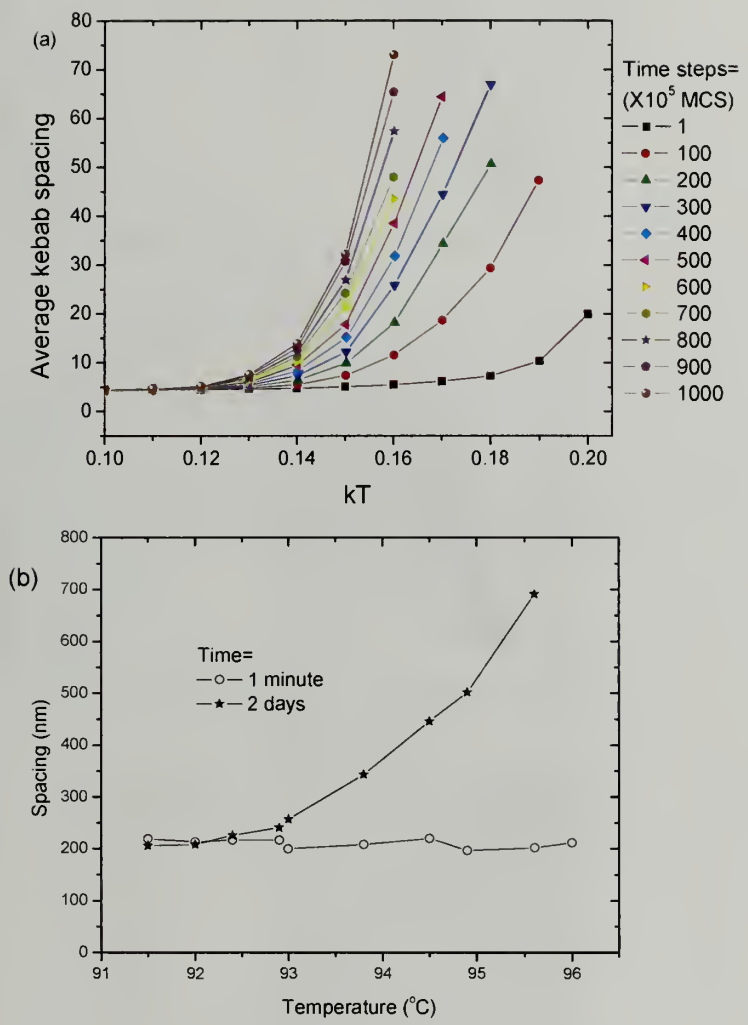

Figure 4.5: Time evolution of temperature dependence of the kebab spacing. (a) Simulation results at C=0.001. (b) Experimental results extracted from Table 2 in Ref. [71].

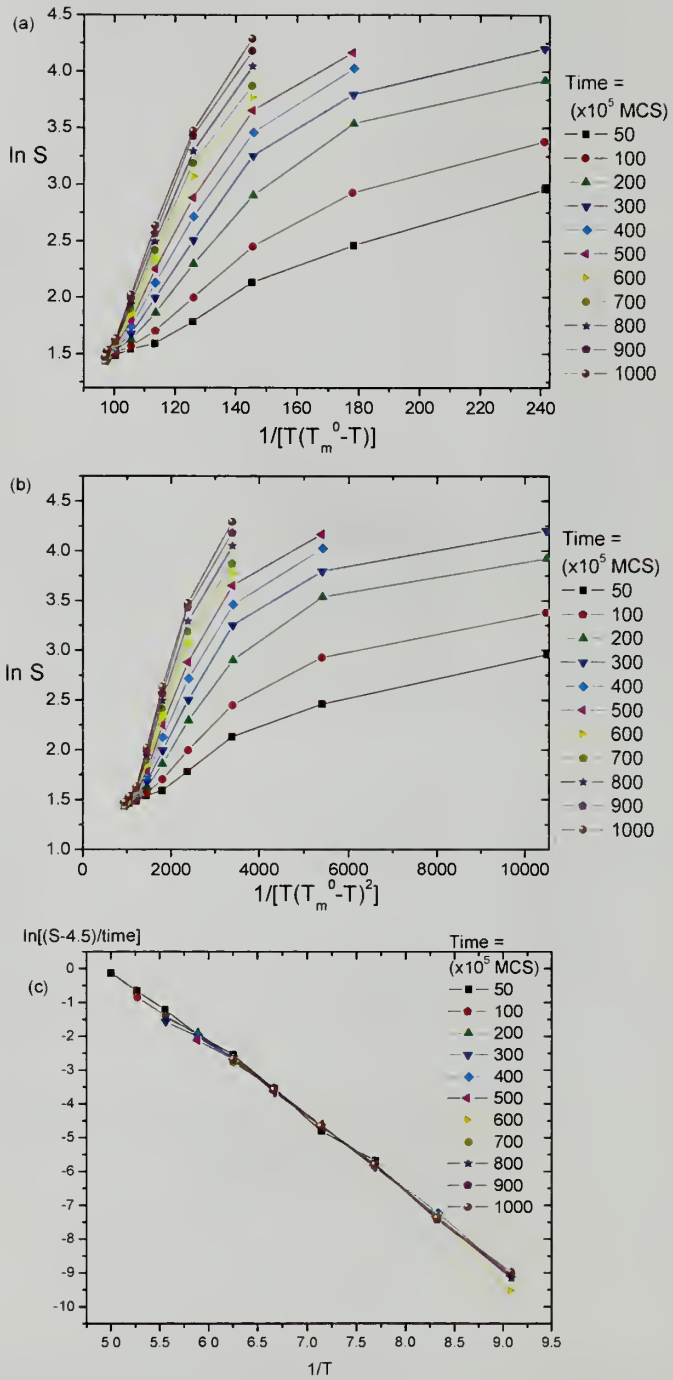

Figure 4.6: (a) Pennings' model: $\ln S \sim 1/T\Delta T$. (b) Hill's model: $\ln S \sim 1/T\Delta T^2$. (c) Our model: $\ln G_S \sim 1/T$, where $G_S = (S - S_0)/time$ is the spacing growth rate, S_0 is the initial spacing in Figure 4.4a, or the constant minimum spacing in the low-T region in Figure 4.5a.

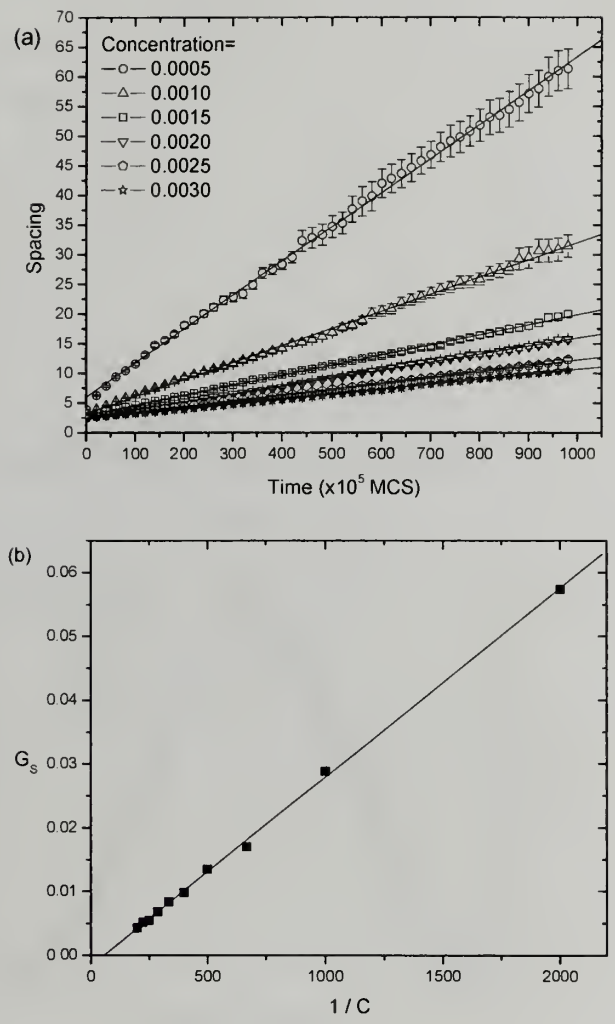

Figure 4.7: (a) Time evolution of the average kebab spacing at different concentrations. kT=0.15. (b) The spacing growth rate, the slope in (a), is proportional to the inverse of polymer concentration, i.e., $G_S \sim 1/C$.

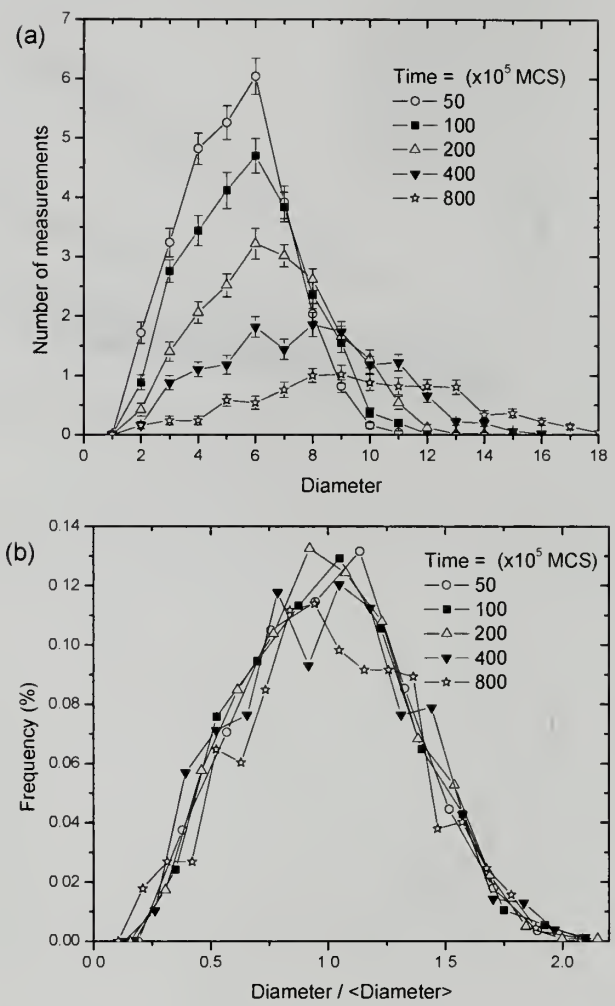

Figure 4.8: (a) Time evolution of symmetric distribution of kebab diameters. kT=0.14 and C=0.001. (b) The diameter distribution in (a) normalized by the average diameter in X axis and the total number of measurements in Y axis becomes invariant with time.

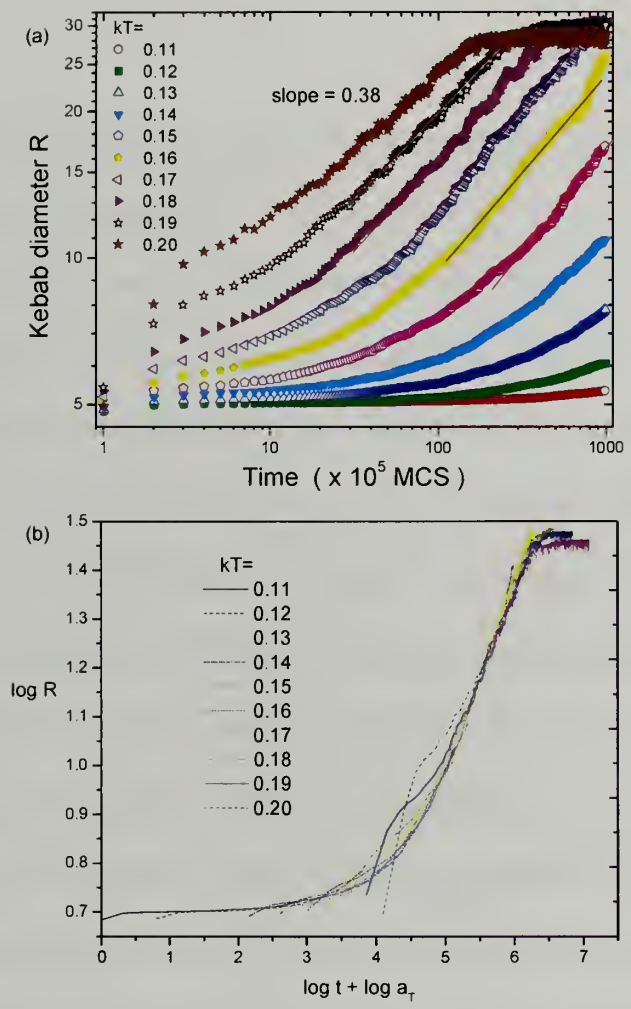

Figure 4.9: (a) Time evolution of the average kebab diameter at different temperatures. (b) The curves in (a) are horizontally shifted into a master curve.

CHAPTER 5

CRYSTAL MELTING

5.1 Introduction

The melting behavior of polymer crystals is quite different from that of small molecule crystals. For small molecule crystals, the melting transition is very sharp. The melting point T_m is well-defined and independent on many factors. In contrast, for polymer crystals, the melting transition is very broad, making definition of the melting point difficult. Even if the last trace of the melting transition is defined as the melting point T_m for polymer crystals, T_m is observed to vary considerably depending on many factors, such as crystallization temperature T_c, crystallization time t_c, and heating rate β, polymer concentration, the degree of crystallinity, the lamellar thickness L, and so on. The large variation in T_m of polymer crystals makes the quantitative study on theories of polymer crystallization very difficult. In light of this, people defined an ideal temperature as the reference temperature, which is independent on the above factors. This ideal temperature, namely the equilibrium melting temperature T_m^0, is defined as the melting point of lamellae of infinite thickness and infinite large lateral dimensions so that all surface effects are negligible. T_m^0 is so critical for polymer crystallization research because the supercooling depth is defined by $\Delta T = T_m^0 - T_c$, which is believed to be the driving force for polymer crystallization and included into most crystallization theories. Due to the infinite size, T_m^0 actually serves as the upper limit for all observed T_m for any polymer (e.g. polyethylene). The depression of T_m from T_m^0 was explained

by the fact that real polymer crystals can never be as perfect as the ideal crystals with infinite size and 100% perfection. The extent of depression of T_m is strongly dependent on the aforementioned factors. The quantitative dependence of T_m on the factors and the ways to extrapolate T_m^0 is to be described briefly in the following paragraphs.

Polymer crystals tend to melt out well below T_m^0 because of a restriction of one crystal dimension, lamellar thickness L, to a small size. Normally the thicker the lamella is, the higher T_m is. The dependence of T_m on L was described by Gibbs-Thomson (GT) equation:[90]

$$T_m = T_m^0\left(1-\frac{2\sigma_f}{L\Delta h}\right) \tag{5.1}$$

where σ_f is the fold surface free energy and Δh is the heat of fusion per volume. Therefore a plot of T_m versus $1/L$ can be extrapolated to the intercept T_m^0.

Another way to extrapolate T_m^0 is Hoffman-Weeks (HW) plot[91,92], before which two more equations have to be introduced first. At the very beginning of nucleation, a virgin lamella (i.e. primary nucleus) is formed and possesses a small and temperature-dependent thickness L^*:

$$L^* = \frac{2\sigma_f T_m^0}{\Delta h \Delta T} + \delta L \tag{5.2}$$

Where δL is small and omitted in the HW equation. The virgin thickness L^* is chosen because a crystal of this thickness has the maximum rate of growth in lateral directions, but not because a crystal with this thickness is the most stable at the crystallization

temperature.[91,92] So lamellae tend to increase its stability by thickening from L^* to L. Normally a thickening coefficient γ is defined as:

$$\gamma = \frac{L}{L^*} \tag{5.3}$$

Another assumption in the HW equation is that thickening is not serious and thickening coefficient γ is a constant close to unity. Combining Equations (5.1), (5.2), and (5.3) by omitting δL and assuming a constant γ, the HW equation is given by

$$T_m = \left(1 - \frac{1}{\gamma}\right) T_m^0 + \frac{1}{\gamma} T_c \tag{5.4}$$

Therefore a plot of T_m versus T_c is linear with slope $1/\gamma$ and the extrapolated intersection with the $T_m = T_c$ line is taken to be T_m^0. Because the thickening coefficient $\gamma > 1$, the slope of T_m versus T_c should be in the range $0 < 1/\gamma < 1$. According to the HW equation, T_m should increase linearly with T_c, which is to be tested in our simulations.

Although the GT and HW plots were successful in fitting a straight line for experimental data in the narrow T_c range, nonlinear behaviors are more often observed over a wide T_c range. Alamo et al.[93] pointed out that the T_m versus T_c data can be divided into three regions: in the low-T_c region, T_m is constant with T_c; in the intermediate-T_c region, T_m increases linearly with T_c; in the high-T_c region, T_m deviates from a straight line and curves upward with increasing T_c, even parallel to the $T_m = T_c$ line. Such an exponential growth of T_m with T_c was declared as a general phenomenon observed over a wider temperature range for many polymers.

Although this upward curvature obviously raises a serious question on validity of the HW equation, people tried to explain this discrepancy by thickening and superheating effects. There are two types of thickening mechanisms.[91,92] One is melting out of thin crystals followed by recrystallization to form thicker ones (melting-recrystallization mechanism), which usually occurs at lower heating rate β and becomes more pronounced at lower T_c. Another type of thickening is chain sliding in the crystal, which is generally more pronounced at higher T_c. The superheating effect is a phenomenon that T_m increases with increasing the heating rate β,[94-96] normally following the relation[96-99]

$$T_m \sim \beta^{0.5} \tag{5.5}$$

The superheating effect is explained by the case when the heating rate is much faster than the melting rate of lamellae. On the other hand, when the heating rate is extremely slow $\beta \to 0$ (called "slow heating technique"), Roberts and Mandelkern[100] pointed out that T_m (defined by the temperature at which the last traces of crystallinity disappear) thus obtained is well-defined, reproducible, and independent of any previous thermal history of the sample. This temperature was actually identified as the true equilibrium melting temperature at that time (unfortunately, this concept was not accepted by the polymer community, probably due to the tediousness in performing slow heating experiments). Besides heating rate dependence, T_m was observed to depend on the initial crystallization time t_c as follows[27,101]

$$T_m \sim \log t_c \tag{5.6}$$

As Weeks pointed out,[102] the relation $T_m \sim \log t_c$ may be a result of lamellar thickening $L \sim \log t_c$. In order to make the GT and HW plots more accurate, people tend to exclude any possibility of thickening or superheating by choosing narrow T_c range, low degree of crystallinity, intermediate heating rate, and extrapolating $T_m(\beta, t_c)$ to $T_m(\beta = 0)$[98,103,104] and $T_m(t_c = \tau)$[27,101,105], where τ is the induction time corresponding to crystallinity equal to zero or heat of fusion equal to zero at early stage. Besides extrapolation methods, a nonlinear HW plot was proposed by Marand et al.[106] They revised the HW equation by taking the δL term into account, assuming γ is not constant, and using M-X fitting to extrapolate T_m^0 by ensuring no thickening $\gamma = 1$:

$$M = \gamma(X + a) \tag{5.7}$$

where $M = \frac{T_m^0}{T_m^0 - T_m}$, $X = \frac{T_m^0}{T_m^0 - T_c}$, and $a = \frac{\delta L \Delta h}{2\sigma_f}$ is a dimensionless constant.[27] Normally the nonlinear HW plot shows an upward curvature and extrapolates to a higher T_m^0 value than the linear HW plot does.

All the experimental results aforementioned, such as the exponential growth of T_m with T_c and $T_m \sim \log t_c$, were generally ascribed to the one-to-one correspondence between T_m and the lamellar thickness L. In the present work, we shall give an entirely different explanation for the observed T_m variations based on the one-to-one correspondence between T_m and the lamellar diameter R. In line with the prefolding concept and the concept of predetermined equilibrium thickness, our model with fixed

lamellar thickness but variable lamellar diameters can reproduce most experimental results including the exponential dependence of T_m on T_c, $T_m \sim \beta^{0.5}$, and $T_m \sim \log t_c$.

5.2 Model and Simulation Algorithm

The model is exactly the same as the model employed in the shish-kebab studies. After the shish-kebab crystallization has occurred at crystallization temperature T_c for certain crystallization time t_c, the whole system is heated stepwisely (e.g. increasing kT by 0.0001 every 10000 MCS) until the previously formed kebabs are all melted. The time/temperature point at which the last trace of kebab crystals disappears is denoted as the melting point T_m. The details about the model parameters and settings can be referred to the previous chapters.

5.3 Results and Discussion

5.3.1 Morphology

As shown in Figure 5.1a, the starting random configurations for prefolded chains in the simulation box is to mimic the athermal state above the melting temperature. When the simulation starts, the chains quickly nucleate onto the shish to form small kebabs, as depicted in Figure 5.1b. After continuing isothermal crystallization at temperature T_c for time t_c, the kebab diameters become larger, as shown in Figure 5.1c. It is noteworthy that how large the kebabs can grow depends on both T_c and t_c. Then the system is heated stepwisely. Because desorption probability increases significantly with kT, the kebab crystals start to melt gradually. Figure 5.1d

shows the last trace of kebab crystals. At this time point, the corresponding temperature is recorded as the melting point T_m.

5.3.2 Broad Melting Transition

It is observed that the degree of crystallinity (proportional to the total number of crystallites) increases quickly to reach an equilibrium value during the initial crystallization time t_c, and then decreases gradually upon heating, showing a broad melting transition. Figure 5.2 shows typical results of time evolution of crystallinity upon heating, kT (converted from the heating time) being the abscissa. For clarity, the initial increase in crystallinity during t_c is not shown.

It is evident from Figure 5.2 that T_m increases with increasing t_c, T_c, and β. The melting transition becomes broader with increasing t_c and β. However, the melting transition becomes broader with decreasing T_c. The broadness of melting transitions for T_c=0.12, 0.16, and 0.20 are roughly 0.12, 0.11, and 0.09, respectively. All these trends are fully consistent with experimental results.[91,92,107,108] The broad melting transition shown here is quite different from the sharp melting transition of small molecule crystals. The big difference could be explained by different geometric confinements for two systems. Polymer crystals are confined in 2D lamellae, whereas small molecule crystals are 3D objects in principle. The layer-by-layer melting of lamellar crystallites is confined in the 1D growth front, whereas melting of small molecule crystals happens over the 2D surface, e.g., spherical surface. This might be the main reason why polymer crystals tend to melt much slower than small molecule

crystals. In spite of the difference in the extent of melting rates due to different geometric confinements, both melting transitions should be the same in nature, i.e., both belong to the first order transition. Note this explanation is different from the traditional viewpoint that broad melting transitions correspond to broad distributions of lamellar thickness or perfection, each of which has different thermal stabilities and melting points.[98,102,103] In our opinion, even a single lamella without thickness distributions shows a broad melting transition.

5.3.3 Effects of Heating Rate

T_m defined by the last trace of crystallinity was plotted as functions of both heating rates and crystallization temperatures in Figure 5.3a. It can be seen that T_m is proportional to the square root of heating rates for all T_c's. The curves in the low-T_c region overlap on one another. At the slowest heating rate $\beta = 10^{-9}$/MCS, T_m becomes independent of T_c and equal to 0.238±0.001.

The increase of T_m with β observed in Figure 5.3a was virtually termed as "superheating" effects,[94-96] which is essentially a matter of supplying heat to the crystal faster than the crystal can melt (the heating rate greater than the melting rate of lamellae). Recently superheating was described by theoretical equation of "melting kinetics":[95,103]

$$T_m(\beta) = T_m(\beta = 0) + b\beta^n \tag{5.8}$$

where $T_m(\beta = 0)$ is defined by the extrapolation of the T_m vs. β^n line to axis of $\beta = 0$, b and n are constants. Many experiments revealed $n = 0.5$, viz. $T_m \sim \beta^{0.5}$.[96-99,104,109]. It

is noteworthy that various T_m vs. $\beta^{0.5}$ lines at different T_c's in Figure 5.3a have different slopes and they converge into a single point for the slowest heating rate. This is in contradiction with some experiments,[97,99,104,109] where the slopes at different crystallization temperature are assumed to be parallel (e.g., Figure 5.3b). Actually it was assumed that these lines at different T_c's have identical slopes and can be extrapolated to $T_m(\beta = 0)$'s, which is in turn used to construct a better HW or GT plot.[98,99,103] Such a discrepancy is attributed to the fact that experiments are usually performed within much narrower T_c and β ranges than our simulations do. For example, kT_c=0.12~0.20 correspond to roughly a range of 130°C, ten times larger than the normal temperature range (10-20°C) employed in experiments. In experiments, the heating rate normally varies from 1 to 50°C/min. However, in our simulations, β changes more than 1000 times. The converging effect at the slowest heating rate is not totally new. As mentioned in the Introduction, the "slow heating technique"[100] (e.g. increasing 1°C per hour) revealed T_m thus obtained is independent of T_c, corresponding to the converging point in Figure 5.3a. Thus the T_m vs. $\beta^{0.5}$ plot needs to be re-evaluated in experiments over a much wider T_c and β ranges to test this converging effect. If it is true, the forgoing methods of extrapolation of the T_m vs. $\beta^{0.5}$ lines to $\beta = 0$ and the more "correct" HW or GT plots based on the extrapolations all become questionable.

5.3.4 Effects of Crystallization Temperature

Figure 5.4a depicts the HW plot using the same data in Figure 5.3a in order to obtain T_m^0. At the slowest heating rate, T_m is constant with increasing T_c, in accord with the observations in slow heating technique.[91,92] At faster heating rates, T_m remains constant in the low-T_c region, whereas increases linearly with T_c in the high-T_c region. The best linearity is achieved at the highest heating rate $\beta = 1000 \times 10^{-9}$ / MCS, where the slope of T_m vs. T_c in the high-T_c region is shown to be $K = 0.55$. A consensus has been reach that, for the HW plot, K is usually in the range of 0.3~0.6,[105,110,111] most likely in the order of 0.5.[91,92,110,112] According to Equation (5.4), $K = 0.5$ corresponds to the thickening coefficient $\gamma = 2$. However, there is no a priori reason for this unique value of $\gamma = 2$, i.e., the thickness of the crystallites that is melting is exactly double that of the initial virgin thickness.[93] In Figure 5.4a, for different heating rates, kT_m^0 extrapolated by linear or nonlinear HW plot might be any value above 0.24, raising a serious question on validity of the HW plot. The exponential dependence of T_m on T_c and the inability of the HW plot to extrapolate T_m^0 are both consistent with experimental results,[34,93,110,111,113] as an example shown in Figure 5.4b.

5.3.5 Effects of Crystallization Time

The dependence of T_m on t_c is depicted as symbols in Figure 5.5(left). It appears that the linear relation $T_m \sim \log t_c$ is valid only for intermediate time range. Over the entire time range, the plot of T_m versus $\log t_c$ shows sigmoidal shapes. Such a sigmoidal behavior is not entirely new. Recent work by Marand et al.[108] revealed that

T_m increases with $\log t_c$ in sigmoidal fashion. The sigmoidal shape was attributed to primary and secondary crystallizations though. Earlier work also revealed that the linear relation $T_m \sim \log t_c$ is not universal over the full time landscape. The slope of T_m vs. $\log t_c$ was found to change with time (either becomes steeper[105] or shallower[102,105]). Sometimes T_m is constant with time.[105,112] Now we understand that the slope change behavior is only a part of the sigmoidal behavior.

The sigmoidal dependence of T_m on $\log t_c$ reminds us of the sigmoidal dependence of $\log R$ on $\log t_c$ in Figure 4.9a. We tried to put two data together. The lines in Figure 5.5 are data of $\log R$ taken from Figure 4.9a. Both T_m and $\log R$ data share the same abscissa $\log t_c$ in the same t_c range. The one-to-one correspondence between T_m and $\log R$ is evident. Both them show a sigmoidal dependence on $\log t_c$. To further confirm this correspondence, we plot T_m vs. $\log R$ directly, and the results show very good linearity (figure not shown), i.e., $T_m \sim \log R$.

5.4 Conclusions

A broad melting transition is observed in simulations and attributed to the geometric confinement inherent in 2D polymer lamellae (slow layer-by-layer melting). The melting transition becomes broader with decreasing crystallization temperature T_c, increasing heating rate β or crystallization time t_c.These trends are universal but their extents strongly depend on the setting of other parameters because the effects of t_c, T_c, and β are correlated. The melting temperature T_m depends on β, t_c, and T_c as follows:

1. $T_m \sim \beta^{0.5}$. At extremely slow β, T_m becomes history-free (independent of T_c and t_c), consistent with the slow heating technique.
2. T_m is constant in the low-temperature region and then increases linearly with T_c in the high-temperature region (with a slope in the range of 0-0.55), challenging the validity of the HW plot.
3. T_m increases with $\log t_c$ in sigmoidal fashion. This suggests $T_m \sim \log R$, in direct contradiction with the traditional view that T_m and lamellar thickness L are strongly correlated.

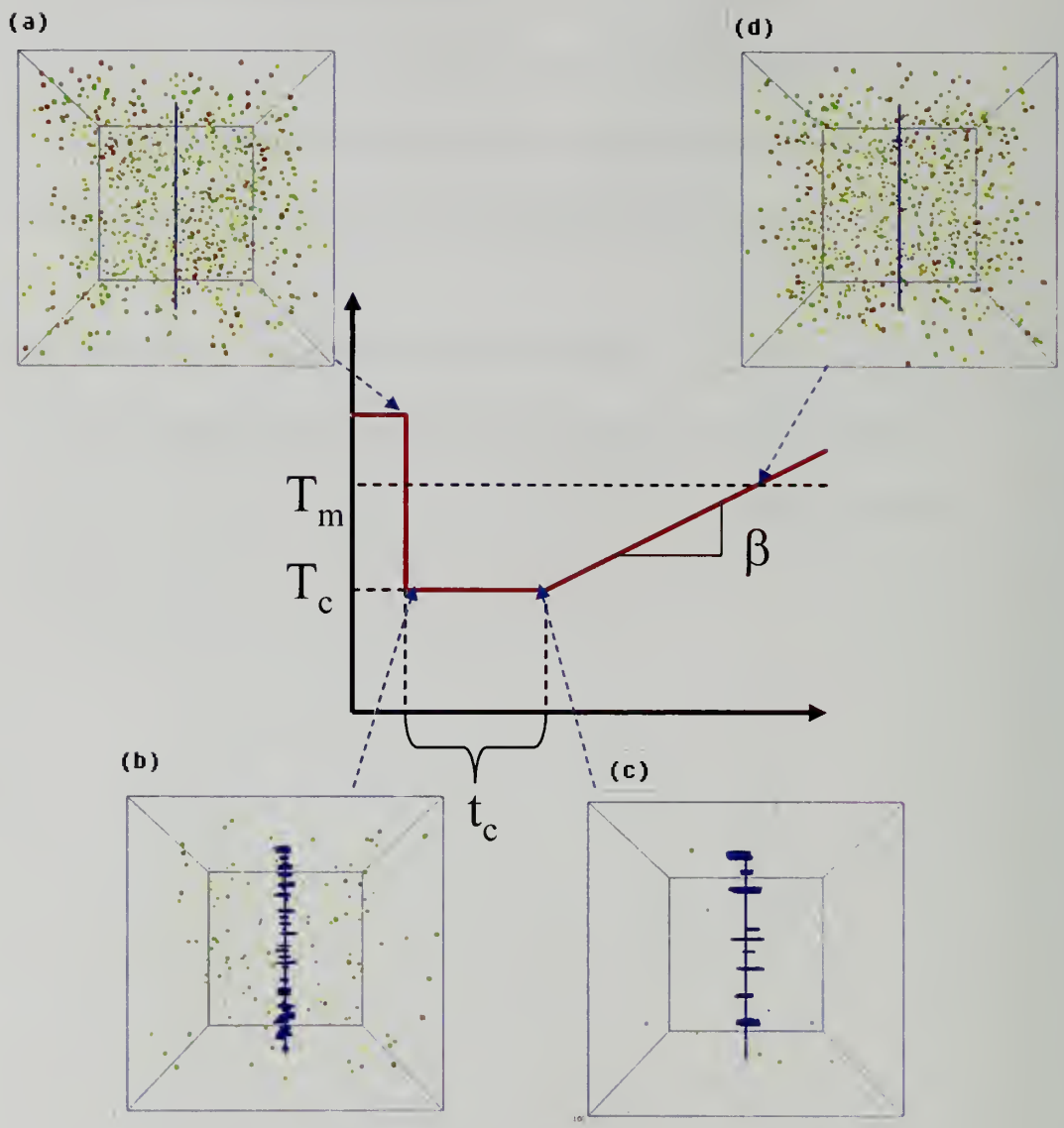

Figure 5.1: T_c is isothermal crystallization temperature, t_c is crystallization time, and β is heating rate. The melting point T_m is obtained as the temperature at which the last trace of crystals disappears.

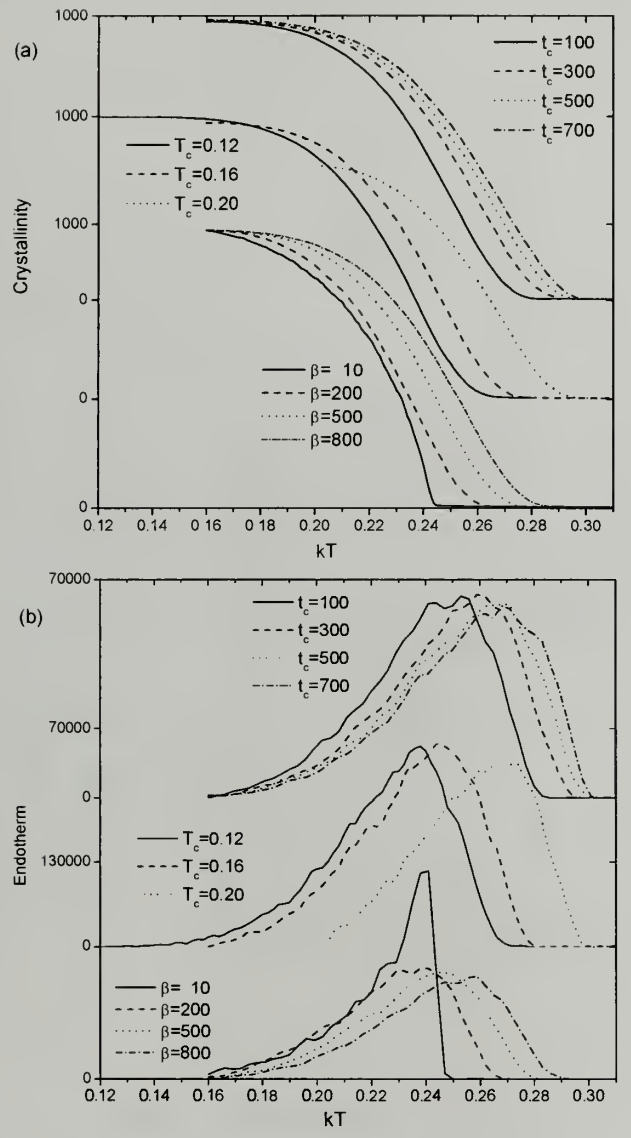

Figure 5.2: Melting transition upon heating: time evolution of crystallinity in (a) and endotherm in (b). kT (converted from heating time) is the abscissa. C=0.001. The upper part shows effects of t_c with unit $\times 10^5$ MCS. All four curves are under the conditions $\beta = 5\times10^{-7}$ /MCS and $T_c = 0.16$. The intermediate part shows effects of T_c. $\beta = 5\times10^{-7}$ and $t_c = 5\times10^6$ MCS. The lower part shows effects of β with unit $\times 10^{-9}$/MCS. $T_c = 0.16$ and $t_c = 5\times10^6$ MCS.

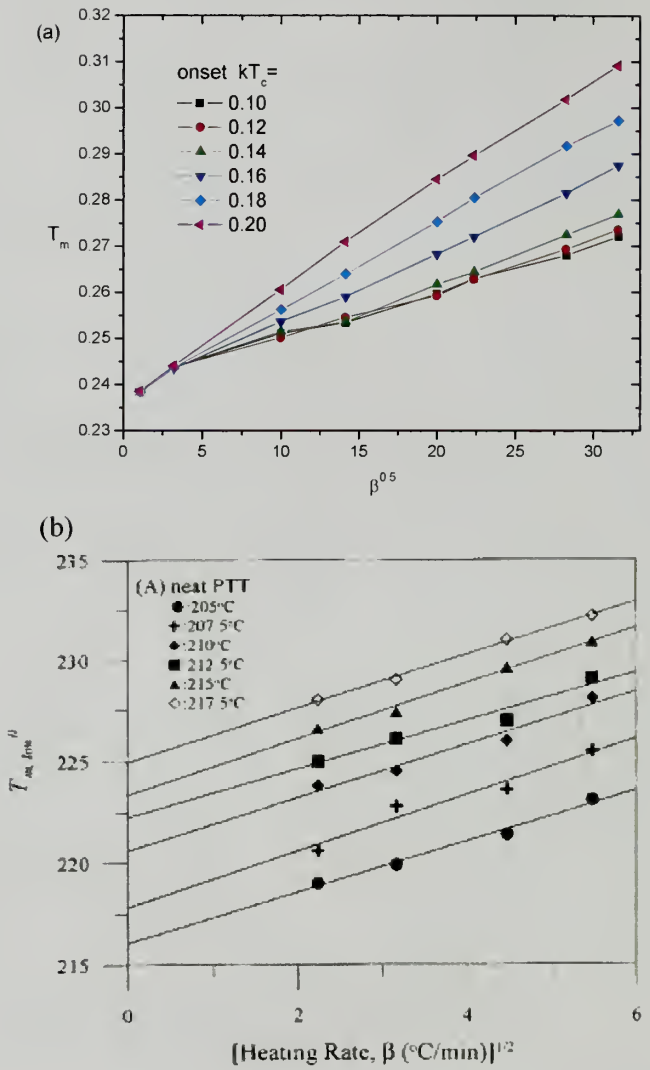

Figure 5.3: Melting temperature is proportional to the square root of heating rate. (a) Simulations. (b) Experiments.[104]

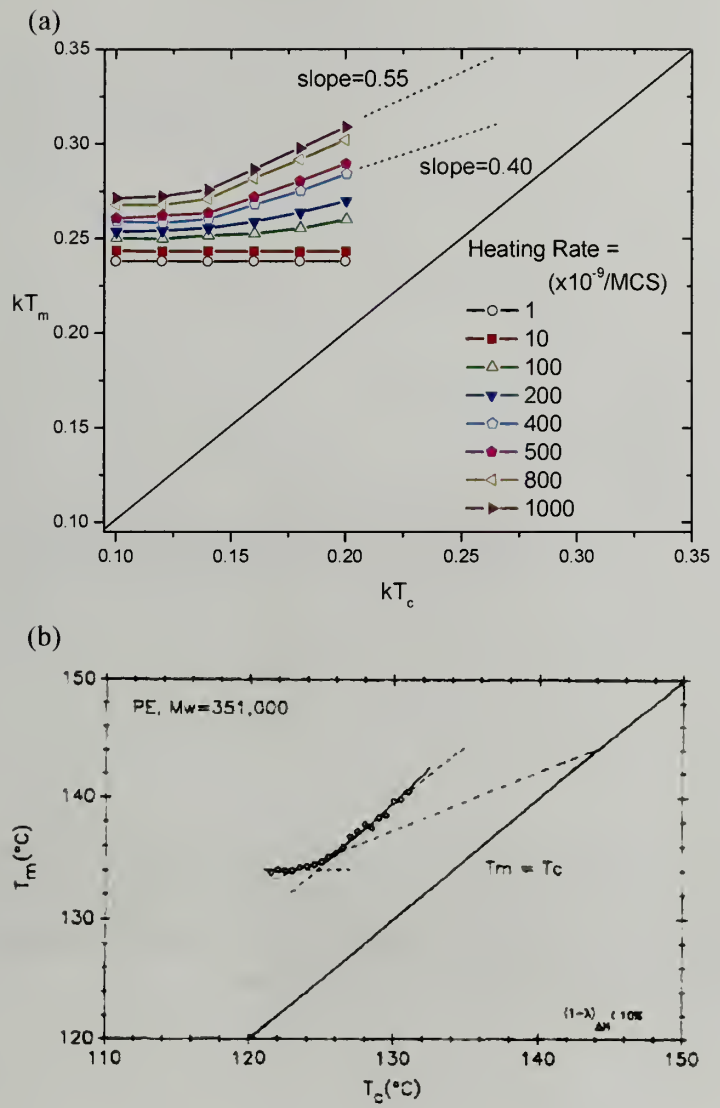

Figure 5.4: The dependence of melting temperature on crystallization temperature (Hoffman-Weeks Plot). (a) Simulations. (b) Experiments.[93]

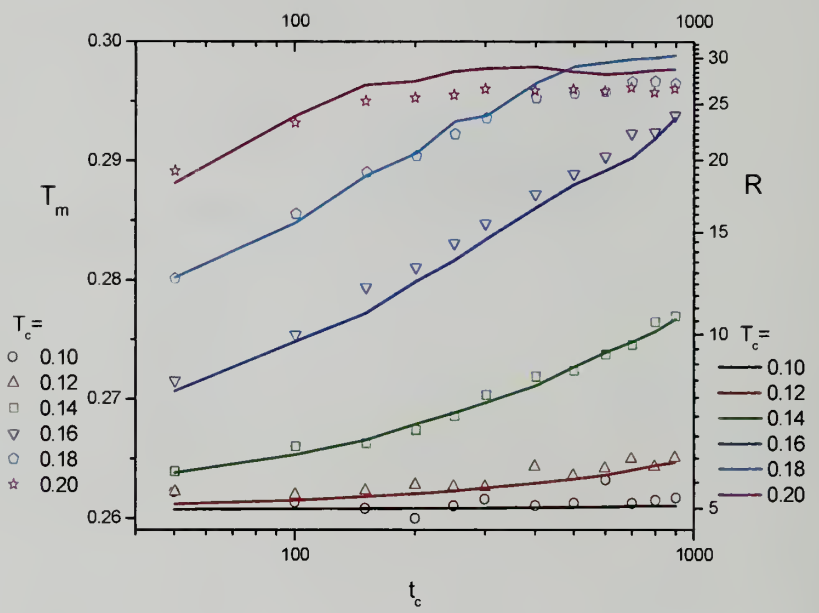

Figure 5.5: T_m increases with $\log t_c$ in sigmoidal fashion. The one-to-one correlation between T_m and $\log R$ is evident. T_m values are represented by the symbols and $\log R$ values by the lines, sharing the same abscissa $\log t_c$ in the same range. $\log R$ data are extracted from Figure 4.9a in the previous chapter.

CHAPTER 6

AMYLOID FIBRILLIZATION

6.1 Introduction

Deposition of amyloid fibrils is associated with a variety of serious diseases, including Alzheimer's disease, Huntington's disease, and prion diseases.[114,115] Identifying the key steps in the formation of amyloid fibrils may reveal important information for inhibition or reversal of fibril formation. Furthermore, recent reports suggested that the toxicity of Aβ and other amyloidogenic proteins is not due to mature fibrils, but rather prefibrillar oligomers.[116,117] Therefore, an understanding of the detailed molecular mechanism of amyloid fibrillogenesis is critical.

Despite little sequence homology, all amyloidogenic proteins exhibit fibrillar morphology and share a common cross-β sheet structure, with β strands perpendicular to and inter-strand hydrogen bonds parallel to the fibril axis. The morphologies of amyloid fibrils are typically unbranched fibrils of 10 nm in width and of 0.1-10 μm in length.[118] The cross-β structure is demonstrated by two characteristic scattering bands produced at 0.5 and 1.0 nm, corresponding to the inter-strand and inter-sheet distances.[119] Several structural models have been proposed and can be roughly classified into two major categories: (1) Ribbon-like model such as polar zippers,[120] continuous zippers,[121] pair-of-sheets steric zipper,[122] and double-layered β-sheets.[123] (2) Helical model such as water-filled nanotudes,[124] double helix,[125] and helical array of β-sheets.[126] Unfortunately, even for the ribbon-like model alone, it is still uncertain about whether intra-sheet neighboring strands are parallel or anti-parallel;[119] uncertain about

the nature of inter-sheet interactions (van der Waals?[122] hydrophobic?[123] or steric interdigitation?[121]); and uncertain about functions of side chains (H-bonding?[120] interdigitation?[121] or π-π aromatic stacking?[127]). This situation is further exemplified by the fact that two entirely different models have been proposed for the exactly same diffraction data.[121,124] From the above analysis, it is evident that there is no universal molecular-level structure model for all amyloid fibrils.[118] The only consensus we can reach now is that they all form the fibrillar morphology with the cross-β structure, where the inter-sheet interactions are always weaker than the intra-sheet H-bonding interactions. This consensus will serve as the basis for our above-molecular-level coarse-grained model.

It has been widely accepted that formation of amyloid fibrils is nucleation-dependent. Three criteria as the evidence of nucleation were proposed:[8,9] (1) There is a critical protein concentration below which no aggregation occurs. (2) Above this critical concentration by a small amount, there exists a lag time before fibrillization occurs. (3) The lag time can be reduced or even eliminated by adding a preformed fibril, which is known as the "seeding" phenomenon. These three criteria were indeed confirmed by numerous experiments.[128-137] However, the exact nature of the nucleus has yet been determined. The nucleus might possibly be a micelle,[138] a colloidal aggregate,[139] one turn of a helix,[8] or even a folded monomer.[140] Another mystery lies in how these amyloid nuclei grow after the nucleation stage. Although transient appearance of protofibril oligomers has been identified at the early stage of fibrillogenesis, their function has not been determined: protofibrils might act as an off-pathway reservoir in rapid equilibrium with monomers, the latter of which slowly assemble into fibrils; or

protofibrils are on-pathway precursors of the mature fibrils.[141,142] Even if protofibrils are indeed on-pathway precursors, it is still unclear about whether the protofibril-to-fibril transition is dominated by sequential addition of monomers or by coalescence of protofibrils (end-to-end association or lateral attachment).[142] The present study aims to shed new light on both nucleation and growth processes.

On the other hand, high-resolution microscopy has revealed that amyloid protofibrils have a bead-like structure (ca. 5nm in height), where young protofibrils appear as dimmers, trimers, and oligomers of these beads.[139,143-145] In situ observations also demonstrated that protofibril elongation occurs by aggregation of these beads from solution.[144,145] Here we take this bead as the assembly unit in our model. The molecular detail inside the bead is omitted such that only anisotropic interactions between beads are assumed, which is self-evident because beads align into a linear fibril rather than a planar or a spherical aggregate.

6.2 Model and Simulation Algorithm

Two slightly different algorithms are employed in the present study: one is for multiple fibrils; the other is for single fibril. The single fibril model is very similar to the single crystal model in Chapter 3. The distinction is that more anisotropic interactions are defined here in order to form fibrils instead of lamellae. In comparison with the single-fibril model, the multi-fibril model further releases the constraint that free beads in solutions do not interact.

The aggregation unit in our model is represented by a cuboidal brick shown in Figure 6.1, based on an assumption that the interactions between units are different

along the x, y, and z directions. The brick may stand for an extended peptide, a folded peptide, a pair of peptides, or even a bead-like aggregate of peptides as suggested in the Introduction, as long as the brick represents the smallest dynamic unit in the fibrillization process. For simplicity, we assume as an example that each brick represents an extended peptide, as shown in Figure 6.1. Simulations of peptide aggregation are all performed in a cuboidal simulation box with length B_x, B_y, and B_z, under periodic boundary conditions. Typical values for $B_{x,y,z}$ range from 50 to 500. The simulation box is further discretized into $B_x \times B_y \times B_z$ cubic lattices, each with length 1. Each cubic lattice is assigned a state from 7 possible states, as illustrated in Figure 6.1: state S_0, solvent cubic lattice (invisible area in the box); state S_1 and S_2, the x-oriented peptide with its wider lateral sides facing the z and y directions, respectively; state S_3 and S_4, the y-oriented peptide facing z and x, respectively; state S_5 and S_6, the z-oriented peptide facing y and x, respectively. For the single-fibril case, an additional state S_7 (with the same orientation as S_6) is introduced to serve as a seed nucleus.

The simulation procedure for multiple fibrils is given first as follows. Initially, a specific number ($B_x \times B_y \times B_z \times C$, where C is the initial peptide concentration) of peptides with random orientations ($S_{1\text{-}6}$) are put at random locations in the simulation box. The rest of lattices are assigned to the solvent state (S_0). Next, randomly select one peptide. Let it randomly walk to any of its six nearest neighbors and randomly changes its orientation (if the walking direction is blocked by another peptide, quit the walk and go back to randomly select another peptide). Calculate its energy state before

(E_0) and after (E_1) such a random walk. Decide whether to accept the walk based on the acceptance probability in the classical Metropolis algorithm:[47]

$$P = \begin{cases} 1 & \text{when} \quad \Delta E \leq 0 \\ \exp\left(\dfrac{-\Delta E}{kT}\right) & \text{when} \quad \Delta E > 0 \end{cases} \tag{6.1}$$

where the energy change $\Delta E = E_1 - E_0$, k is the Boltzmann constant, and T is absolute temperature. Repeat the above procedure for several billion times. The number of iterations is given in units of Monte Carlo step (MCS). At 1 MCS, the number of attempted random walks is equal to the total number of peptides in the simulation box. As is conventional for Monte Carlo simulations, all temperatures are given as kT with units of energy rather than just temperature. Based on their physical meanings, the random walks can be classified into four different categories: diffusion ($E_0 = 0, E_1 = 0$), adsorption ($E_0 = 0, E_1 < 0$), desorption ($E_0 < 0, E_1 = 0$), and rearrangement within the fibril ($E_0 < 0, E_1 < 0$).

The energy setting is as follows. The Hamiltonian for the simulation is calculated as the sum of interaction energies between each peptide *i* and its nearest-neighbor peptide *j* (if any exist):

$$H = \frac{1}{2}\sum_{i=1}^{N}\sum_{j=1}^{6} E\left(q_i q_j\right) \tag{6.2}$$

where the change of the total Hamiltonian, ΔH, is equivalent to the local ΔE in Equation (6.1) for each random walk, N is the total number of peptides, q is the state/orientation of the peptide (i.e. $S_1 - S_6$), and $E\left(q_i q_j\right)$ is the bond energy between neighboring peptides in arbitrary units of energy and is a function of the states of the

two neighboring peptides. It should be noted that the bond energy is defined differently along the x, y, and z directions. Take, for example, the case of Figure 6.1(right panel), where aggregated peptides are z-oriented and x-faced. To illustrate the multi-fibril case first, we temporarily assume they are in state S_6 instead of S_7. For each individual peptide in the state $q_i = S_6$, the total bond energies with its six nearest neighbors, $\sum_{j=1}^{6} E(q_i q_j)$, are counted according to the following five rules: if there is any peptide with the same orientation ($q_j = q_i$) in its two nearest neighbors along the x direction, they will form stronger intra-sheet H-bonds ($E_x < 0$); if there is any equal-oriented peptide in its y neighbors, they will form weaker inter-sheet attractive interaction ($E_y < 0$); if there is any equal-oriented peptide in its z neighbors, they are not allowed to grow along z to form a "β-sheet" structure so that a repulsive interaction is set to avoid it ($E_z > 0$); if there is any peptide with different orientations ($q_j \neq q_i$) in its six nearest neighbors along the x, y, or z directions, such a configuration is unstable and impractical (set repulsive $E_n > 0$ to avoid it); the interaction with solvent is always set to zero so that the solvent acts like an empty site. Since only the dimensionless ratio $\Delta E / kT$ controls the acceptance probability of random walks, we reduce E_y to -1 and determine an appropriate range of kT values by trial and error. Different magnitudes of $E_x = (-1) \sim (-15)$ have been tried and a good fibrillar morphology is obtainable only when $E_x \leq -10$. The magnitudes of E_n and E_z do not affect the "cross-β" fibril formation as long as certain repulsion exists to avoid forming non-parallel configurations or the "β-sheet" structure. A typical large value

$E_n = E_z = +10$ is chosen to ensure that it would not occur. Note that the above setting of $E_{x,y,z,n}$ is only concerned with z-oriented and x-faced peptides ($q_i = S_6$). For peptides with other orientations ($q_i = S_{1\text{-}5}$), the interaction energies $E_{x,y,z,n}$ have to be redefined in a corresponding way.

The preceding setting is merely devoted to the multi-fibril algorithm. For the single-fibril algorithm, several modifications are needed. First, a seed nucleus (S_7) with length $n_x \times n_y$ is put at the origin of the simulation box at the very beginning. In order to form a single fibril, the interactions between freely diffusing peptides ($S_{1\text{-}6}$) are disabled. The free peptide ($S_{1\text{-}6}$) has to diffuse to the vicinity of the seed peptide (S_7) to get adsorbed, thus converting its own state to S_7. The once-adsorbed peptide has the probability $P = \exp(-\Delta E / kT)$ to desorb or rearrange at a later time. But the initial seed is fixed throughout the simulation. For details, a step-by-step procedure is given for a similar system in our previous paper.[146]

Taking polyglutamine $D_2Q_{15}K_2$ as an example, the typical size of a brick in our model is 0.48nm thick (H-bonding intra-sheet distance), 0.83nm wide (inter-sheet distance), and 7nm long (length of the extended peptide).[121] This brick-stacking scenario is supported by direct observation of striations perpendicular to the $A\beta_{11\text{-}25}$ fibril axis, with 0.48nm spacing between striations.[147] Our model can naturally apply to the case of flat-ribbon-like amyloid fibrils,[130,133,148-150] with possible extension to twisted ribbons[118,135,145,149-151] or coiled helical structure with constant interacting regions (Fig. 6*a* of Ref. [152]) if assuming cubic lattices are twisted in space as well. The stacking configuration of neighboring strands can be parallel or anti-parallel for

extended peptides,[119] or can be face-to-face[123] or side-by-side[121] for hairpin peptides. In short, our coarse-grained generic model omits molecular details inside the aggregation unit and merely focuses on kinetics of amyloid fibrillogenesis by utilizing the classical Metropolis algorithm with a simple assumption $|E_x| > |E_y|$.

6.3 Results and Discussion

6.3.1 Single Fibril

6.3.1.1 Energy Ratio vs. Length Ratio

Aggregation of diffusing peptides is driven by the reduction in the total energy via forming more and more peptide-peptide interfaces ($E_{x,y} < 0$). Apparently the kinetics is determined by two ratios: E/kT and E_y/E_x. First we fix kT to a constant value kT =1.0 to see how the energy ratio E_y/E_x influences the fibril morphology. To achieve various energy ratios, we fix E_x =−10 and vary E_y from −1 to −10. The simulation box is initially populated with random peptides and a single seed nucleus at the center. As time elapses, diffusing peptides nucleate and grow on the seed, exhibiting distinct morphologies for different energy ratios (Figure 6.2). As the energy setting along the *x* and *y* directions becomes more anisotropic, the shape of the aggregate becomes more anisotropic too, leading to a fibrillar shape at large energy ratios. The length ratio L_x/L_y (defined in Figure 6.1) is observed to increase with time and then reach equilibrium in the late stage. The equilibrium values of L_x/L_y are plotted against

E_y / E_x in Figure 6.2b. It turns out that the length ratio varies significantly from 1/1 to 35/1 when the energy ratio varies from 1/1 to 1/10. So Figure 6.2b provides a rough way to estimate the relative magnitude of peptide interactions from its morphology. For example, a ribbon-like fibril of 10nm in width and 350nm in length can be estimated to have an energy ratio 1:10 between the inter- and intra-sheet interactions. In the following context, for simplicity, the energy ratio is fixed to 1:10, the magnitude of which should not affect our general results on kinetics.

6.3.1.2 Nucleation and Growth

A typical process of nucleation and growth of single fibril is shown in Figure 6.3, where the black beads represent the seed and subsequently grown fibril, and colorful beads stand for free peptides with different orientations. Starting from a single seed at t =0, the freely diffusing peptides tend to land on the seed and grow linearly along the x direction. The initial growth is thermodynamically unfavorable,[8,129] as manifested by the size fluctuation of the protofibril. The one-dimensional (1D) protofibril grows [t =62 ($\times 10^4$ MCS)] and shrinks (t =106), back and forth, until its size is large enough to overcome the nucleation barrier. In particular, a second layer of beads (t =132) seems to help stabilize the structure. Once the stable nucleus has been formed, subsequent growth (t >132) becomes thermodynamically favorable. The lateral side surface of the final fibril is quite smooth, generating a ribbon-like morphology. Presumably it is because the peptides which are attached on the lateral sides have less binding energy ($E_y = -1$) than the peptides which are attached on the fibril ends ($E_x = -10$). It is noteworthy that nucleation appears only within a narrow range of

temperature or concentrations. At lower kT or higher C, the fibril growth is spontaneous so that the nucleation behavior is nonexistent.

6.3.1.3 Fibril Size and Lag Time

To quantify the above observations, we monitor time evolution of the fibril size, R, by counting how many beads in the fibril, as shown in Figure 6.4ab. In agreement with numerous experiments,[128-137] the fibril growth exhibits a characteristic sigmoidal curve which can be divided into three stages: (1) nucleation stage, where the fibril grows and redissolves back and forth until its size exceeds a critical nucleus size, i.e. $R > R_c$; (2) growth stage, where R is found to increase linearly with time; and (3) equilibrium stage, where R reaches a plateau as the free peptides in the simulation box are exhausted. The duration of the nucleation stage, called "lag time" τ, can be obtained from the $R - t$ curves. For the convenience of discounting wild fluctuations in the fibril size during the nucleation stage, we calculated the lag time as the time point when R reaches 50, the magnitude of which should not affect our general results. In rare cases, where the size fluctuation is larger than 50, we recorded the correct lag time manually. It is evident from Figure 6.4a that nucleation is a stochastic process.[137] Under the identical conditions, simulation runs with different random-number seeds produce quite different lag times. The distribution of lag times is found to be lognormal (data not shown). The average value of lag times is plotted in Figure 6.4c as a function of the seed size. Apparently, the lag time is reduced significantly by increasing the seed size, which is related to the "seeding" phenomenon.[8,129] Similarly, Harper *et al.* noted that the fibril formation can be seeded by the addition of (bigger) fibrils, but not by (smaller)

protofibrils.[153] Consistent with our previous argument regarding the second layer of beads, the double-layer seed is more effective in "seeding" than the single-layer seed (τ for the 1×2 seed is even shorter than τ for the 10×1 seed), the reason for which will be discussed in a later section.

Another characteristic of nucleation is so-called "critical concentration", below which fibrillization cannot occur.[8] This effect is illustrated in Figure 6.5. The lag time increases sharply with decreasing the peptide concentration,[131-137] tending to diverge at a finite concentration (critical concentration).

6.3.2 Multiple Fibrils

6.3.2.1 Time Evolution

Time evolution of morphologies and fibril size distributions in Figure 6.6ac matches very well with the experimental results in Figure 6.6bd.[143] As shown in Figure 6.6a, the simulation box is initially populated with random peptides. The diffusing peptides quickly aggregate into many short protofibrils. Then the short protofibrils elongate gradually into longer protofibrils and eventually ribbon-like fibrils, in good agreement with experimental morphologies in Figure 6.6b.[143] The number count for each protofibril size is plotted as a frequency distribution in Figure 6.6c, which agrees quantitatively in shape with Figure 6.6d:[143] the population of longer protofibrils increases while the population of shorter protofibrils decreases with time; the total number of protofibrils decreases with time too, which is evident from Figure 6.6c where the total number of fibrils, "Area", decreases from 351 to 126 as time elapses.

In contradiction to the traditional view that elongation of amyloid fibrils is irreversible,[154,155] we noticed that adsorbed peptides can reversibly desorb into free space during the elongation process, i.e., a protofibril may undergo 120 adsorption and 100 desorption events in order to grow 20 beads longer. It appears that all fibrils are in fast, dynamic exchange with the peptide solution (free diffusing peptides dissolved in free space). The fibril growth is not uniform either: some protofibrils grow faster; some grow slower; some disappear soon; some initially grow and later shrink. It seems that relatively bigger fibrils can gain more peptides than smaller ones during both their exchanges with the peptide solution, presumably due to the relatively lower desorption probability for the bigger fibrils. So it looks as if the peptides on smaller fibrils are gradually transferred onto bigger fibrils by a diffusion process. In fact, this phenomenon is widely known as "Ostwald ripening",[43,156] where bigger objects grow at the expense of smaller ones via an evaporation-condensation mechanism. During Ostwald ripening, the whole system is driven from a non-equilibrium state to an equilibrium state, by minimizing the total interfacial energy. Ideally the equilibrium state is reached when there is only one gigantic fibril left in the simulation box, which is indeed seen in our simulations for even longer time (not shown).

The above observations are not ungrounded. The AFM movies from experiments[145] revealed a highly dynamic and reversible process for assembly of protofibrils, where bead-like monomers can diffuse, align transiently forming chains and then move apart again, or elongate directly into longer protofibrils. Real-time monitoring of fibril growth by fluorescence microscopy[157] also revealed that the elongation rates for different protofibrils are not uniform. It varies significantly from

one protofibril to another. The measurements by size exclusion chromatography[142,150] revealed that the amount of oligomers first increases and then decreases, while the amount of monomers/dimers decreases monotonically with time, consistent with our morphologies and distributions in Figure 6.6. For example, in Figure 6.6c, the number of protofibrils with size 5 first rises and then diminishes, while the number of monomers/dimers with size 1 or 2 decreases monotonically with time. Interestingly, the debate as to the role of protofibrils[141,142] can be reconciled in the context of Ostwald ripening (bigger fibrils eat smaller ones). Protofibrils can be either on-pathway precursors or off-pathway monomer reservoirs, depending on their relative sizes.

6.3.2.2 Effects of Concentrations

Figure 6.7a presents the effect of peptide concentrations on morphologies of fibrils at fixed $t = 10^7$ MCS, which matches excellently with the experimental results in Figure 6.7b.[143] It is observed that the fibril length increases with increasing the initial peptide concentration. Similar to experimental results in Figure 6.7d,[143] the fibril elongation rate is a linear function, first order in the initial peptide concentration (Figure 6.7c).

6.3.2.3 Effects of Temperature

Figure 6.8a presents the effect of temperature on morphologies of fibrils at fixed $t = 10^7$ MCS, which again matches excellently with the experimental results in Figure 6.8b.[143] In both figures, increasing temperature results in longer and fewer fibrils. Similar to experiments,[143] the initial fibril elongation rate increases exponentially with temperature. As shown in Figure 6.8c, the logarithm of the initial elongation rate, $\ln G$,

is indeed proportional to $1/kT$, in good agreement with experimental results shown in Figure 6.8d.[143]

6.3.2.4 Seeding

The "seeding" phenomenon, i.e. lag time is reduced or eliminated by adding preformed fibrils, has been regarded as the key evidence of nucleation mechanism for amyloids.[8,9] Figure 6.9 illustrates the seeding behavior by showing a sigmoidal-to-logarithmic (S-to-L) shape transition after adding seeds. In this case, only pre-added seeds can grow immediately, whereas the endogenously formed seeds cannot grow immediately because they are below the critical nucleus size. For the unseeded case in Figure 6.9(lower part), the monomers quickly aggregate into many short protofibril seeds within t=5 ($\times 10^5$ MCS). However, the morphology remains the same from t=5 to 300, i.e., remains within the lag time. The fibrils have to wait until the size fluctuations happen to be large enough to overcome the nucleation barrier. At t=330, a double-layer structure is formed and turns into a stable seed. Since then, the time-mass curve enters the growth region. At t=430, the second seed starts to form, while the first seed has grown into a longer fibril. Eventually, two big fibrils are formed at t=800 when the total mass reaches equilibrium. On the other hand, for the seeded case in Figure 6.9(upper part), the only difference at t=0 is that four 20×2 seeds are added in the solution. Because these seeds are already larger than the critical nucleus size at the present conditions, they start to grow immediately. At t=300, they have grown into big fibrils and the total mass almost reaches equilibrium, in contrast to the unseeded case where it is still within the lag time. After t=350, although the total mass remains the

same, the underlying Ostwald ripening still goes on (the morphology changes from 4 fibrils to 2 bigger ones). So the fact that the total mass reaches the plateau stage does not necessarily mean that the fibril growth has stopped.[150] The above S-to-L shape transition in the time-mass curve is a typical seeding result observed in numerous experiments.[128-130,133,134] To our best knowledge, it is the first simulation to reproduce the seeding phenomenon with a clear S-to-L curve transition. In addition, our accompanying morphologies beautifully illustrate the mechanisms of the sigmoidal shape and the seeding phenomenon at the molecular scale. Incidentally, the effect of the seed concentration is also reproduced in Figure 6.9, where increasing the number of seeds results in shorter lag time.[137,140,158,159]

6.3.2.5 Disassembly upon Dilution

To complete our comparisons with Ref. [143], disassembly of preformed fibrils upon dilution is presented in Figure 6.10a. After fibrils being put into a bigger box (27-fold dilution), the fibril size is observed to decrease exponentially, reaching a plateau around $t = 750\times10^4$MCS. The rate of decrease in fibril length is much faster over the first 250×10^4MCS (size = 8.7→3.9) as compared to the subsequent 250×10^4MCS (size = 3.9→3.1). The fibril density also decreases as time elapses. All these observations agree excellently with experimental results shown in Figure 6.10b.[143]

6.3.3 Mechanism of Nucleation and Growth

One of puzzles regarding nucleation of amyloid is why a 1D fibril can have nucleation barrier?[8] According to the classical nucleation theory, the free energy change of forming a 3D spherical object is

$$\Delta F = -\frac{4}{3}\pi R^3 \Delta\mu + 4\pi R^2 \sigma \tag{6.3}$$

where R is spherical radius, $\Delta\mu$ is bulk energy gain, and σ is surface energy penalty. By setting $\partial \Delta F / \partial R = 0 = -4\pi R^2 \Delta\mu + 8\pi R\sigma$, the critical nucleus size is obtained as

$$R_c = \frac{2\sigma}{\Delta\mu} \tag{6.4}$$

For $R < R_c$, the surface energy term dominates and ΔF increases with increasing R (the fibril growth is thermodynamically unfavorable); for $R > R_c$, the bulk energy term dominates and ΔF decreases with increasing R (the fibril growth is thermodynamically favorable); at $R = R_c$, ΔF reaches maximum. So a free energy barrier is formed. In order to grow, the 3D object has to wait until its size fluctuation happens to be larger than R_c so that the free energy barrier is overcome.

For a 2D circular object, we can do similar calculations,

$$\begin{cases} \Delta F = -\pi R^2 \Delta\mu + 2\pi R\sigma \\ \dfrac{\partial \Delta F}{\partial R} = 0 = -2\pi R\Delta\mu + 2\pi\sigma \\ R_c = \dfrac{\sigma}{\Delta\mu} \end{cases} \tag{6.5}$$

For a 1D cylindrical object, however, the critical nucleus size is not obtainable,

$$\begin{cases} \Delta F = -\left(\pi \times 1^2\right) R\Delta\mu + \left(2\pi \times 1\right) R\sigma \\ \dfrac{\partial \Delta F}{\partial R} = 0 = -\pi\Delta\mu + 2\pi\sigma \\ R_c = ? \end{cases} \tag{6.6}$$

Here we assume the cylinder radius is 1 and the cylinder length is R. It seems that ΔF can either increase or decrease with R, but not both. If $2\sigma > \Delta\mu$, the 1D object never grow. If $2\sigma < \Delta\mu$, the 1D object will grow immediately. Neither free energy barrier nor critical nucleus size exists for the 1D case. So how can 1D amyloid fibrils exhibit sigmoidal growth curves and the seeding phenomenon (hallmarks of nucleation)?

As mentioned in the Introduction, the nature of nucleus remains mystery. In order to bypass the paradox of "1D nucleation", for example, one turn of a helix was proposed as a stable nucleus (R_c corresponds to the number of peptides which is required to form exactly one turn of a helix).[8] In contrast, our answer to this paradox is that the amyloid fibril is not really a 1D object, but rather a semi-2D object. As shown in Figure 6.11, monomers can aggregate into dimers, trimers, 1-layer protofibrils, 2- or 3-layer fibrils. These fibrils all undergo frequent adsorption/desorption events, i.e., they are in dynamic exchange with monomer solutions. Here the middle parts of the fibril are almost impossible to desorb due to their high binding energies. So we will focus only on the adsorption/desorption of peptides on the fibril ends. Although the adsorption probabilities are the same for all fibrils, the desorption probabilities are different for different fibril sizes, because the binding energy of end peptides is a function of the fibril size. For example, at kT =1.0, the desorption probability of 1-layer fibril is $P_{d1} = \exp(-10/1.0) = 4.5\times10^{-5}$, three times larger than the desorption probability of 2-layer fibril $P_{d2} = \exp(-11/1.0) = 1.7\times10^{-5}$. Under certain conditions (high T or low C), if the adsorption probability happens to be within this range $1.7\times10^{-5} < P_a < 4.5\times10^{-5}$, the 2-layer fibril can grow ($P_a > P_{d2}$) while the 1-layer fibril cannot grow ($P_a < P_{d1}$). Thus the fibril growth has to wait until the size

fluctuations happen to form a second layer to overcome the nucleation barrier. R_c corresponds to the size of a 2-layer fibril. This idea is consistent with the mass-per-length (MPL) measurements in experiments,[145,150] where MPL = 21, 31, 42 kDa/nm correspond to 2-, 3-, 4-layer fibrils, indicating the 1-layer fibril is more unstable. Note that the binding energy will saturate and approaches a limiting value, 12, with increasing the layers. So the stability difference between 1- and 2-layer fibrils is larger than the stability difference between 2- and multi-layer (even 100-layer) fibrils. This idea is also supported by Figure 6.4c, where the reduction in τ becomes less significant with increasing the number of layers from 1 to 2, and then to 3.

Once the nucleation barrier is overcome, Ostwald ripening starts to dominate. As seen from the unseeded case in Figure 6.9, one nucleus forms earlier, while another nucleus forms later. When they grow bigger, they have different sizes. For example, one is a 2-layer fibril, and the other is a 3-layer fibril. As shown in Figure 6.11, the desorption probability of a 3-layer fibril is $P_{d3} = \exp(-11.33/1.0) = 1.2\times10^{-5}$, where 11.33 is the average binding energy for its edge peptides. As the monomer reservoir becomes exhausted (C becomes lower), the adsorption probability should also become smaller. Under certain conditions, if the adsorption probability happens to drop into the range $1.2\times10^{-5} < P_a < 1.7\times10^{-5}$, the 3-layer fibril can grow ($P_a > P_{d3}$) while the 2-layer fibril starts to shrink ($P_a < P_{d2}$). Thus it looks as if the 3-layer fibril grows at the expense of the 2-layer fibril. So the size-dependent binding energy is also the reason for Ostwald ripening. As time goes by, the free monomers become exhausted, and the nucleation barrier is essentially lifted (R_c increases with lowering C in Figure

3.5b) so that smaller fibrils tend to disaggregate while bigger fibrils tend to grow. In this sense, Ostwald ripening can be regarded as "competitive nucleation".

To test our semi-2D idea, we modified the energy setting to $E_x = -10$ and $E_{y,z,n} = +10$, which essentially ensured that the fibril growth is purely 1D. The simulation results for the single-fibril case are shown in Figure 6.12. As seen from the morphologies in Figure 6.12a, the fibril growth is indeed purely 1D. It is evident from Figure 6.12b that for a pure 1D growth the fibril can either grow immediately, or never grow. The lag time can be either zero or infinity. There is no finite lag time. The sigmoidal curve is not observable (scrutinized at kT =1.10, 1.11, ..., 1.20). This agrees with the classical nucleation theory in that a pure 1D growth has no nucleation barrier. The reason we did see sigmoidal shapes and the seeding behavior in the previous simulations is really due to the semi-2D nature (stabilization effects of the second / multiple layers).

6.4 Conclusions

We have employed the classical Metropolis algorithm with anisotropic interactions to simulate nucleation and growth of amyloid fibrils. It is surprising to see such a generic model can reproduce so many experimental results. The main findings are summarized as follows. (1) For the first time in simulations, we reproduced the sigmoidal growth curve and the seeding behavior. The underlying nucleation mechanism is confirmed and illustrated by the accompanying morphologies at the molecular scale. (2) We propose that nucleation of amyloid fibrils is due to its semi-2D nature. It is confirmed that a pure 1D growth does not require nucleation and does not

exhibit sigmoidal curves. The importance of the second layer is stressed. The mechanism of nucleation is explained by the size-dependent binding energy and desorption rate. (3) We propose Ostwald ripening (bigger fibrils grow at the expense of smaller ones) as the mechanism of amyloid fibril growth. Ostwald ripening mechanism reconciles the debate as to whether protofibrils are precursors or monomer reservoirs. (4) The elongation rate G increases linearly with the initial peptide concentration. The relation $\ln G \sim 1/kT$ is also observed. (5) The lag time is shown to be functions of three factors $\tau\left[n\left(R_0\right), R_c\left(C\right)\right]$. Increasing the seed size R_0 or the seed concentration $n\left(R_0\right)$ results in shorter τ. The 2-layer seed is more effective in "seeding" than the 1-layer seed. τ increases sharply with decreasing the peptide concentration C, diverging at the critical concentration.

Besides the above major results, this study reproduced many other experimental findings. Our simulation results agree very well with the experimental results in Ref. [143]. Longer and fewer fibrils are seen at later time points and higher temperature. The fibril size distribution matches theirs too. The disassembly upon dilution is reproduced, where the shrinkage of the fibril size is faster for the early stage than for the late stage. SEC measurements[142,150] showed that the amount of oligomers first increases and then decreases with time. AFM movies[145] revealed a highly dynamic and reversible process for assembly of protofibrils. The fluorescence microscopy[157] also revealed that the elongation rates for different protofibrils are not uniform. All these observations are consistent with the concept of Ostwald ripening.

Structure (molecular conformation and morphology), interactions, and kinetics (nucleation and growth) are three key issues in amyloid studies.[118] The amyloid fibrils,

although formed from a variety of protein precursors with different conformations and specific molecular interactions, share a common cross-β structure and a similar fibrillization process. The present generic model, by omitting the molecular details, provides a promising tool to investigate the common morphologies and kinetics for all amyloid fibrils.

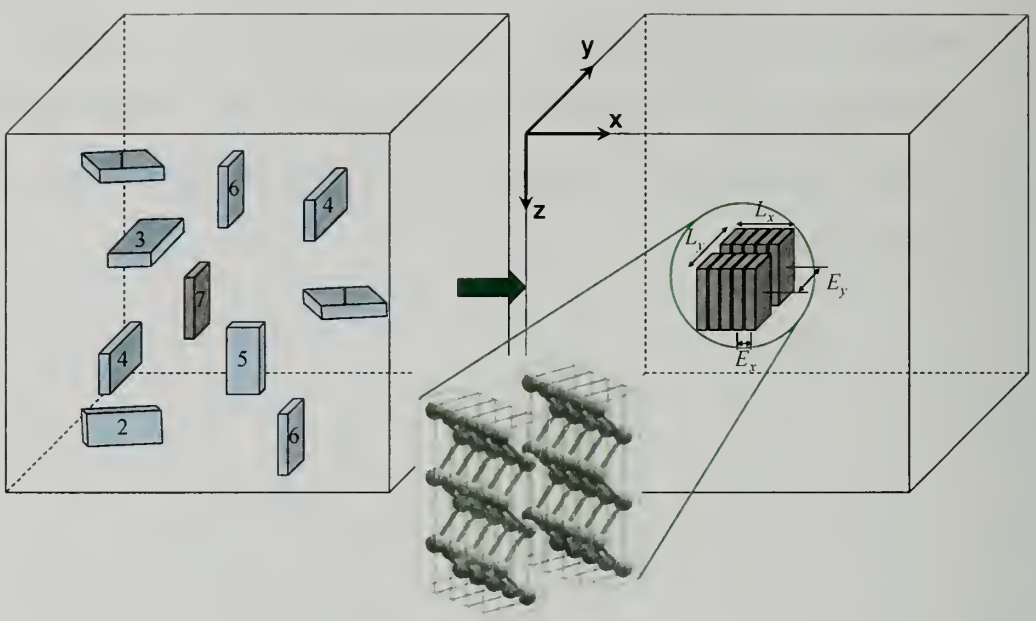

Figure 6.1: Peptide solutions for amyloid fibril formation are mapped onto a 3D array of lattice sites. Each peptide (a bead-rod chain) occupies one lattice and is represented by a cuboidal brick which randomly walks, randomly changes its orientation (state $S_1 \sim S_6$), and aggregates with other peptides when having the same orientation. The solvent (state S_0) is represented by the empty lattice which is invisible here for clarity. For the single-fibril case, an additional state S_7 (same orientation as S_6) is introduced to serve as the seed nucleus. The fibril thus formed has length L_x, width L_y, intra-sheet H-bonding interaction E_x, and inter-sheet interaction E_y.

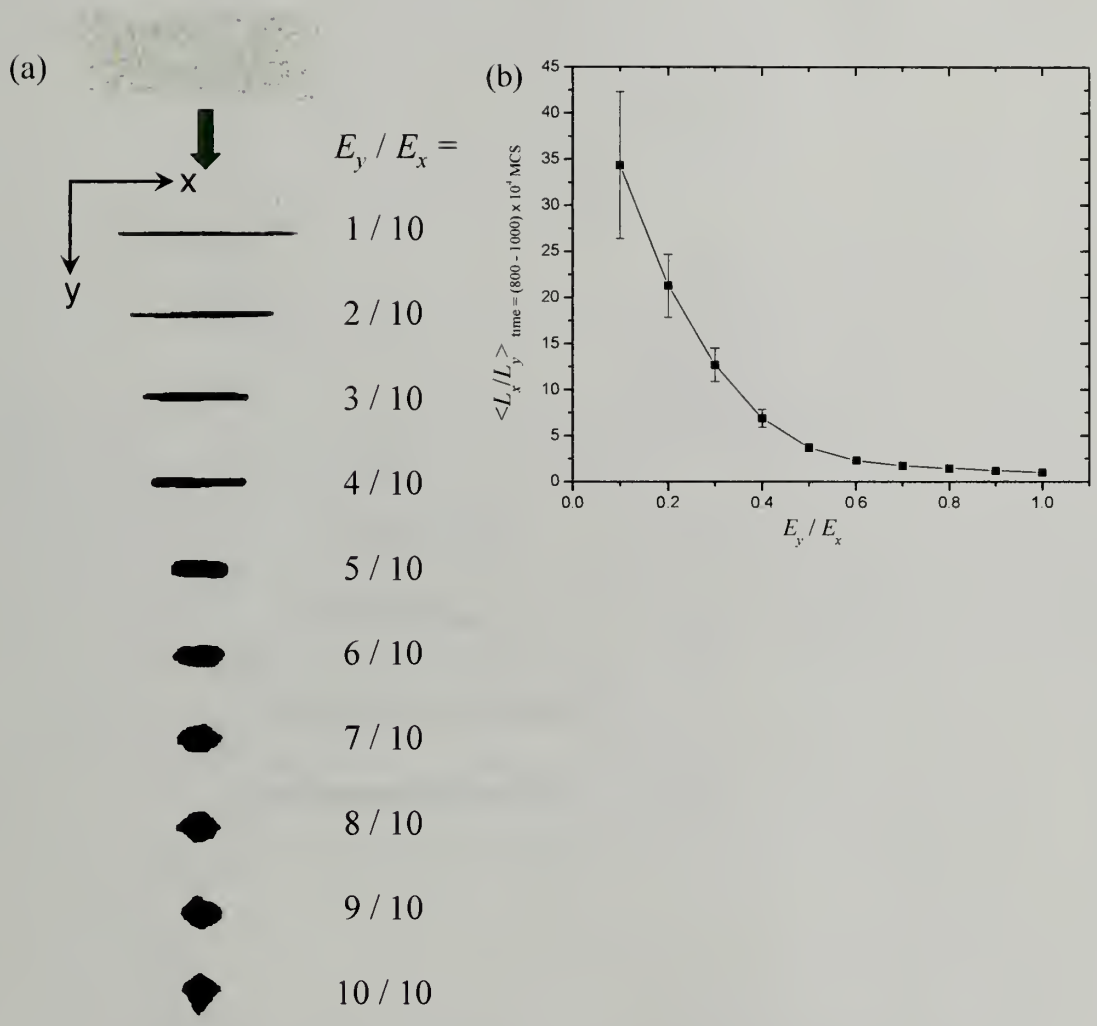

Figure 6.2: The length ratio (L_x / L_y) as a function of the energy ratio (E_y / E_x). The size of the initial seed nucleus is 1 (almost invisible); the size of the simulation box $B_x = 250$ and $B_y = B_z = 100$; temperature $kT = 1.0$; the initial peptide concentration $C = 0.0005$; the total simulation time $t_{\max} = 10^7$ MCS. (a) Initial and final morphologies for various energy ratios. (b) L_x / L_y vs. E_y / E_x. L_x / L_y is averaged over t =(800–1000)×10^4 MCS.

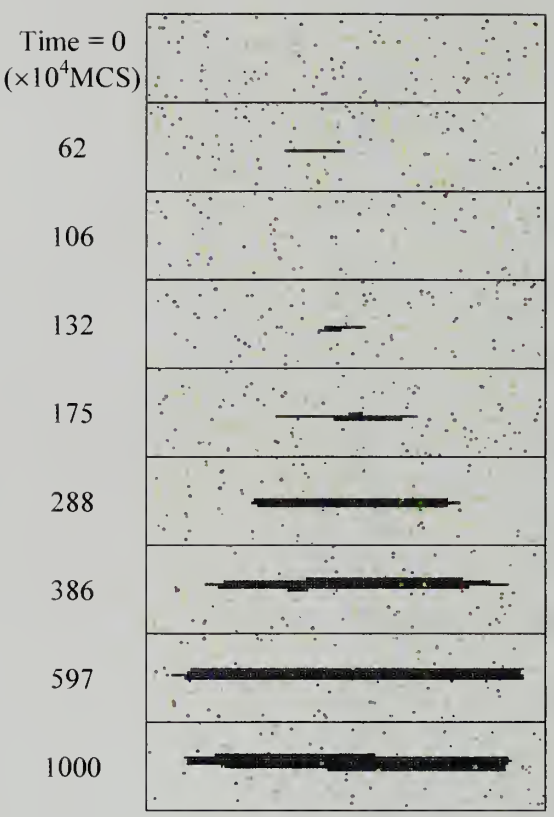

Figure 6.3: Nucleation and growth of single fibril. The seed size is 1; kT =1.17; C =0.001. All subsequent simulations on single fibrils are under the conditions $B_x = 500$, $B_{y,z} = 50$, and $t_{\max} = 10^7$ MCS. In the rest of the chapter, the default energy settings are $E_x = -10$, $E_y = -1$, and $E_{z,n} = +10$.

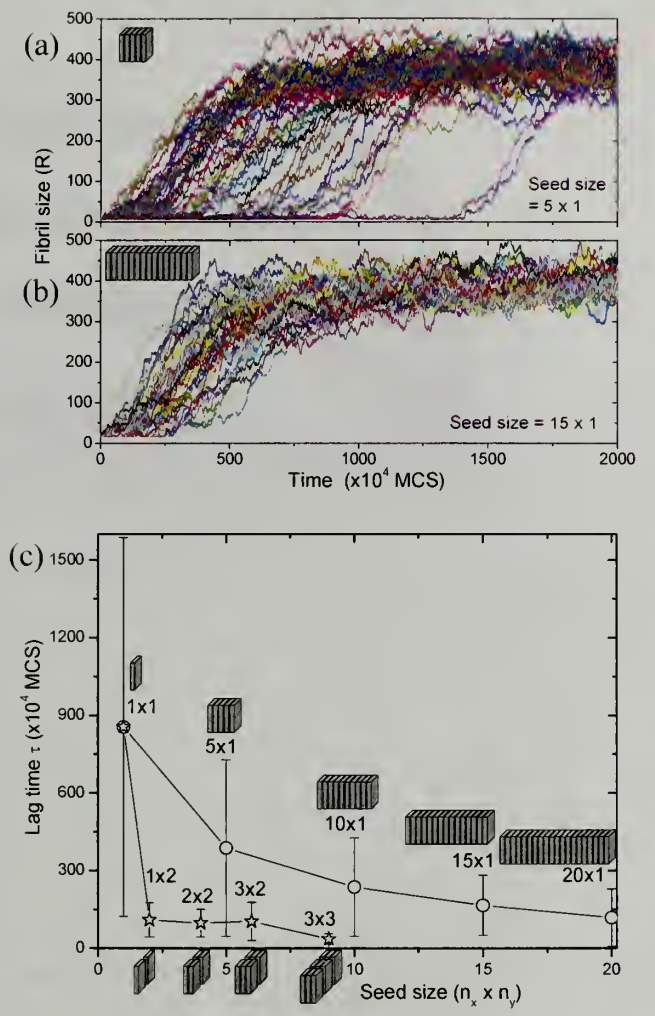

Figure 6.4: Time evolution of the fibril size (R) and the corresponding lag time (τ) as a function of the initial seed size ($n_x \times n_y$). C =0.001 and kT =1.2. (a) Smaller 5×1 seed. (b) Larger 15×1 seed. Different curves in (a, b) correspond to 50 independent simulation runs. (c) The average lag time vs. the seed size.

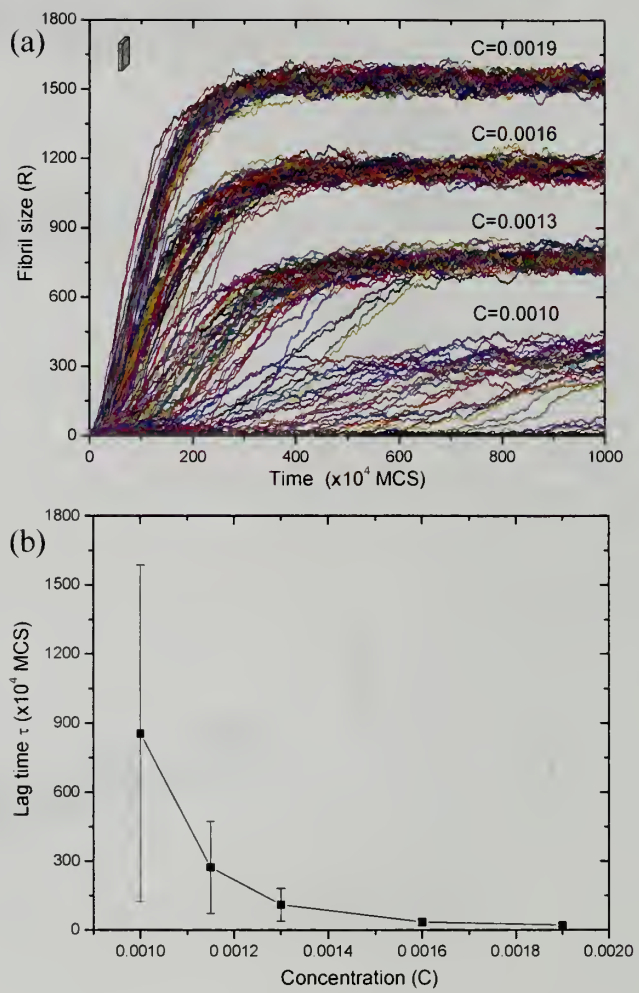

Figure 6.5: Time evolution of the fibril size (R) and the corresponding lag time (τ) as a function of the initial peptide concentration (C). kT =1.2 and the seed size is 1.

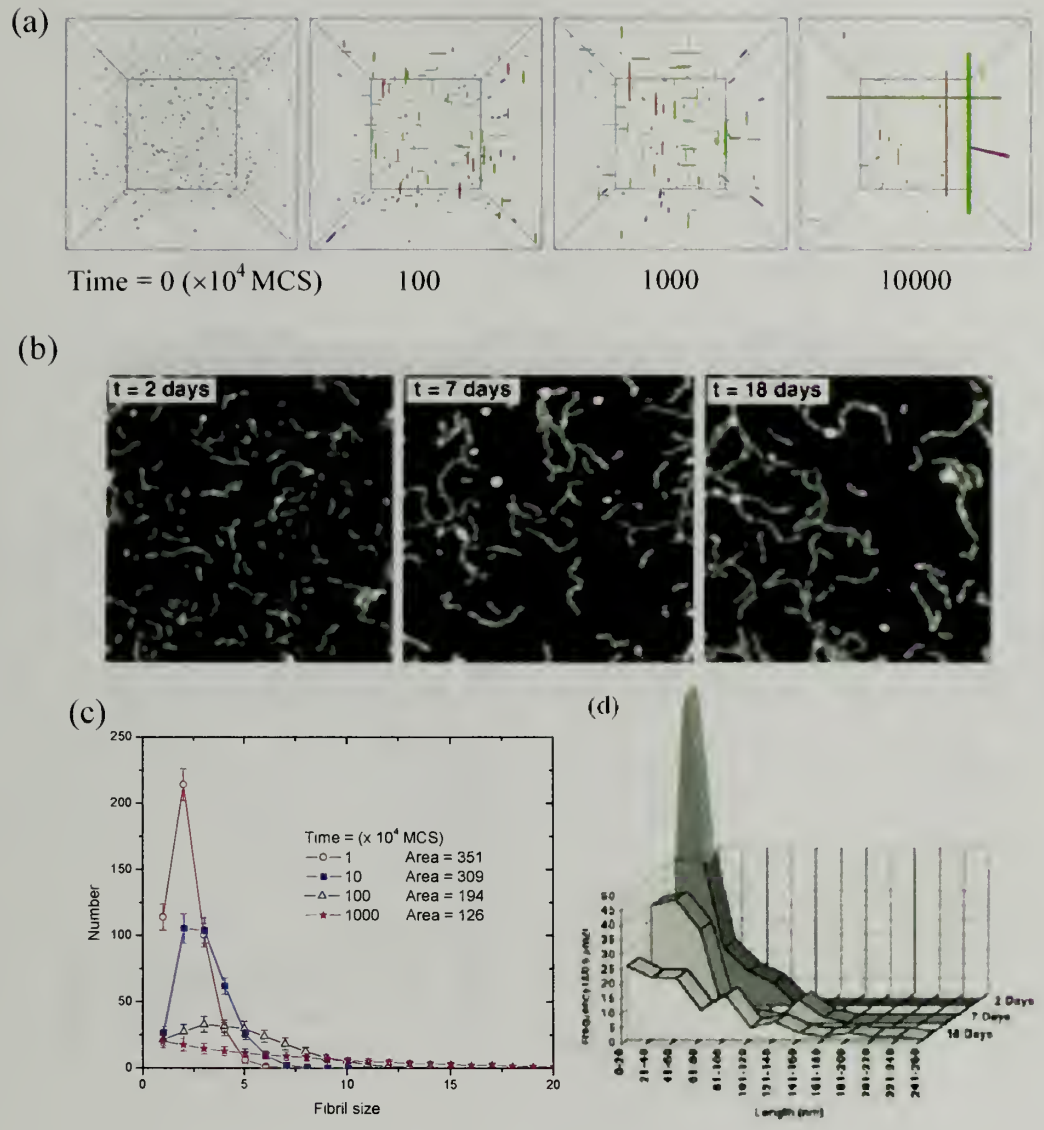

Figure 6.6: Time evolution of morphologies and fibril size distributions for multi-fibril assembly. C =0.001; kT =0.8; all subsequent simulations on multiple fibrils are performed in the simulation box with length $B_{x,y,z} = 100$. (a) Morphological evolution in simulations. (b) Morphological evolution in experiments.[143] (c) Time evolution of fibril size distributions in simulations. The integrated "Area" represents the total number of protofibrils. (d) Time evolution of fibril size distributions in experiments.[143]

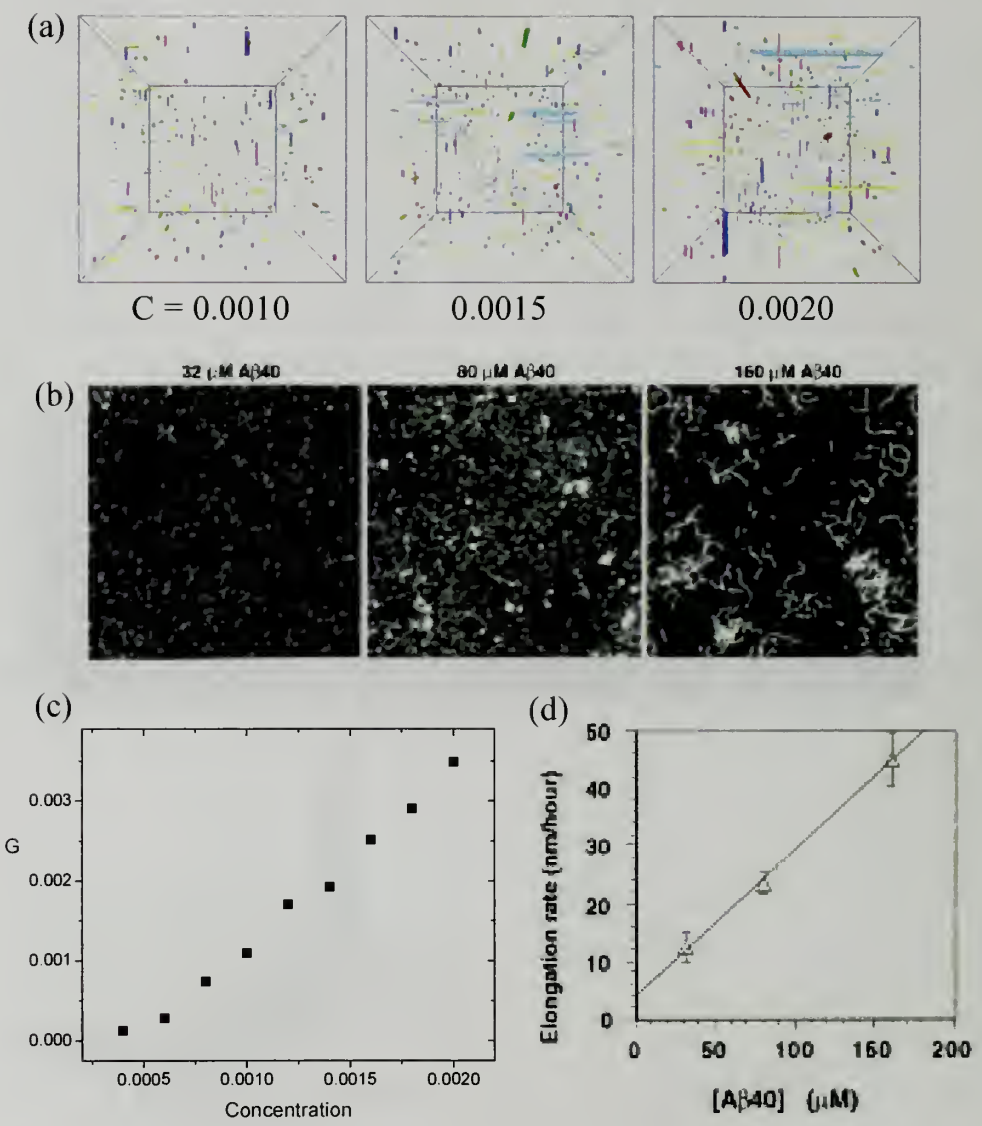

Figure 6.7: Morphologies as a function of peptide concentrations for (a) simulation results at $t = 10^7$ MCS and (b) experimental results.[143] Concentration dependence of the fibril growth rate for (c) simulation results and (d) experimental results.[143]

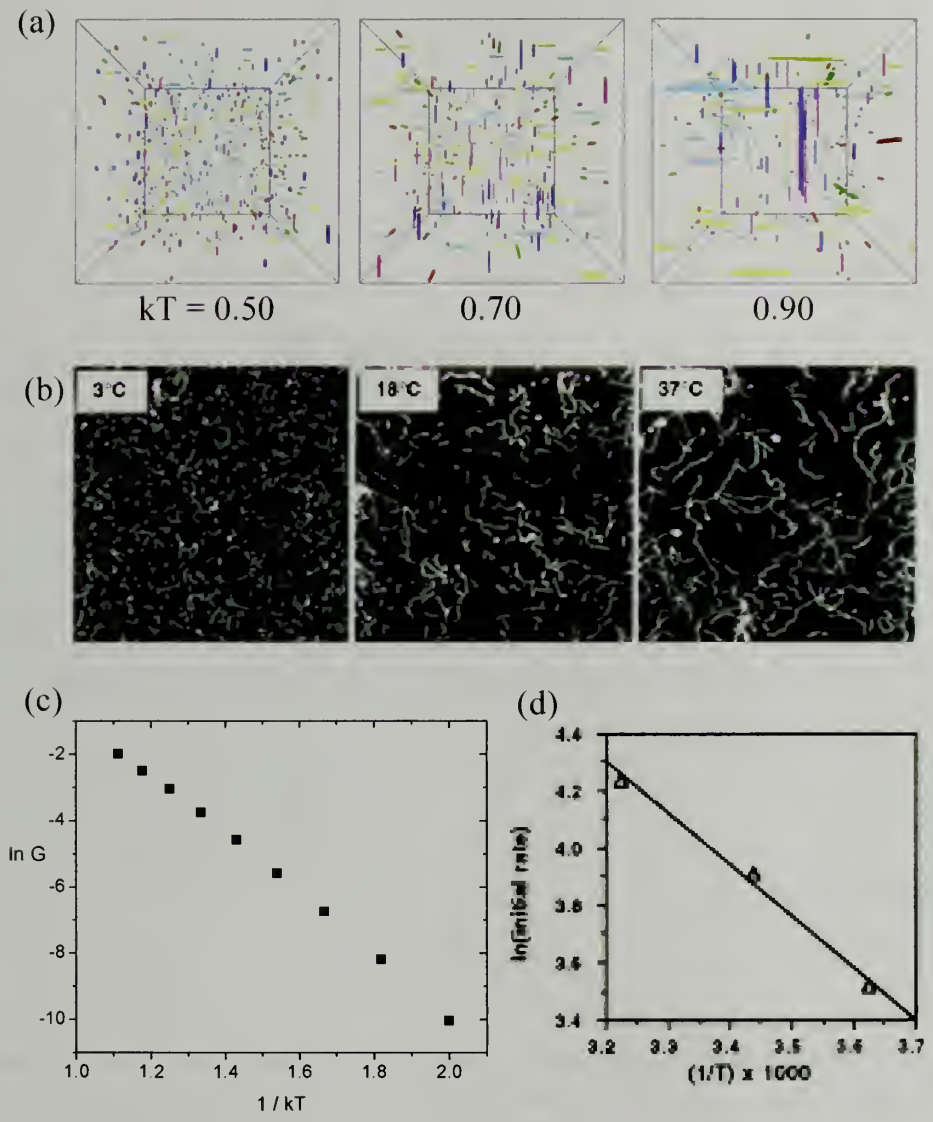

Figure 6.8: Morphologies as a function of temperature for (a) simulation results at $t=10^7$ MCS and (b) experimental results.[143] Temperature dependence of the initial fibril growth rate for (c) simulation results and (d) experimental results.[143]

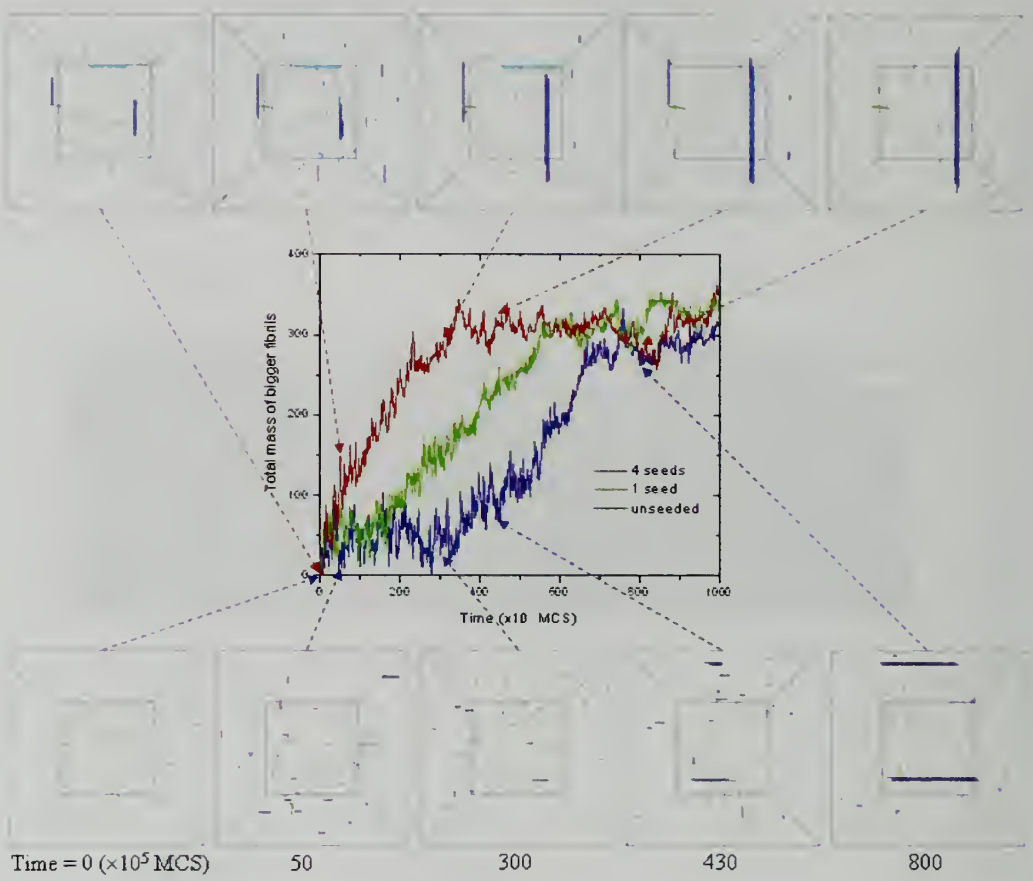

Figure 6.9: Effects of seeding and seed concentrations on fibril growth. Time evolution of the total fibril mass (based on all fibrils whose size ≥ 10) is monitored for the unseeded, 1-seed, and 4-seed cases, respectively. The corresponding morphologies for the unseeded and 4-seed cases are given at t =0, 50, 300, 430, 800 (×10^{5}MCS). The size of each seed is 20×2. C =0.0005, kT =0.9. The mass contribution due to added seeds was subtracted.[129,133] Due to the stochastic nature, only one typical run is given for the time-mass curve. The average lag time of 50 simulation runs, however, indeed decreases with increasing the seed concentration: τ =171, 74, 3 (×10^5 MCS) for the unseeded, 1-seed, and 4-seed cases, respectively.

(a)

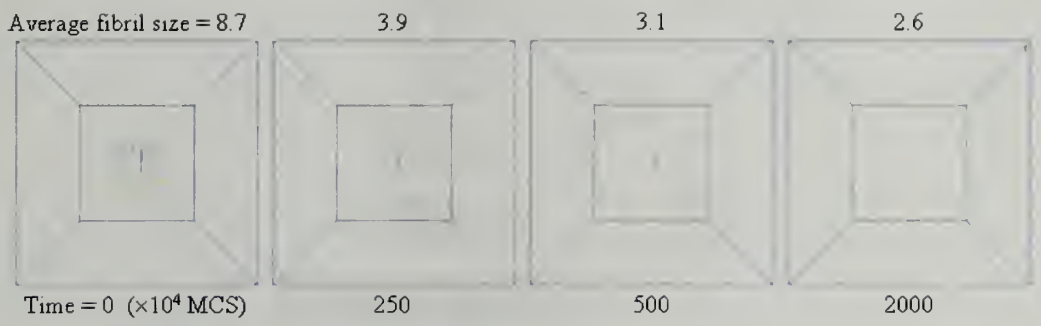

(b)

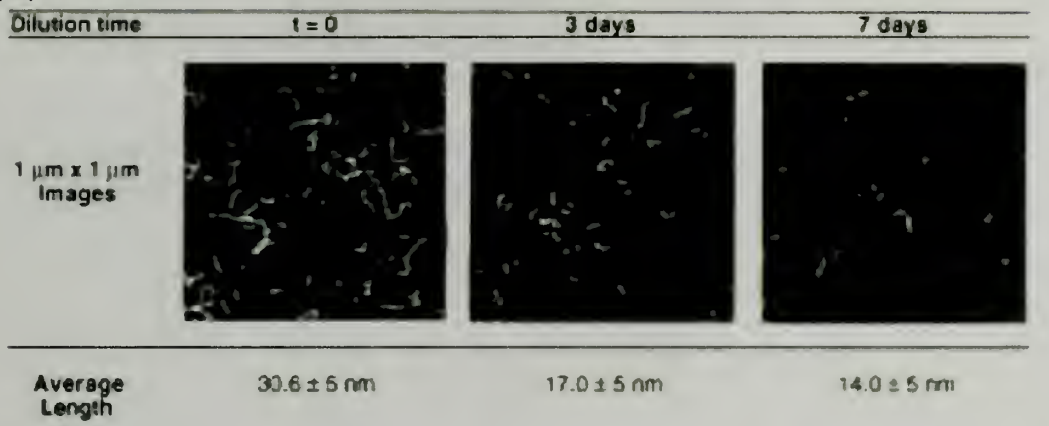

Figure 6.10: (a) Disassembly upon dilution. The already-formed fibrils (under the conditions C=0.002, kT=0.9, simulation box length 100) are put in a bigger simulation box with length 300 to simulate effects of dilution. (b) Experimental results where the sample was diluted 20-fold.[143]

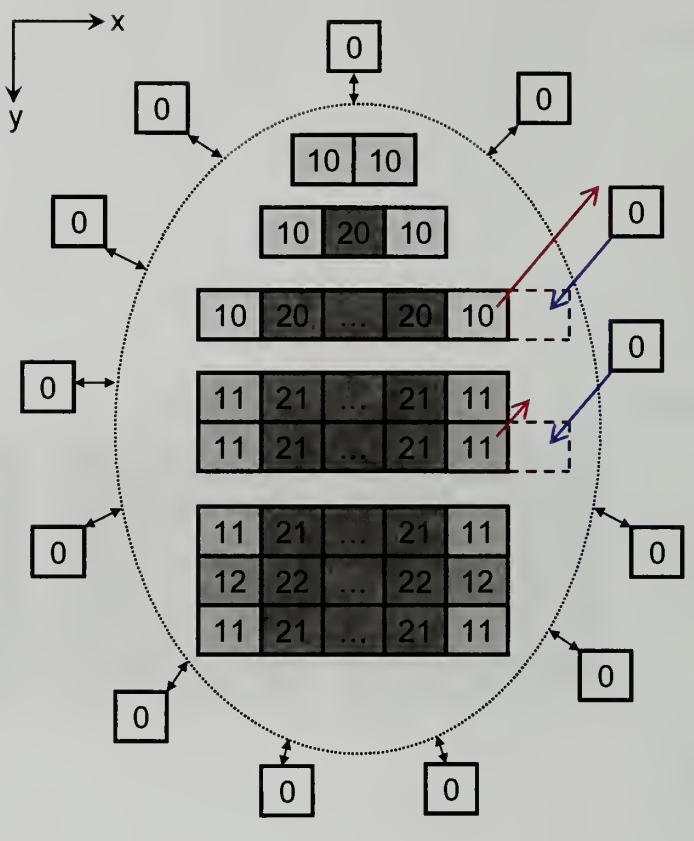

Figure 6.11: Mechanisms of nucleation and Ostwald ripening. 1-, 2-, and 3-layer fibrils are all in dynamic exchange with monomers. The number in each square represents its binding energy with nearest neighbors. The bigger the fibril, the stronger binding energy its edge peptides get, the higher thermal stability the fibril can have. Although the adsorption probabilities (blue arrows) are the same for 1- and 2-layer fibrils, the desorption probabilities (red arrows) differ. Under certain conditions, the smaller 1-layer protofibril cannot grow (adsorption < desorption) while the bigger 2-layer fibril can grow (adsorption > desorption). Once the nucleation barrier is overcome and many seeds have grown into fibrils, Ostwald ripening starts to dominate, e.g. the stability difference between 2- and 3-layer fibrils will favor the growth of 3-layer fibrils at the expense of 2-layer fibrils during their both exchanges with the more diluted monomer reservoir.

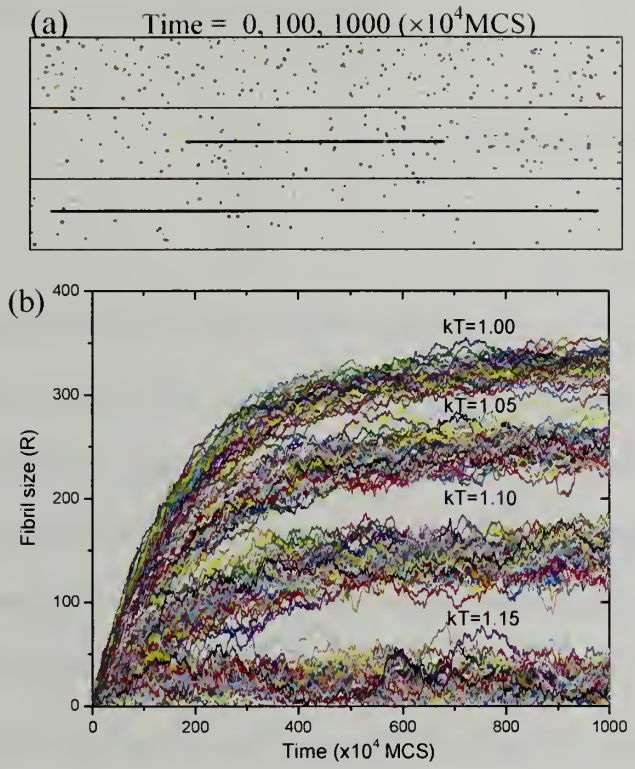

Figure 6.12: Pure 1D growth. The energy settings are $E_x = -10$ and $E_{y,z,n} = +10$. $B_x = 500$, $B_{y,z} = 30$, C =0.001. (a) Morphological evolution at kT =1.0. (b) Fibril growth at various temperatures. No sigmoidal curve is observed at any kT.

CHAPTER 7

CONCLUSIONS AND FUTURE WORK

7.1 Polymer Crystallization

7.1.1 Conclusions

Polymer crystallization from dilute solutions is simulated by both Langevin Dynamics and Monte Carlo models. The Langevin Dynamics simulations reveal that chains in dilute solutions are prefolded before aggregation and the lamellar thickness is a predetermined equilibrium result, in direct contradiction with the existing theories where chains are assumed to fold only on the growth front and the lamellar thickness is kinetically trapped in a finite value. Based on this new prefolding concept, systematic Monte Carlo simulations are performed as regards temperature and concentration dependences of crystal habits, growth rates, induction time, melting points, kebab spacings, and so on. A summary of major comparisons between the three models are given in Table 7.1, where the new model is shown to be more consistent with experimental results than the other two.

The work done here has great impact in the field of polymer crystallization. Basically it constructs a new framework for polymer crystallization in solutions, because the most basic assumption (stem nucleation, or segment pinning) is replaced by a new one (aggregation of prefolded chains). The dilemma between the low-T roughening in the LH theory and the high-T roughening in the SG model is solved by a rough-flat-rough transition in our model. The three-regime transitions in the LH theory are criticized. The exponential dependence of the growth rate on temperature is

attributed to a 2D multi-chain nucleation, rather than a 1D stem nucleation or a pinning entropic barrier. δL catastrophe is solved by introducing the concept of predetermined equilibrium thickness. Concentration dependence of the growth rate has been reproduced without invoking the cilia nucleation concept. Our simulation results suggest that α in the relation of $G \sim C^{\alpha}$ is actually not constant. In fact, this nonlinear concentration dependence is also observed for crystallization of small molecules.[160] Induction time is studied more systematically. Because the initial seed size can be explicitly specified, a novel phase diagram of critical nucleus sizes is proposed, which shows that the critical nucleus size is not a constant value but varies with environmental conditions and time. The melting results add further support to our prefolding model. For the first time, the linear relation between T_m and $\beta^{0.5}$ is reproduced in simulations. The HW plot is criticized. The relation between T_m and $\log t_c$ is found to be sigmoidal, consistent with recent experimental results. The sigmoidal shape of T_m is found to be closely related to the sigmoidal dependence of $\log R$ on $\log t$. For the first time, we propose that the melting point of polymer crystals is related to the lamellar lateral diameter R, instead of the lamellar thickness L. So the famous GT plot based on T_m and L should be replaced by T_m and R. Because both the HW and GT plot are questioned, the famous concept of the equilibrium melting temperature of an infinite large crystal, T_m^0, is also questioned (The extrapolation of T_m^0 in experiments is inaccurate and unreliable too). So choosing T_m^0 as the reference temperature for the degree of supercooling $\Delta T = T_m^0 - T$ may not be a good idea. Instead, in line with the early experiments, we propose that a better reference temperature should be determined

by the slow heating technique. This true equilibrium temperature is independent of many factors and history-free. A broad melting transition for polymer crystals is attributed to the 2D geometry confinement, rather than broad distributions of lamellar thickness. Shish-kebab studies add further support to the prefolding concept. The time dependence of spacings and lognormal distributions are both consistent with experiments. A new relation of $\log G_S \sim 1/T$ is proposed to replace the previous two models based on the LH theory, where $G_S = \frac{S - S_0}{time}$ is the spacing growth rate and S_0 is the initial spacing. Another new relation $G_S \sim 1/C$ is predicted and to be tested against experiments. It is further suggested that Ostwald ripening is the dominating mechanism responsible for polymer crystallization.

All in all, the concepts of prefolding and predetermined thickness, dependence of T_m on R instead of L, and mechanisms of 2D nucleation and Ostwald ripening are key new concepts here. The present study puts polymer crystallization from dilute solutions back into the same general framework of classical crystallization of small molecules (In contrast, traditional theories of polymer crystallization put too much emphasis on the chain folding process and ignored the connection with small molecule crystallization). The only distinction between crystallization of polymers and small molecules is the anisotropic interactions introduced here, which confines polymers crystallizing into a 2D lamella and slows down both crystallization and melting rates.

7.1.2 Future Work

Although the prefolding framework has been roughly established, there are still many aspects to be improved. Large-scale Langevin Dynamics simulations are desired, where much more chains are put into the simulation box and hopefully the Ostwald ripening process can be observed (A similar Ostwald ripening process for the polymer melt has been simulated over 10^6 CPU hours.[161]). Once a big lamella is formed, how it is melted is another interesting question. If we can observe layer-by-layer chain desorptions upon heating in the Langevin Dynamics simulations, it will be further support to our Monte Carlo simulation results as regards crystal melting. The equilibrium lamellar thickness can be calculated more accurately for such a many-chain system too. On the other hand, more Monte Carlo simulations are also desired. Although we have used shish-kebab crystals as a model system for multiple crystals, it is desired to redo the simulations with a real multi-crystal system. The dependences of melting points on many factors should be the same. Temperature dependence of the growth rate for the multi-crystal system should exhibit a bell shape like what we observed for amyloid multiple fibrils (data not shown). In addition, we can extend our Monte Carlo model to study other peculiar systems, such as molecular-weight (MW) segregation phenomenon[162-164] (crystallization of mixtures of low- and high-MW chains results in crystals of high-MW chains surrounded by low-MW free chains at higher temperatures) and effects of confine geometry[165,166] (how the growth rate of polymer crystals varies with the film thickness).

7.2 Amyloid Fibrillization

7.2.1 Conclusions

A generic model which neglects molecular details inside the aggregation unit has been proposed and successfully applied to amyloid fibril formation. Because of the puzzle of "1D nucleation", in the amyloid community, the nature of the nucleus is often confused with the smallest dynamic unit. The nucleus was thought as one turn of helix, a folded monomer, or a micelle. Namely, once the nucleus is formed, linear aggregation of these nuclei will be spontaneous and not hindered by nucleation barrier any more. However, our simulation results present an entirely different view. The 1D nucleation is indeed nonexistent, because our pure 1D simulations reveal no sigmoidal shapes or finite lag time. The amyloid fibril is found to be a semi-2D object. The nucleation barrier arises from the size-dependent desorption rate. The role and importance of the second layer is stressed. The nucleus, i.e. critical nucleus size, can be a two-layer structure composed of multiple dynamic units. Namely, the nucleus is not one aggregation unit in the traditional view but a collection of aggregation units. The nucleus does not correspond to a constant number of units either. The critical nucleus size varies with temperature, concentration, and even time. Another important concept we introduced is the Ostwald ripening growth mechanism which remains unnoticed in the research field of amyloid. Ostwald ripening reconciles the debate about the role of protofibrils (serving as both a monomer reservoir and precursors depending on its relative size).

The above new concepts are supported by our simulations which have reproduced numerous experimental results, including the "seeding" phenomenon, time evolution of fibril size distributions, temperature and concentration dependences of elongation rates, and disassembly upon dilution.

7.2.2 Future Work

Although we have gained a deeper understanding of the mechanisms of nucleation and growth for amyloid fibrils, our ultimate goal is to find out how to reverse or inhibit the amyloid fibril growth, thus controlling the related Alzheimer's and Huntington's diseases. The promise of interdisciplinary research lies in its power to generate new ideas. For example, the well known "molecular weight segregation" phenomenon[162-164] in the polymer crystallization field might suggest an inhibitor for the amyloid disease. By adding low-MW chains into the solution of high-MW chains, crystallization of the high-MW chains are impeded, and the morphology thus formed can be altered by the amount of low-MW components. Similarly, if we add shorter peptides (e.g. benign $A\beta_{1\text{-}30}$) into the longer peptides (e.g. toxic $A\beta_{1\text{-}40}$) solutions, the shorter one might impede the fibrillization of longer ones, or alter the fibril morphology to reduce its toxicity. In this aspect, Monte Carlo simulations of two species with different magnitudes of interaction energies are desired to study systematically how the concentration of short peptides alters the growth rate and morphology of amyloid fibrils formed from longer toxic peptides.

Table 7.1: Comparisons between the two existing models and our prefolding model

	LH theory	SG model	Our prefolding model
Smallest dynamic unit	Stem (80 $-CH_2-$)	Segment (6 $-CH_2-$)	Prefolded Chain (1000 $-CH_2-$) (supported by nodular structures seen in experiments)
Barrier	1D intra-chain stem nucleation barrier (simulations show no barrier)	Pinning entropic barrier (AFM shows no tapered edge)	2D multi-chain nucleation barrier (our simulations confirm prefolding and aggregation)
Habit – T	Only low-T roughening	Only high-T roughening	Both low-T and high-T roughenings
G – T	Exponential (3 regimes) (regime transitions not concomitant with morphology transitions)	Exponential	Exponential (no regimes)
L – T	δL catastrophe	No δL catastrophe	No δL catastrophe Predetermined equilibrium thickness (supported by isochronous decoration experiments)
$G \sim C^{\alpha}$	Cilia nucleation		α increases with increasing T or decreasing C, α is not constant
τ	τ – T		τ – R_0, T, C Phase diagram of critical nucleus sizes
T_m	HW plot ($T_m - T_c$) $T_m \sim \log t_c$ GT plot (T_m – 1/L)		$T_m \sim \beta^{0.5}$ (Converge at slowest β) T_m increases exponentially with T_c (HW plot invalid) Sigmoidal $T_m - \log t_c$ $T_m \sim \log R$, irrelevant with L
Shish-kebab	$\ln S \sim 1/T\Delta T$ $\ln S \sim 1/T\Delta T^2$		Lognormal distribution S ~ time $\ln G_S \sim 1/T$ $G_S \sim 1/C$ Ostwald ripening $R \sim t^{1/3}$

BIBLIOGRAPHY

[1] J. I. Lauritzen and J. D. Hoffman, J. Res. Natl. Bur. Stand. Sec. A **64** (1), 73 (1960).

[2] J. D. Hoffman and J. I. Lauritzen, J. Res. Natl. Bur. Stand. Sec. A **65** (4), 297 (1961).

[3] D. M. Sadler, Polymer **24** (11), 1401 (1983).

[4] D. M. Sadler, Polymer **28** (9), 1440 (1987).

[5] D. M. Sadler and G. H. Gilmer, Polymer **25** (10), 1446 (1984).

[6] D. M. Sadler and G. H. Gilmer, Phys. Rev. Lett. **56** (25), 2708 (1986).

[7] D. M. Sadler and G. H. Gilmer, Phys. Rev. B **38** (8), 5684 (1988).

[8] J. T. Jarrett and P. T. Lansbury, Cell **73** (6), 1055 (1993).

[9] J. D. Harper and P. T. Lansbury, Annu. Rev. Biochem. **66**, 385 (1997).

[10] J. U. Sommer and G. Reiter, J. Chem. Phys. **112** (9), 4384 (2000).

[11] J. P. K. Doye and D. Frenkel, J. Chem. Phys. **110** (5), 2692 (1999).

[12] C. Liu and M. Muthukumar, J. Chem. Phys. **109** (6), 2536 (1998).

[13] P. Welch and M. Muthukumar, Phys. Rev. Lett. **87** (21), 218302 (2001).

[14] S. Fujiwara and T. Sato, J. Chem. Phys. **107** (2), 613 (1997).

[15] T. A. Kavassalis and P. R. Sundararajan, Macromolecules **26** (16), 4144 (1993).

[16] M. Muthukumar and P. Welch, Polymer **41** (25), 8833 (2000).

[17] M. Muthukumar, Adv. Polym. Sci. **191**, 241 (2005).

[18] J. Loos, P. C. Thune, J. W. Niemantsverdriet, and P. J. Lemstra, Macromolecules **32** (26), 8910 (1999).

[19] S. Magonov and Y. Godovsky, American Laboratory **31** (8), 52 (1999).

[20] D. H. Jones, A. J. Latham, A. Keller, and M. Girolamo, J. Polym. Sci., Part B: Polym. Phys. **11** (9), 1759 (1973).

[21] L. Larini and D. Leporini, J. Chem. Phys. **123** (14), 144907 (2005).

[22] J. J. Point, M. C. Colet, and M. Dosiere, J. Polym. Sci., Part B: Polym. Phys. **24** (2), 357 (1986).

[23] M. W. Tian, M. Dosiere, S. Hocquet, P. J. Lemstra, and J. Loos, Macromolecules **37** (4), 1333 (2004).

[24] W. Paul, D. Y. Yoon, and G. D. Smith, J. Chem. Phys. **103** (4), 1702 (1995).

[25] N. Waheed, M. S. Lavine, and G. C. Rutledge, J. Chem. Phys. **116** (5), 2301 (2002).

[26] M. P. Allen and D. J. Tildesley, *Computer Simulation of Liquids*. (Clarendon Press, Oxford, 1987).

[27] P. Juhasz, J. Varga, K. Belina, and H. Marand, Journal of Thermal Analysis and Calorimetry **69** (2), 561 (2002).

[28] P. Supaphol, J. E. Spruiell, and J. S. Lin, Polymer International **49** (11), 1473 (2000).

[29] M. Cooper and R. S. J. Manley, Macromolecules **8** (2), 219 (1975).

[30] J. D. Hoffman, L. J. Frolen, G. S. Ross, and J. I. Lauritzen, J. Res. Natl. Bur. Stand. Sec. A **79** (6), 671 (1975).

[31] J. D. Hoffman, Polymer **24** (1), 3 (1983).

[32] J. D. Hoffman and R. L. Miller, Polymer **38** (13), 3151 (1997).

[33] J. M. Schultz, *Polymer Crystallization: The Development of Crystalline Order in Thermoplastic Polymers*. (Oxford University Press, 2001).

[34] S. Z. D. Cheng, J. J. Janimak, A. Zhang, and H. N. Cheng, Macromolecules **23** (1), 298 (1990).

[35] J. P. Armistead and J. D. Hoffman, Macromolecules **35** (10), 3895 (2002).

[36] S. Z. D. Cheng, J. H. Chen, and J. J. Janimak, Polymer **31** (6), 1018 (1990).

[37] P. J. Phillips and N. Vatansever, Macromolecules **20** (9), 2138 (1987).

[38] J. J. Point and J. J. Janimak, J. Cryst. Growth **131** (3-4), 501 (1993).

[39] S. J. Organ and A. Keller, J. Polym. Sci., Part B: Polym. Phys. **24** (10), 2319 (1986).

[40] S. J. Organ and A. Keller, J. Mater. Sci. **20** (5), 1571 (1985).

[41] S. Hocquet, M. Dosiere, A. Thierry, B. Lotz, M. H. J. Koch, N. Dubreuil, and D. A. Ivanov, Macromolecules **36** (22), 8376 (2003).

[42] M. W. Tian and J. Loos, J. Polym. Sci., Part B: Polym. Phys. **39** (7), 763 (2001).

[43] V. Tikare and J. D. Cawley, Acta Materialia **46** (4), 1333 (1998).

[44] V. Tikare and J. D. Cawley, Acta. Mater. **46** (4), 1343 (1998).

[45] V. Tikare and J. D. Cawley, J. Am. Ceram. Soc. **81** (3), 485 (1998).

[46] H. M. Zeng, K. I. Jacob, and V. Tikare, J. Cryst. Growth **262** (1-4), 602 (2004).

[47] N. Metropolis, A. W. Rosenbluth, M. N. Rosenbluth, A. H. Teller, and E. Teller, J. Chem. Phys. **21** (6), 1087 (1953).

[48] B. Wunderlich, T. W. Shu, and E. A. James, J. Polym. Sci., Part A **2** (6), 2759 (1964).

[49] B. Wunderlich and P. Sullivan, J. Polym. Sci. **61** (171), 195 (1962).

[50] V. F. Holland and P. H. Lindenmeyer, J. Polym. Sci. **57** (165), 589 (1962).

[51] F. Kloos, Mandelke.L, and S. Go, J. Polym. Sci., Part B: Polym. Phys. **12** (6), 1145 (1974).

[52] A. Toda and H. Kiho, J. Polym. Sci., Part B: Polym. Phys. **27** (1), 53 (1989).

[53] Y. Tanzawa, Polymer **33** (13), 2659 (1992).

[54] M. Yamashita, H. Miyaji, A. Hoshino, and K. Izumi, Polym. J. **36** (3), 226 (2004).

[55] R. L. Miller and J. D. Hoffman, Polymer **32** (6), 963 (1991).

[56] A. Toda, J. Phys. Soc. Jpn. **55** (10), 3419 (1986).

[57] A. Toda, Polymer **32** (5), 771 (1991).

[58] K. Armistead, G. Goldbeckwood, and A. Keller, Adv. Polym. Sci. **100**, 221 (1992).

[59] D. J. Blundell and A. Keller, J. Polym. Sci., Part B: Polym. Lett. **6** (6), 433 (1968).

[60] H. Wang, J. Polym. Sci., Part B: Polym. Phys. **42** (17), 3133 (2004).

[61] L. Mandelkern, J. Appl. Phys. **26** (4), 443 (1955).

[62] A. Keller and Pedemont.E, J. Cryst. Growth **18** (2), 111 (1973).

[63] A. Toda, H. Miyaji, and H. Kiho, Polymer **27** (10), 1505 (1986).

[64] I. C. Sanchez and E. A. Dimarzio, Macromolecules **4** (6), 677 (1971).

[65] I. C. Sanchez and E. A. Dimarzio, J. Chem. Phys. **55** (2), 893 (1971).

[66] A. Toda, H. Kiho, H. Miyaji, and K. Asai, J. Phys. Soc. Jpn. **54** (4), 1411 (1985).

[67] N. Ding and E. J. Amis, Macromolecules **24** (13), 3906 (1991).

[68] A. J. Pennings, R. Lageveen, and R. S. Devries, Colloid Polym. Sci. **255** (6), 532 (1977).

[69] A. J. Pennings, J. M. A. A. van der Mark, and A. M. Kiel, Kolloid Z. Z. Polym. **237** (2), 336 (1970).

[70] M. J. Hill, P. J. Barham, and A. Keller, Colloid Polym. Sci. **258** (9), 1023 (1980).

[71] M. J. Hill, P. J. Barham, and A. Keller, Colloid Polym. Sci. **261** (9), 721 (1983).

[72] A. Keller, Journal of Polymer Science **21** (99), 363 (1956).

[73] M. J. Hill and A. Keller, Colloid Polym. Sci. **259** (3), 335 (1981).

[74] J. Petermann and H. Gleiter, Journal of Polymer Science Part C-Polymer Letters **15** (11), 649 (1977).

[75] R. H. Somani, L. Yang, B. S. Hsiao, P. K. Agarwal, H. A. Fruitwala, and A. H. Tsou, Macromolecules **35** (24), 9096 (2002).

[76] R. H. Somani, B. S. Hsiao, A. Nogales, S. Srinivas, A. H. Tsou, I. Sics, F. J. Balta-Calleja, and T. A. Ezquerra, Macromolecules **33** (25), 9385 (2000).

[77] I. Dukovski and M. Muthukumar, J. Chem. Phys. **118** (14), 6648 (2003).

[78] W. B. Hu, D. Frenkel, and V. B. F. Mathot, Macromolecules **35** (19), 7172 (2002).

[79] P. J. Barham and A. Keller, J. Mater. Sci. **20** (7), 2281 (1985).

[80] T. X. Liu, W. C. Tjiu, and J. Petermann, J. Cryst. Growth **243** (1), 218 (2002).

[81] T. X. Liu, I. Lieberwirth, and J. Petermann, Macromolecular Chemistry and Physics **202** (14), 2921 (2001).

[82] T. Nagasawa and Y. Shimomura, Journal of Polymer Science Part B-Polymer Physics **12** (11), 2291 (1974).

[83] J. Rau, R. M. Gohil, J. Petermann, and J. M. Schultz, Colloid Polym. Sci. **259** (2), 241 (1981).

[84] J. Petermann, R. M. Gohil, J. M. Schultz, R. W. Hendricks, and J. S. Lin, Journal of Polymer Science Part B-Polymer Physics **20** (3), 523 (1982).

[85] P. H. Geil, Journal of Macromolecular Science-Physics **B 12** (2), 173 (1976).

[86] G. S. Y. Yeh and P. H. Geil, J. Macromol. Sci., Phys. **1** (2), 251 (1967).

[87] J. K. Hobbs, A. D. L. Humphris, and M. J. Miles, Macromolecules **34** (16), 5508 (2001).

[88] J. K. Hobbs and M. J. Miles, Macromolecules **34** (3), 353 (2001).

[89] G. H. Michler, I. Naumann, F. J. B. Calleja, and F. Ania, Acta Polym. **48** (1-2), 36 (1997).

[90] B. Wunderlich, *Macromolecular physics*. (Vol. 3, Academic Press, New York, 1980).

[91] J. D. Hoffman and J. J. Weeks, J. Res. Natl. Bur. Stand. Sec. A **66** (1), 13 (1962).

[92] J. D. Hoffman and J. J. Weeks, Journal of Chemical Physics **42** (12), 4301 (1965).

[93] R. G. Alamo, B. D. Viers, and L. Mandelkern, Macromolecules **28** (9), 3205 (1995).

[94] E. Hellmuth and B. Wunderlich, J. Appl. Phys. **36** (10), 3039 (1965).

[95] A. Toda, M. Hikosaka, and K. Yamada, Polymer **43** (5), 1667 (2002).

[96] J. E. K. Schawe and G. R. Strobl, Polymer **39** (16), 3745 (1998).

[97] S. Sohn, A. Alizadeh, and H. Marand, Polymer **41** (25), 8879 (2000).

[98] R. Endo, S. Amiya, and M. Hikosaka, Journal of Macromolecular Science-Physics **B42** (3-4), 793 (2003).

[99] L. Finelli, N. Lotti, A. Munari, M. Gazzano, and V. Malta, Journal of Polymer Science Part B-Polymer Physics **42** (3), 553 (2004).

[100] D. E. Roberts and L. Mandelkern, J. Am. Chem. Soc. **77** (3), 781 (1955).

[101] J. N. Xu, S. Srinivas, H. Marand, and P. Agarwal, Macromolecules **31** (23), 8230 (1998).

[102] J. J. Weeks, Journal of Research of the National Bureau of Standards Section a-Physics and Chemistry **A 67** (5), 441 (1963).

[103] K. Yamada, M. Hikosaka, A. Toda, S. Yamazaki, and K. Tagashira, Macromolecules **36** (13), 4790 (2003).

[104] P. L. Wu and E. M. Woo, Journal of Polymer Science Part B-Polymer Physics **40** (15), 1571 (2002).

[105] C. Wang, Y. C. Hsu, and C. F. Lo, Polymer **42** (20), 8447 (2001).

[106] H. Marand, J. N. Xu, and S. Srinivas, Macromolecules **31** (23), 8219 (1998).

[107] J. Clements, G. Capaccio, and I. M. Ward, Journal of Polymer Science Part B-Polymer Physics **17** (4), 693 (1979).

[108] H. Marand and Z. Y. Huang, Macromolecules **37** (17), 6492 (2004).

[109] T. Sasaki, H. Sunago, and T. Hoshikawa, Polymer Engineering and Science **43** (3), 629 (2003).

[110] R. G. Alamo, E. K. M. Chan, L. Mandelkern, and I. G. Voigtmartin, Macromolecules **25** (24), 6381 (1992).

[111] R. J. Samuels, Journal of Polymer Science Part B-Polymer Physics **13** (7), 1417 (1975).

[112] Y. Kong and J. N. Hay, Polymer **44** (3), 623 (2003).

[113] G. Guerra, V. Petraccone, P. Corradini, C. Derosa, R. Napolitano, and B. Pirozzi, Journal of Polymer Science Part B-Polymer Physics **22** (6), 1029 (1984).

[114] J. C. Rochet and P. T. Lansbury, Curr. Opin. Struct. Biol. **10** (1), 60 (2000).

[115] J. D. Sipe and A. S. Cohen, J. Struct. Biol. **130** (2-3), 88 (2000).

[116] M. P. Lambert, A. K. Barlow, B. A. Chromy, C. Edwards, R. Freed, M. Liosatos, T. E. Morgan, I. Rozovsky, B. Trommer, K. L. Viola, P. Wals, C. Zhang, C. E. Finch, G. A. Krafft, and W. L. Klein, Proc. Natl. Acad. Sci. U. S. A. **95** (11), 6448 (1998).

[117] M. Bucciantini, E. Giannoni, F. Chiti, F. Baroni, L. Formigli, J. S. Zurdo, N. Taddei, G. Ramponi, C. M. Dobson, and M. Stefani, Nature **416** (6880), 507 (2002).

[118] R. Tycko, Curr. Opin. Struct. Biol. **14** (1), 96 (2004).

[119] L. C. Serpell, Biochim. Biophys. Acta **1502** (1), 16 (2000).

[120] M. F. Perutz, T. Johnson, M. Suzuki, and J. T. Finch, Proc. Natl. Acad. Sci. U. S. A. **91** (12), 5355 (1994).

[121] P. Sikorski and E. Atkins, Biomacromolecules **6** (1), 425 (2005).

[122] R. Nelson, M. R. Sawaya, M. Balbirnie, A. O. Madsen, C. Riekel, R. Grothe, and D. Eisenberg, Nature **435** (7043), 773 (2005).

[123] A. T. Petkova, Y. Ishii, J. J. Balbach, O. N. Antzutkin, R. D. Leapman, F. Delaglio, and R. Tycko, Proc. Natl. Acad. Sci. U. S. A. **99** (26), 16742 (2002).

[124] M. F. Perutz, J. T. Finch, J. Berriman, and A. Lesk, Proc. Natl. Acad. Sci. U. S. A. **99** (8), 5591 (2002).

[125] J. L. Jimenez, J. L. Guijarro, E. Orlova, J. Zurdo, C. M. Dobson, M. Sunde, and H. R. Saibil, EMBO J. **18** (4), 815 (1999).

[126] M. Sunde, L. C. Serpell, M. Bartlam, P. E. Fraser, M. B. Pepys, and C. C. F. Blake, J. Mol. Biol. **273** (3), 729 (1997).

[127] O. S. Makin, E. Atkins, P. Sikorski, J. Johansson, and L. C. Serpell, Proc. Natl. Acad. Sci. U. S. A. **102** (2), 315 (2005).

[128] J. T. Jarrett, E. P. Berger, and P. T. Lansbury, Biochemistry **32** (18), 4693 (1993).

[129] H. Y. Han, P. H. Weinreb, and P. T. Lansbury, Chem. Biol. **2** (3), 163 (1995).

[130] S. M. Chen, V. Berthelier, J. B. Hamilton, B. O'Nuallain, and R. Wetzel, Biochemistry **41** (23), 7391 (2002).

[131] J. Hofrichter, P. D. Ross, and W. A. Eaton, Proc. Natl. Acad. Sci. U. S. A. **71** (12), 4864 (1974).

[132] T. Arvinte, A. Cudd, and A. F. Drake, J. Biol. Chem. **268** (9), 6415 (1993).

[133] E. Scherzinger, A. Sittler, K. Schweiger, V. Heiser, R. Lurz, R. Hasenbank, G. P. Bates, H. Lehrach, and E. E. Wanker, Proc. Natl. Acad. Sci. U. S. A. **96** (8), 4604 (1999).

[134] L. Nielsen, R. Khurana, A. Coats, S. Frokjaer, J. Brange, S. Vyas, V. N. Uversky, and A. L. Fink, Biochemistry **40** (20), 6036 (2001).

[135] N. Ferguson, J. Berriman, M. Petrovich, T. D. Sharpe, J. T. Finch, and A. R. Fersht, Proc. Natl. Acad. Sci. U. S. A. **100** (17), 9814 (2003).

[136] L. Zhu, X. J. Zhang, L. Y. Wang, J. M. Zhou, and S. Perrett, J. Mol. Biol. **328** (1), 235 (2003).

[137] P. Hortschansky, V. Schroeckh, T. Christopeit, G. Zandomeneghi, and M. Fandrich, Protein Sci. **14** (7), 1753 (2005).

[138] A. Lomakin, D. S. Chung, G. B. Benedek, D. A. Kirschner, and D. B. Teplow, Proc. Natl. Acad. Sci. U. S. A. **93** (3), 1125 (1996).

[139] S. H. Xu, B. Bevis, and M. F. Arnsdorf, Biophys. J. **81** (1), 446 (2001).

[140] S. M. Chen, F. A. Ferrone, and R. Wetzel, Proc. Natl. Acad. Sci. U. S. A. **99** (18), 11884 (2002).

[141] J. D. Harper, S. S. Wong, C. M. Lieber, and P. T. Lansbury, Chem. Biol. **4** (2), 119 (1997).

[142] D. M. Walsh, A. Lomakin, G. B. Benedek, M. M. Condron, and D. B. Teplow, J. Biol. Chem. **272** (35), 22364 (1997).

[143] J. D. Harper, S. S. Wong, C. M. Lieber, and P. T. Lansbury, Biochemistry **38** (28), 8972 (1999).

[144] H. K. L. Blackley, G. H. W. Sanders, M. C. Davies, C. J. Roberts, S. J. B. Tendler, and M. J. Wilkinson, J. Mol. Biol. **298** (5), 833 (2000).

[145] C. Goldsbury, P. Frey, V. Olivieri, U. Aebi, and S. A. Muller, J. Mol. Biol. **352** (2), 282 (2005).

[146] J. N. Zhang and M. Muthukumar, J. Chem. Phys. **126** (23), 234904 (2007).

[147] L. C. Serpell and J. M. Smith, J. Mol. Biol. **299** (1), 225 (2000).

[148] M. S. Lamm, K. Rajagopal, J. P. Schneider, and D. J. Pochan, J. Am. Chem. Soc. **127** (47), 16692 (2005).

[149] H. A. Lashuel, S. R. LaBrenz, L. Woo, L. C. Serpell, and J. W. Kelly, J. Am. Chem. Soc. **122** (22), 5262 (2000).

[150] C. S. Goldsbury, S. Wirtz, S. A. Muller, S. Sunderji, P. Wicki, U. Aebi, and P. Frey, J. Struct. Biol. **130** (2-3), 217 (2000).

[151] H. H. Bauer, U. Aebi, M. Haner, R. Hermann, M. Muller, T. Arvinte, and H. P. Merkle, J. Struct. Biol. **115** (1), 1 (1995).

[152] J. L. Jimenez, E. J. Nettleton, M. Bouchard, C. V. Robinson, C. M. Dobson, and H. R. Saibil, Proc. Natl. Acad. Sci. U. S. A. **99** (14), 9196 (2002).

[153] J. D. Harper, C. M. Lieber, and P. T. Lansbury, Chem. Biol. **4** (12), 951 (1997).

[154] A. Lomakin, D. B. Teplow, D. A. Kirschner, and G. B. Benedek, Proc. Natl. Acad. Sci. U. S. A. **94** (15), 7942 (1997).

[155] A. J. Modler, K. Gast, G. Lutsch, and G. Damaschun, J. Mol. Biol. **325** (1), 135 (2003).

[156] C. K. Haas and J. M. Torkelson, Physical Review E **55** (3), 3191 (1997).

[157] T. Ban, D. Hamada, K. Hasegawa, H. Naiki, and Y. Goto, J. Biol. Chem. **278** (19), 16462 (2003).

[158] M. R. H. Krebs, L. A. Morozova-Roche, K. Daniel, C. V. Robinson, and C. M. Dobson, Protein Sci. **13** (7), 1933 (2004).

[159] S. J. Wood, J. Wypych, S. Steavenson, J. C. Louis, M. Citron, and A. L. Biere, J. Biol. Chem. **274** (28), 19509 (1999).

[160] G. H. Gilmer, Science **208** (4442), 355 (1980).

[161] R. H. Gee, N. Lacevic, and L. E. Fried, Nature Materials **5** (1), 39 (2006).

[162] H. D. Keith and F. J. Padden, J. Appl. Phys. **35** (4), 1286 (1964).

[163] H. D. Keith and F. J. Padden, J. Appl. Phys. **35** (4), 1270 (1964).

[164] W. B. Hu, Macromolecules **38** (21), 8712 (2005).

[165] K. Taguchi, H. Miyaji, K. Izumi, A. Hoshino, Y. Miyamoto, and R. Kokawa, Polymer **42** (17), 7443 (2001).

[166] S. Ok and A. L. Demirel, J. Macromol. Sci., Phys. **B42** (3-4), 611 (2003).